

Universität
Rostock



Traditio et Innovatio

DOCTORAL DISSERTATION

Pseudo piezoelectricity in calcium
titanate and structural changes
under electric field

Abdullah Riaz

Born on 22.09.1989 in Kuwait from Pakistan

University of Rostock

*Faculty of Mathematics and Natural Sciences
Institute of Physics - Physics of New Materials*

Rostock, 2019

Reviewer:

Professor Dr. Eberhard Burkel, University of Rostock, Faculty of Mathematics and Natural Sciences, Institute of Physics - Physics of New Materials

Professor Dr. -Ing. Hermann Seitz, University of Rostock, Chair of Fluid Technology and Microfluidics

Year of submission: 2019

Year of defense: 2019

Abstract

Perovskite polycrystalline calcium titanate has orthorhombic crystal structure at room temperature and belongs to the centro-symmetric point group. This implies that calcium titanate does not exhibit piezoelectric behaviour. However, in the present study such behaviour is observed in calcium titanate prepared by sol-gel synthesis and densified by field assisted sintering technique. Presumably, the instability of regular TiO_6 octahedra results in the off-centering of titanium positions in nanostructured bulk calcium titanate. This phenomenon leads to the breaking of crystal symmetry causing the generation of electric dipoles. These electric dipoles are created due to the lattice distortions produced by the formation of highly localized defects, i.e. oxygen vacancies, during densification by field assisted sintering. As a consequence, piezoelectric behaviour is observed in calcium titanate which is referred to “pseudo piezoelectricity”. Additionally, in-situ high energy X-ray diffraction study revealed domains switching under external electric field. The contribution of non-180° domains reorientation has also been observed. These structural responses testify the observed pseudo piezoelectric behaviour in calcium titanate. The produced charge (Q) and the average piezoelectric constant (d_{33}) values of field assisted sintered calcium titanate have been determined to be $Q = (2.7 \pm 0.5)$ pC and $d_{33} \sim 0.595$ pm/V, respectively. The mentioned average piezoelectric constant d_{33} value is comparable with the piezoelectric constant d_{ij} values of natural bone. This particular response of calcium titanate is of great interest in biomedicine because it can improve osseointegration of implant materials.

Zusammenfassung

Polykristallines Calciumtitanat hat bei Raumtemperatur eine orthorhombische Kristallstruktur (Perovskitstruktur). Aufgrund seiner zentrosymmetrischen Elementarzelle zeigt Calciumtitanat kein piezoelektrisches Verhalten. Die vorliegende Arbeit weist jedoch piezoelektrisches Verhalten von Calciumtitanat nach, das mittels Sol-Gel Synthese hergestellt und mittels Feld-Aktiviertem Sintern (FAST) verdichtet wurde. Vermutlich verursacht die Instabilität regulärer TiO_6 Oktaeder eine Verschiebung der Positionen von Titanatomen in Festkörpern aus nanostrukturiertem Calciumtitanat. Dieses Phänomen verursacht die Verletzung der Kristallsymmetrie und erzeugt elektrische Dipole. Die Dipole entstehen aufgrund von Gitterverzerrungen, die durch stark lokalisierte Defekte - Sauerstoff-Leerstellen - während des Feld-Aktivierten Sinterns auftreten. Daher kann piezoelektrisches Verhalten, genannt "Pseudopiezoelektrizität", in Calciumtitanat beobachtet werden. Außerdem konnte in in-situ Hochenergie-öntgendiffraktionsmessungen das Umklappen von Domänen unter Einfluss eines externen elektrischen Feldes beobachtet werden. Auch der Beitrag von Umklappen um von 180° verschiedene Winkel wurde nachgewiesen. Diese strukturelle Antwort auf das externe elektrische Feld bestätigt das beobachtete piezoelektrische Verhalten von Calciumtitanat. Erzeugte Ladung (Q) und piezoelektrische Konstante (d_{33}) wurden zu $Q = (2.7 \pm 0.5) \text{ pC}$ und $d_{33} \sim 0.595 \text{ pm/V}$ bestimmt. Der Durchschnittswert für die piezoelektrische Konstante d_{33} ist vergleichbar mit den Werten für d_{ij} in natürlichem Knochen. Dieses Ergebnis ist von großem Interesse für biomedizinische Anwendungen zur Verbesserung der Osseointegration von Implantatmaterialien.

Dedication

To my parents, beautiful wife, children and sisters.

Contents

1	Motivation	1
2	Theory	5
2.1	<i>CaTiO</i> ₃ crystal structure	5
2.1.1	Phases	6
2.2	Defect physics	7
2.2.1	Point defects	7
2.2.2	Trapping of charge defects	9
2.3	Piezoelectric effect	10
2.3.1	Symmetries of crystals	10
2.3.2	Piezoelectric ceramics	11
2.3.3	Electromechanical equations	13
2.3.4	Domain walls and their contribution	15
2.3.5	Piezoelectricity in <i>CaTiO</i> ₃	15
3	Synthesis techniques and sample preparation	17
3.1	Sol-gel synthesis	17
3.2	Spray drying	18
3.3	Field assisted sintering technique	18
3.4	Conventional sintering	19
3.5	Preparation of <i>CaTiO</i> ₃	19
3.5.1	Sol-gel synthesis	19
3.5.2	Field assisted sintering	21
3.5.3	Conventional sintering	22
3.5.4	Polishing	23
3.5.5	Sputter coating	23
4	Experimental methods and set-ups	25
4.1	Differential scanning calorimetry	25
4.2	Scanning electron microscope	26
4.3	Energy dispersive X-ray spectroscopy	27
4.4	X-ray photoelectron spectroscopy	27
4.5	Piezoelectric measurements	28
4.6	High energy X-ray diffraction	30
4.6.1	Synchrotron radiation	30
4.6.2	Debye-Sherrer geometry	31
4.6.3	Rietveld refinement	31
4.7	Indentation test	33

4.8	Characterization of $CaTiO_3$	34
4.8.1	Differential scanning calorimetry	34
4.8.2	Scanning electron microscopy and energy dispersive X-ray spectroscopy	34
4.8.3	X-ray photoelectron spectroscopy	35
4.8.4	Piezoelectric measurement	36
4.8.5	High energy X-ray diffraction	37
4.8.6	Nanoindentation test	41
5	Results	43
5.1	Phase analysis - DSC	43
5.2	Structure analysis - HEXRD	44
5.3	Surface morphology - SEM	45
5.4	Chemical composition - EDX	47
5.5	XPS spectra	48
5.5.1	Chemical composition	48
5.5.2	Defect analysis	50
5.6	Piezoelectric response	52
5.7	Structure evolution - HEXRD	54
5.7.1	Lattice parameters	54
5.7.2	Lattice distortion	55
5.7.3	Lattice distortion under external electric field	58
5.7.4	Resistivity	59
5.8	Mechanical effect - Nanoindentation	60
6	Discussion	63
6.1	Pseudo piezoelectricity in field assisted sintered $CaTiO_3$	63
6.2	Piezoelectric matrix and constant	66
6.3	Non-180° domain wall motion	67
6.4	Lattice strain and lattice vibration under external electric field	69
6.5	Evolution of lattice parameters with azimuthal sectors	71
6.6	Structure defects	74
6.7	Texture evolution	79
6.8	Poling treatment	81
7	Conclusion	83
8	Outlook	87
	Appendices	89
A	Azimuthal sector integration from 2D images and lattice parameters	91
B	SEM, XPS and EDX spectroscopy	93
C	In-situ HEXRD	99
D	Nanoindentation	109

Chapter 1

Motivation

During the past years, research and development of orthopaedic implant materials were focused on titanium and its alloys because of their low elastic modulus, corrosion resistance, good biocompatibility and low density [1], [2]. Nowadays, the primary challenge in orthopaedic implant material development is the improvement of osseointegration. Hence, there is a necessity of the improvement of bone implant material in terms of osseointegration. In order to understand the way in which a host bone responds to implant materials, it is important to know its structure and composition, principal cell types present in bone and the way in which bone remodels and repairs itself.

A bone skeletal system is presented in Figure 1.1. It mainly consists of inorganic mineral component which is hydroxylapatite (HA) and an organic matrix of collagen. In other words, the hard substances of bone consist of calcium phosphate crystals as HA which disperse between collagen fibers. HA is shown in cubic shape with green color and collagen fibers in brown tube like shape [3]. The inorganic state can be poorly crystallized, non-stoichiometric or highly defective due to carrying small amount of cations or anions, e.g. CO_3^{2-} , Ca^{2+} , PO_4^{3-} , Mg^{2+} , Fe^{2+} , Na^+ , F^- , Cl^- , and K^+ [4].

In 1957, Fukada and Yasuda discovered a directional piezoelectric effect in bone [5]. This response of bone indicated that bone skeleton has some form of asymmetry in its structure leading to the generation of electric dipoles. It is suggested that these electric dipoles are created by asymmetric collagen molecules. These collagen fibres are oriented parallel to the long axis of the bone which form helices within the lamellae oriented at various angles. To summarize, the overall orientation of collagen is therefore in the direction of bone axis and results in piezoelectric properties [6]. The magnitude of piezoelectric response is mainly controlled by so-called streaming potential as a driving force which also controls the bone structure [7]. It can be demonstrated that osteoblasts and osteoclasts can be controlled by means of electric fields [8]. It is therefore a necessity of the current research to develop implants from electrically activate materials for the bone replacement. This type of materials can support the natural bone structure and improve osseointegration by having comparable piezoelectric property which can mimic natural bone and help in the healing process [5], [9], [10].

In general, bone implant materials can be divided into three groups: metals, ceramics and polymers. Mostly, metal implant materials are used due to above mentioned properties. However, they have poor tribological properties and lack bioactive functionality [11]. Moreover, they do not initiate a response or interact when introduced to biological tissue. In other words, introducing the material to the body will not cause a reaction

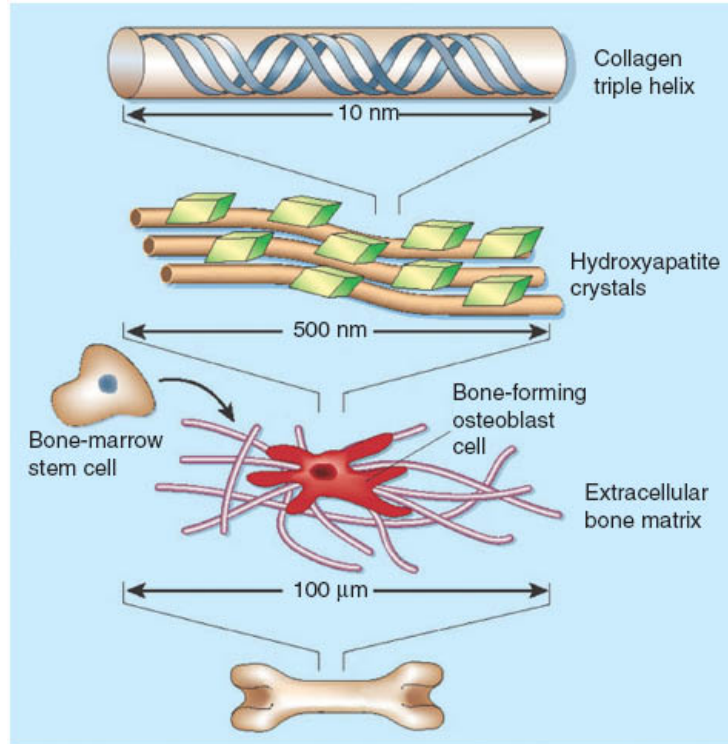


Figure 1.1: Inside view of bone [3]

by the host. Polymeric compounds are also used as surface treatments only because they are capable of being decomposed by bacteria or other living organisms and thereby help in avoiding pollution. Whereas, ceramics can withstand high pressure, show little wear and also exhibit piezoelectric properties. This group also includes calcium titanate ($CaTiO_3$) and HA (40% of the human bone consists of this material). Ceramics can be inert and at the same time promote bone growth by mimicking piezoelectric property of bone [4]. Whereas, most of the investigated ceramics, e.g. $PbTiO_3$ or $BaTiO_3$ or their compounds are toxic [12], [13] and also have much larger piezoelectric constant (d_{ij}) compared to the bone [4], [14]. Previous experiments on surface modifications of titanium surface with perovskite $CaTiO_3$ ceramics revealed that it improves bone binding strength and that it is also a non-toxic substance [15]–[17]. Additionally, $CaTiO_3$ has sufficiently high electrical conductivity and polarizability compared to HA. $CaTiO_3$ also provides positive surface charge which can interact with the negatively charged phosphate ions in the fluid, inducing the formation of a layer of calcium phosphate. Therefore, it has the potential to increase osseointegration probably more than HA [18]. Consequently, a promising candidate for a substitute material is $CaTiO_3$. However, it does not exhibit piezoelectric behaviour [19].

The crystal structure of $CaTiO_3$ consists of corner linked TiO_6 octahedra with calcium atoms allocated between the octahedra. It has an orthorhombic crystal structure at room temperature which belongs to centro-symmetric point group, i.e. mmm , [20] (discussed comprehensively in next Chapter). Ceramics can only show piezoelectric behaviour if they have electric dipoles which are produced due to non-symmetrical charge distribution in the lattice like perovskite titanates such as $SrTiO_3$ or $BaTiO_3$ [14], [21]. However, it is predicted that the instability of regular TiO_6 octahedra will result in off-centering of the titanium positions. The distorted titanium atoms break

the crystal symmetry causing the generation of electric dipoles [22]. This off-centering of titanium atoms was first observed by aberration-corrected TEM imaging in twin boundary of $CaTiO_3$ single crystal grown by the floating zone technique [23]. However, the fundamental challenge is to create instability of regular TiO_6 octahedra in bulk polycrystalline $CaTiO_3$ which can lead to piezoelectric response. One possibility of distortion creation in crystal lattice is the production of lattice oxygen defects [24]. This can be achieved by a thermal treatment in poor oxygen atmosphere at elevated temperature. It is also reported that such defects can strongly influence ferroelectric and piezoelectric properties by the level of their ordering [25]. A promising technique for producing such materials is the field assisted sintering technique (FAST) [26].

FAST is a relatively novel technique used for the densification of powders by applying pulsed directed current and mechanical load simultaneously to assist sintering in a protective gas atmosphere or vacuum. The electric current is essential to achieve high densification at lower temperatures with shorter sintering time [27]–[29]. The advantages of FAST are cleaner grain boundaries in sintered ceramics, higher permittivity in ferroelectrics and improved bonding quality or reduced impurity segregation at grain boundaries [26]. Additionally, the sintering atmosphere also plays an important role in oxidation number, stoichiometry and change in composition or formation of defects [30], [31]. The main advantages of FAST are high heating and cooling rates which enhance densification over grain growth [26], [32]. Accordingly, it is possible to achieve high density of grain boundaries with defective bulk nanostructure which directly influence the physical properties, in particular the electrical properties of the densified material [26]. As a consequence, the application of FAST sintering in vacuum for the production of polycrystalline bulk $CaTiO_3$ can lead to a piezoelectric response of the material [33]. Therefore, $CaTiO_3$ has been investigated. Nanostructured $CaTiO_3$ was synthesized by sol-gel procedure and densified using conventional and FAST sintering. The samples have been examined by differential scanning calorimetry (DSC) to observe the phase transformation temperature, e.g. amorphous to crystal structure. Scanning electron microscopy (SEM), energy dispersive X-ray spectroscopy (EDX) and X-ray photoelectron spectroscopy (XPS) were performed to investigate their microstructure, chemical composition and structural defects, respectively. Furthermore, direct and inverse piezoelectric effects were investigated and the determined piezoelectric constants were compared to the ones of bone. Most importantly, the piezoelectric response of any material originates from its crystal structure. Therefore, in-situ high energy X-ray diffraction (HEXRD) measurement was also performed for the analysis of detailed structural response, i.e. evolution of lattice parameters as well as the structural changes under external electric field (EEF). Additionally, mechanical properties of samples are also studied using nanoindentation test.

Chapter 2

Theory

$CaTiO_3$ is widely used in medical field for the interests in its bioactivity [34]. Bioactivity can be characterized by the structure of a material and its physical properties especially electrical properties or specifically piezoelectric properties [35]. Therefore, crystal structure and phases of $CaTiO_3$, and the influence of point defects as well as their trapping which affect the electrical properties of $CaTiO_3$ is discussed in the following Chapter. Additionally, the basic principles of piezoelectric effect, domain walls and their contribution as well as the possibility of piezoelectricity in $CaTiO_3$ is also discussed.

2.1 $CaTiO_3$ crystal structure

$CaTiO_3$ belongs to the family of perovskite crystal structure. It has a perovskite formula- ABO_3 , where atoms A are located at the corners, B atoms at the body-center and O atoms at the face centers as shown in Figure 2.1 in simplified 2D structure of $CaTiO_3$ [36]. It consists of corner linked TiO_6 octahedra with calcium atoms allocated between the octahedra. The top-to-top-axis of the basis octahedron in unit cell is defined as the O-Ti-O bond with maximum length which is important for the lattice position of possible defects [37].

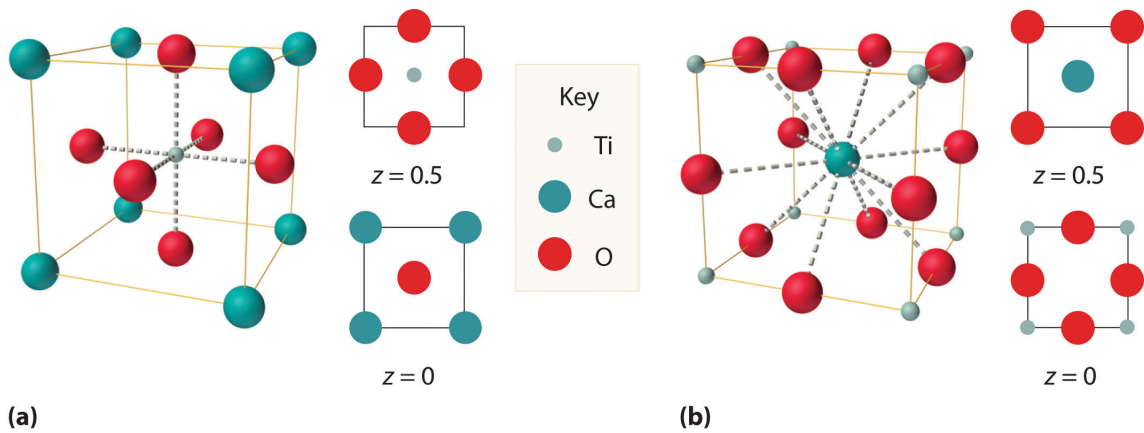


Figure 2.1: Two similar views of 2D perovskite crystal structure of $CaTiO_3$ in simplified form. (a) When Ti atoms are at the center and (b) when Ca atoms are at the center [36].

2.1.1 Phases

$CaTiO_3$ can exist in three phases of crystal structure depending on the temperature range. It has an orthorhombic phase from room temperature to (1498 ± 25) K, tetragonal from (1498 ± 25) K to (1634 ± 13) K and cubic from (1634 ± 13) K to higher temperatures [38]. The lattice parameters and space groups of mentioned phases are presented in Table 2.1.

Crystal structure	Space group	Lattice parameters [\AA]
Orthorhombic	Pbnm	a= 5.380 ± 0.001 b= 5.440 ± 0.001 c= 7.640 ± 0.001
Tetragonal	I4/mcm	a= 5.498 ± 0.003 c= 7.783 ± 0.008
Cubic	Pm3m	a= 3.897 ± 0.001

Table 2.1: Crystal structure, space group, lattice parameters and temperature of particular phases of $CaTiO_3$ [38]–[40].

Among all phases of $CaTiO_3$, orthorhombic is the most stable phase and exists at room temperature. For better understanding of the crystal structure, the 3D visualization of perfect orthorhombic structural model of $CaTiO_3$ crystal unit cell is presented in Figure 2.2. The program VESTA [41] is used for the plotting of this visualization. There are two oxygen sites which are named as O1 and O2. O1 sites are located in top-to-top-axis and O2 sites on plane-axis. All calcium (Ca) and titanium (Ti) atoms connected with O1 and O2 atoms have different bond lengths and bond angles which make the crystal structure more complex.

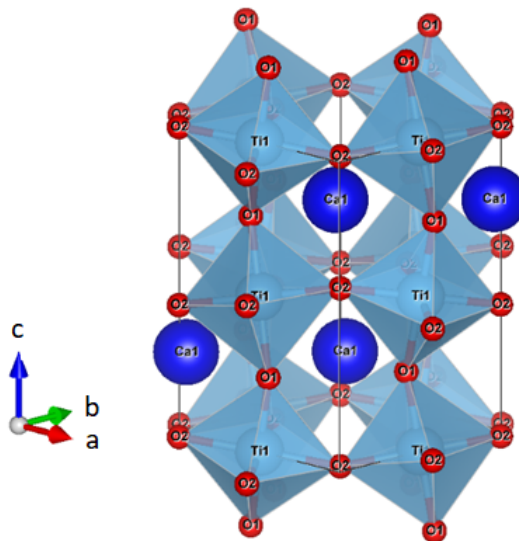


Figure 2.2: 3D visualization of orthorhombic structural model of $CaTiO_3$ crystal unit cell.

2.2 Defect physics

$CaTiO_3$ has high electric permittivity (dielectric) along with other alkaline-earth titanates ($SrTiO_3$ and $BaTiO_3$) and their properties are determined by the defect physics. Additionally, the modification in properties of these materials are possible by producing controlled defects. This can be achieved by doping or by generating oxygen non-stoichiometry [42]. It is also suggested that only crystal structure is not enough for correct illustration of the properties of $CaTiO_3$. Apart from its crystal structure, defect structure should also be considered because defects are electrically charged and therefore affect electrical properties [42]. There is a proposed model of defect physics which is based on the electrical conductivity [43]. This electrical conductivity is determined by the concentration of charge carriers taking part in the conduction. Additionally, their mobility terms are described in following equation [42]:

$$\sigma = e\mu_n n + e\mu_p p + ez_i \mu_i [i] \quad (2.1)$$

where σ is conductivity, e is elementary charge, μ is mobility, n , p and i subscripts are electrons, holes and ions, respectively, as well as n , p and $[i]$ are their respective concentrations and z is charge number of the ions.

The defects generated in any material can be both localized or delocalized defects and mainly depend on how the material is synthesized. These defects also plays an important role in determining material's electrical properties [44]. Therefore, synthesis procedure is very important factor for the modification of electrical properties of material.

2.2.1 Point defects

Crystal structure of $CaTiO_3$ independent of phases, always consists of TiO_6 octahedra as mentioned in last chapter. The crystal structure only differs depending on how these octahedra are connected inside the unit cell. In case of defects, there are two possibilities of creation of oxygen defects which are top-top-top and in-plane. In perfect TiO_6 octahedra, there is no resulting electric dipole in $CaTiO_3$. Therefore, if any resulting electric dipole effect is generated then they are purely produced by doping or in undoped case by defects.

In the case of undoped $CaTiO_3$, oxygen non-stoichiometry can be generated by annealing at elevated temperature or in oxygen partial pressure ($p(O_2)$). The effect of $p(O_2)$ can be considered within the two regimes: extremely reducing and reducing conditions. On one hand, the extremely reducing condition can be described by Kröger-Vink [39] notation through following equilibrium [45]:



where O_o is lattice site oxygen, $V_{\ddot{o}}$ is doubly ionized oxygen vacancy and e is electron. The equilibrium constant K_1 of the Reaction 2.2 is:

$$K_1 = [V_{\ddot{o}}]n^2p(O_2)^{1/2} \quad (2.3)$$

It is assumed that the oxygen vacancies are mainly lattice defects. So, the charge neutrality in lattice needs to be:

$$2[V_{\ddot{o}}] = n \quad (2.4)$$

Therefore,

$$n = (2K_1)^{1/3} p(O_2)^{-1/6} \quad (2.5)$$

On the other hand, reducing conditions in the $p(O_2)$ range cause defects other than ionized oxygen vacancies. They can be singly ionized oxygen vacancies and trivalent Ti ions on the Ti sites. However, it is difficult to differentiate between both types of defects because they have similar dependence of electric conductivity on $p(O_2)$ [42]. Singly ionized oxygen vacancy ($V_{\dot{o}}$) is generated according to following reaction [46]:



The equilibrium constant K_2 of the Reaction 2.6 is:

$$K_2 = n[V_{\dot{o}}]p(O_2)^{1/2} \quad (2.7)$$

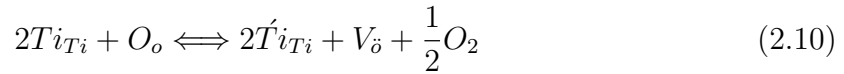
So, the charge neutrality is:

$$[V_{\dot{o}}] = n \quad (2.8)$$

So,

$$n = (K_2)^{1/2} p(O_2)^{-1/4} \quad (2.9)$$

The trivalent Ti ions are generated according to following reaction [46]:



where Ti_{Ti} is lattice titanium and $\dot{T}i_{Ti}$ is titanium trivalent ion.

So, the charge neutrality is:

$$2[V_{\dot{o}}] = [\dot{T}i_{Ti}] \quad (2.11)$$

Supposing that the concentration of trivalent Ti ions are independent of $p(O_2)$ [46] and by joining Equations 2.2 and 2.10, lead to the following relation between $p(O_2)$ and n:

$$n = \left(\frac{2K_1}{[\dot{T}i_{Ti}]} \right)^{1/2} p(O_2)^{-1/4} \quad (2.12)$$

There is also a model which assumes the creation of anti-site defects consisting of Ca^{+2} ions in Ti sites. These can be generated according to the following reaction:



where Ca_{Ca} is lattice calcium and $\dot{C}a_{Ti}$ is anti-site defect.

So, the charge neutrality in this case requires that:

$$[V_{\dot{o}}] = [\dot{C}a_{Ti}] \quad (2.14)$$

where the solubility of CaO in $CaTiO_3$ determines the concentration of anti-site defects and is independent of $p(O_2)$. Then:

$$n = \left(\frac{K_1}{[\dot{C}a_{Ti}]} \right)^{1/2} p(O_2)^{-1/4} \quad (2.15)$$

However, it is reported that the concentration of such kind of defects can be too small because their formation enthalpy is very high, i.e. 4.80 eV.

The formation of Ca vacancies (\dot{V}_{Ca}) is also possible in Ruddlesden-Popper phase which involves excess Ca ions accommodated in between $CaTiO_3$ blocks resulting in the formation of the pairs of Ca and oxygen vacancies through following equilibrium [47], [48]:



The equilibrium constant K_3 is:

$$K_3 = [\dot{V}_{Ca}][V_{\dot{o}}] \quad (2.17)$$

So, the charge neutrality is then:

$$[\dot{V}_{Ca}] = [V_{\dot{o}}] = K_3^{1/2} \quad (2.18)$$

By combining Equations 2.4 and 2.18:

$$n = K_1^{1/2} K_3^{-1/2} p(O_2)^{-1/4} \quad (2.19)$$

Additionally, the following defect model assumes that the mainly negatively charged defects are acceptor type defects and ionic defects are oxygen vacancies [47]–[50]. Therefore, the lattice charge neutrality is:

$$A = 2[V_{\dot{o}}] \quad (2.20)$$

where A is an excess of acceptors over donors:

$$A = [\dot{A}] - [\dot{D}] \quad (2.21)$$

with \dot{A} is acceptor and \dot{D} is donor.

By considering Equation 2.2, the concentration of electrons are the function of $p(O_2)$ according to following equation:

$$n = \left(\frac{2K_1}{A}\right)^{1/2} p(O_2)^{-1/4} \quad (2.22)$$

To summarize, all the derived defect models of $CaTiO_3$ result that the concentration of electrons have the same $p(O_2)$ dependence. Consequently, the obtained data based on the $p(O_2)$ dependence of electric conductivity cannot distinguish between the main defects related to the defect models [42].

2.2.2 Trapping of charge defects

As mentioned in previous Section, defects like oxygen vacancies in $CaTiO_3$ can lead to the generation of electric dipoles. This is only possible when produced defects are highly localized. Otherwise, there will be no electric dipoles and there are nearly equal possibility for all lattice positions to occupy such a quasi-free-electron causing electric conductivity [51].

Therefore, in this work the main interest is to generate highly localized defects and investigate their outcome. In general, charge defects can be trapped which lead to the

resistance of the migration and prevent diffusion of defects. Grain boundaries play an important role for charge trapping and act as pinning points. Similarly, twin walls in solids can also inhibit conductivity or in other words reduce the diffusion of charges [52]. Apart from that, crystalline-crystalline-interfaces of different phases are expressed as a rigid amorphous fraction (RAF) which connects two different crystals. Oxygen atom which is bounded by covalent bond inside this RAF, is known as bridging oxygen and also has a highest possibility of creation of an oxygen vacancy [53]. Moreover, this oxygen vacancy is highly localized and act as hole trapping site.

2.3 Piezoelectric effect

Certain materials become electrically polarized under the mechanical stress and the degree of polarization is directly proportional to the applied stress. The phenomenon is called direct piezoelectric effect and presented in Figure 2.3a. According to the definition, if the stress is changed from tensile to compression then the sign of electric charge appearing on the electrodes reverses. The process is reversible which means that the material can also deform when exposed to an EEF known as inverse piezoelectric effect shown in Figure 2.3b. Similar to direct piezoelectric effect, the sign of strain changes to the opposite one if the direction of EEF is reversed [19], [54].

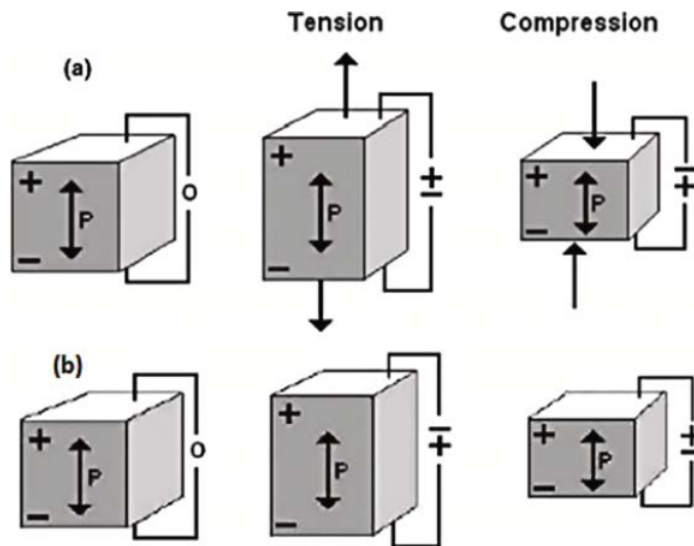


Figure 2.3: Illustration of (a) direct and (b) inverse piezoelectric effects [19].

2.3.1 Symmetries of crystals

In piezoelectric materials, the crystallographic symmetry plays a conclusive role in the generation of piezoelectric effect. All components of the piezoelectric tensor should be zero when crystal has the center of symmetry [54]. There are only 21 non-centrosymmetric classes which may show piezoelectric effect among all crystallographic symmetries. A rough statistical estimation is that about 30% of all materials, which are around several millions known by now, have non-centro-symmetric crystal structure. Although, only few thousands of them reveal piezoelectric properties and only some

hundreds possess piezoelectric activity which is valuable for the applications. Hence, it can be concluded that non-centro-symmetry is a basic requirement for any material to exhibit piezoelectric effect but this is not the only requirement to exhibit any sizable piezoelectric effect [19]. Table 2.2 presents the point groups that either permit or do not permit the piezoelectricity in all crystallographic systems.

They contain built-in polarization. Pyroelectric point groups possess polar axis and

Crystal system	Symmetry elements	Centro-symmetry	Non-centro-symmetry
Triclinic	Center	$\bar{1}$	1
Monoclinic	Center, axis, plane	2/m	2, m
Orthorhombic	Center, axis, plane	mmm	222, mm2
Tetragonal	Center, axis, plane	4/m, 4/mmm	4, $\bar{4}$, 422, 4mm, $\bar{4}2m$
Trigonal	Center, axis, plane	$\bar{3}$, $\bar{3}m$	3, $\bar{3}2$, 3m
Hexagonal	Center, axis, plane	6/m, 6/mmm	6, $\bar{6}$, 622, 6mm, $\bar{6}m2$
Cubic	Center, axis, plane	m $\bar{3}$, m $\bar{3}m$	23, $\bar{4}3m$, $\bar{4}32$

Table 2.2: Crystal system, symmetry elements, centro- and non-centro-symmetric point groups in crystals [19].

are ten in number among the twenty piezoelectric crystal classes. They have temperature induced electric dipole moments in the unit cell in absence of EEF. The crystal is called ferroelectric when spontaneous polarization can be reversed by applying EEF. However, the spontaneous polarization vanishes leading to ferroelectric crystal transformation into paraelectric state above the Curie point temperature (T_c). The transformation to paraelectric state above T_c is caused by centro-symmetric crystallographic structures, which means that they do not have electric dipoles [19].

2.3.2 Piezoelectric ceramics

An important group among all the piezoelectric materials are ceramics. They are mostly polycrystalline ferroelectric ceramics having perovskite crystal structure[55]. This type of crystal structure exhibits piezoelectric effect only if they have off centering anions in the unit cell, which cause the electric dipoles by breaking of perfect symmetry. The

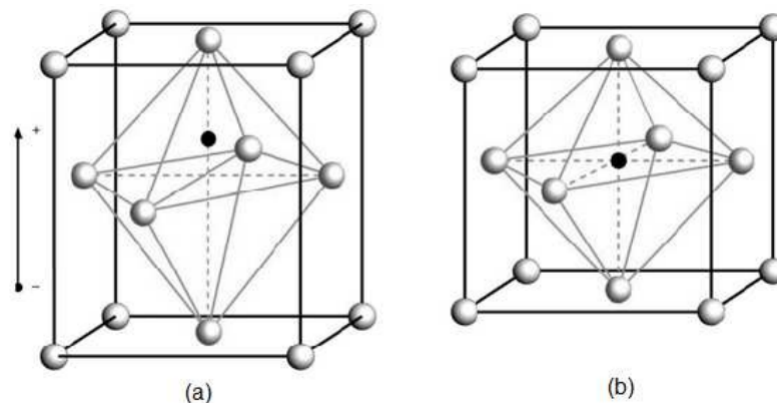


Figure 2.4: Perovskite crystal structure of piezoelectric ceramic (a) tetragonal lattice below T_c and (b) cubic lattice above T_c [56].

perovskite crystal structures with and without electric dipoles can be seen in Figure 2.4a and Figure 2.4b respectively, as well as their dependence on T_c . Additionally, even polycrystalline piezoelectric ceramics have electric dipoles but there is no net polarization due to their randomly orientation. The local alignment of these electric dipoles is called domains. This local alignment gives a net electric dipole moment to the domain and thus referred as net polarization, which is mostly random as presented in Figure 2.5a. These domains can be aligned by applying strong EEF typically at a temperature slightly below the Curie temperature shown in Figure 2.5b. This is known as the poling treatment and the alignment of domains due to poling treatment causes the elongation of material usually within the micrometer range. When EEF is removed after the poling treatment, most of the domains are locked into the configuration of near alignment like, in Figure 2.5c. Hence, the material has become a permanent polarized material and also permanently elongated [35].

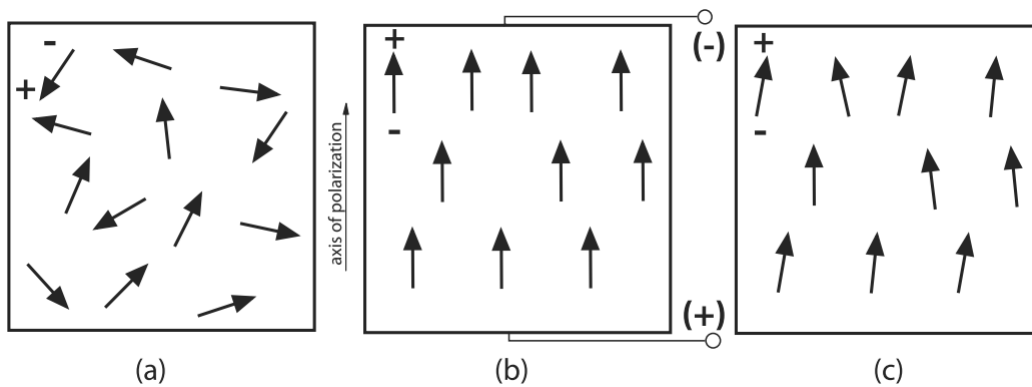


Figure 2.5: Poling treatment of piezoelectric material: (a) before poling with domains are randomly oriented (b) domains alignment with high direct current EEF and (c) after removing of direct current EEF with the remanent polarization [55].

The working principle of poled piezoelectric ceramics can be explained by Figure 2.3. Mechanical tension or compression of the ceramic creates charge due to the changes in electric dipole moment associated with that material. Tension along the perpendicular direction of polarization and compression along the same direction of polarization produce charges of the same polarity as the poling direction, which can be seen in Figure 2.3a (compression). Compression along the perpendicular direction and tension along the same direction of polarization produce a charge with polarity of opposite direction to the poling direction Figure 2.3a (tension). In this mode, the material converts the mechanical energy to tension or compression into electrical energy. This is also known as direct piezoelectric effect. Moreover, the magnitude of mechanical stress and the charge produced are linearly proportional up to a certain stress, which depend on the material itself. Same linear behaviour is true for applied voltage and the strain generated by material. Similarly, if the voltage is applied with the same polarity as the poling direction then the material is elongated Figure 2.3b (tension). If the voltage applied to opposite of the poling direction then the material becomes shorter Figure 2.3b (compression). This is also known as inverse piezoelectric effect and the material converts electrical energy to mechanical energy. Additionally, if an alternating voltage is applied to the poled piezoelectric material then it contracts and expands periodically

with the frequency of applied alternating voltage [35].

2.3.3 Electromechanical equations

Piezoelectric response is direction dependent, so its complete electromechanical equation can only be described with the axis dependence. Conventionally, axis 1 and 2 correspond to x and y axis respectively, which lie in the plane perpendicular to axis 3. Axis 3 which is x axis usually refers to the direction of the polarization. The electromechanical equations for the linear piezoelectric material are described below [35]:

$$D_m = d_{mi}\sigma_i + \xi_{ik}^\sigma E_k \quad (2.23)$$

$$E_i = g_{mi}\sigma_i + \beta_{ik}^\sigma D_k \quad (2.24)$$

$$\varepsilon_i = S_{ij}^E \sigma_j + d_{mi} E_m \quad (2.25)$$

$$\varepsilon_i = S_{ij}^D \sigma_j + g_{mi} D_m \quad (2.26)$$

where indices $i, j = 1, 2, \dots, 6$ and $m, k = 1, 2, 3$ represent different directions of the coordinate system of piezoelectric material.

σ - stress vector

ε - strain vector

E - vector of applied EEF

ξ - permittivity

D - vector of electric displacement

β - impermittivity component

d - matrix of piezoelectric strain constants

S - matrix of compliance coefficients

g - matrix of piezoelectric constants

Superscripts D, E and σ represent the measurements taken at constant electric displacement, constant EEF and constant stress, respectively.

Equations 2.23 and 2.24 represent the direct piezoelectric effect and Equations 2.25 and 2.26 represent the inverse piezoelectric effect, respectively. In the matrix form, these equations can be expressed as:

$$\begin{pmatrix} \varepsilon_1 \\ \varepsilon_2 \\ \varepsilon_3 \\ \varepsilon_4 \\ \varepsilon_5 \\ \varepsilon_6 \end{pmatrix} = \begin{pmatrix} S_{11} & S_{12} & S_{13} & S_{14} & S_{15} & S_{16} \\ S_{21} & S_{22} & S_{23} & S_{24} & S_{25} & S_{26} \\ S_{31} & S_{32} & S_{33} & S_{34} & S_{35} & S_{36} \\ S_{41} & S_{42} & S_{43} & S_{44} & S_{45} & S_{46} \\ S_{51} & S_{52} & S_{53} & S_{54} & S_{55} & S_{56} \\ S_{61} & S_{62} & S_{63} & S_{64} & S_{65} & S_{66} \end{pmatrix} \begin{pmatrix} \sigma_1 \\ \sigma_2 \\ \sigma_3 \\ \sigma_4 \\ \sigma_5 \\ \sigma_6 \end{pmatrix} + \begin{pmatrix} d_{11} & d_{21} & d_{31} \\ d_{12} & d_{22} & d_{32} \\ d_{13} & d_{23} & d_{33} \\ d_{14} & d_{24} & d_{34} \\ d_{15} & d_{25} & d_{35} \\ d_{16} & d_{26} & d_{36} \end{pmatrix} \begin{pmatrix} E_1 \\ E_2 \\ E_3 \end{pmatrix} \quad (2.27)$$

also

$$\begin{pmatrix} D_1 \\ D_2 \\ D_3 \end{pmatrix} = \begin{pmatrix} d_{11} & d_{12} & d_{13} & d_{14} & d_{15} & d_{16} \\ d_{21} & d_{22} & d_{23} & d_{24} & d_{25} & d_{26} \\ d_{31} & d_{32} & d_{33} & d_{34} & d_{35} & d_{36} \end{pmatrix} \begin{pmatrix} \sigma_1 \\ \sigma_2 \\ \sigma_3 \\ \sigma_4 \\ \sigma_5 \\ \sigma_6 \end{pmatrix} + \begin{pmatrix} e_{11}^\sigma & e_{12}^\sigma & e_{13}^\sigma \\ e_{21}^\sigma & e_{22}^\sigma & e_{23}^\sigma \\ e_{31}^\sigma & e_{32}^\sigma & e_{33}^\sigma \end{pmatrix} \begin{pmatrix} E_1 \\ E_2 \\ E_3 \end{pmatrix} \quad (2.28)$$

As mentioned above, material is poled along the axis 3 by convention. Moreover, considering the piezoelectric material as transversely isotropic in the case of piezoelectric ceramics, many of the variables in above matrices can be zero or equivalent to other variables. In general, the non-zero compliance coefficients are:

$$\begin{aligned} S_{11} &= S_{22} \\ S_{13} &= S_{31} = S_{23} = S_{32} \\ S_{12} &= S_{21} \\ S_{44} &= S_{55} \\ S_{66} &= 2(S_{11} - S_{12}) \end{aligned}$$

The non-zero piezoelectric strain coefficients are given as:

$$\begin{aligned} d_{31} &= d_{32} \\ d_{15} &= d_{24} \end{aligned}$$

The non-zero dielectric coefficients are given as:

$$\begin{aligned} e_{11}^{\sigma} &= e_{22}^{\sigma} \\ e_{33}^{\sigma} & \end{aligned}$$

Eventually, the Equations 2.27 and 2.28 are reduced as following [35]:

$$\begin{pmatrix} \varepsilon_1 \\ \varepsilon_2 \\ \varepsilon_3 \\ \varepsilon_4 \\ \varepsilon_5 \\ \varepsilon_6 \end{pmatrix} = \begin{pmatrix} S_{11} & S_{12} & S_{13} & 0 & 0 & 0 \\ S_{12} & S_{11} & S_{13} & 0 & 0 & 0 \\ S_{13} & S_{13} & S_{33} & 0 & 0 & 0 \\ 0 & 0 & 0 & S_{44} & 0 & 0 \\ 0 & 0 & 0 & 0 & S_{44} & 0 \\ 0 & 0 & 0 & 0 & 0 & 2(S_{11} - S_{12}) \end{pmatrix} \begin{pmatrix} \sigma_1 \\ \sigma_2 \\ \sigma_3 \\ \sigma_4 \\ \sigma_5 \\ \sigma_6 \end{pmatrix} + \begin{pmatrix} 0 & 0 & d_{31} \\ 0 & 0 & d_{31} \\ 0 & 0 & d_{33} \\ 0 & d_{15} & 0 \\ d_{15} & 0 & 0 \\ 0 & 0 & 0 \end{pmatrix} \begin{pmatrix} E_1 \\ E_2 \\ E_3 \end{pmatrix} \quad (2.29)$$

also

$$\begin{pmatrix} D_1 \\ D_2 \\ D_3 \end{pmatrix} = \begin{pmatrix} 0 & 0 & 0 & 0 & d_{15} & 0 \\ 0 & 0 & 0 & d_{15} & 0 & 0 \\ d_{31} & d_{31} & d_{33} & 0 & 0 & 0 \end{pmatrix} \begin{pmatrix} \sigma_1 \\ \sigma_2 \\ \sigma_3 \\ \sigma_4 \\ \sigma_5 \\ \sigma_6 \end{pmatrix} + \begin{pmatrix} e_{11}^{\sigma} & 0 & 0 \\ 0 & e_{11}^{\sigma} & 0 \\ 0 & 0 & e_{33}^{\sigma} \end{pmatrix} \begin{pmatrix} E_1 \\ E_2 \\ E_3 \end{pmatrix} \quad (2.30)$$

Piezoelectric constant

The piezoelectric constant (d_{ij}) can be described as a ratio of generated strain in j direction to the applied EEF along i direction. If the voltage is generated in thickness (1) direction which is also the direction of polarization, then it produces an electric field [35]:

$$E_3 = \frac{V}{t} \quad (2.31)$$

and this leads to the strain in piezoelectric ceramic:

$$\varepsilon_3 = \frac{\Delta l}{l} \quad (2.32)$$

Hence,

$$d_{33} = \frac{\Delta l}{V} \quad (2.33)$$

Furthermore, d_{ij} can also be interpreted as the ratio of per unit surface charges between the connected electrodes perpendicular to j direction to the applied stress in i direction. When subjected to the force, it generates stress according to following relation:

$$\sigma_3 = \frac{F}{l} \quad (2.34)$$

and this leads to the generation of electric charges on the surface of piezoelectric material [35].

$$d_{33} = \frac{q}{F} \quad (2.35)$$

2.3.4 Domain walls and their contribution

The boundaries of domains described earlier are called domain walls which can be moved by applying strong EEF. As a result, spontaneous polarization is reoriented in the direction closest to the applied field direction [19]. In dielectric and ferroelectric materials, domain walls and domain wall motion significantly contribute in their properties [44], [57], [58]. Dielectric permittivity strongly rely on the domain wall motion because charged domain walls result in the increase of conductivity [59]–[61]. Similarly, non-linear elasticity and elongation are caused by ferroelastic domain wall motion [62], [63]. The movement of domain walls contribute significantly in piezoelectric response of the material as well [64]. For instance, in the case of tetragonal crystals, i.e. $BaTiO_3$, only 180° and 90° domain walls are possible. The orthorhombic crystal, i.e. $CaTiO_3$, can contain 180° , 90° , 120° or 60° domain walls. In rhombohedral crystal, i.e. $Pb(Zr_{1-x}Ti_x)O_3$, only 180° and 71° or 109° domain walls are possible. However, it has been revealed that the ferroelectric 180° domain walls do not contribute effectively in piezoelectric response. Whereas, the ferroelectric-ferroelastic non- 180° domain walls contribute significantly to the piezoelectric response [65]–[67].

2.3.5 Piezoelectricity in $CaTiO_3$

It has been reported that artificially synthesized material, e.g. HA, which has centro symmetric crystal structure, can exhibit piezoelectric effect [22]. This implies that the centro symmetry of crystal can break by shifting positive and negative charges through the generation of lattice strain. As a result, electric dipole moments are formed which leads to the piezoelectric effect.

This work is focused on the possibility of generating piezoelectric response of $CaTiO_3$ (for reason, discussed in previous Chapter) which will be referred as “**pseudo piezoelectricity**”. To generate this effect, the instability of regular TiO_6 octahedra is necessary for creating electric dipoles, which results from the off-centering of titanium positions. Therefore, there is a need to produce localized point defects like oxygen

vacancies and freeze them, which can cause the shift of positive and negative charges, i.e. generation of electric dipoles. Moreover, synthesis and densification procedure play an important role in terms of grain boundaries or trapping of charge defects which is discussed in Chapter 5 and 6.

Chapter 3

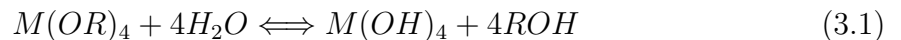
Synthesis techniques and sample preparation

This chapter focuses on the methods used for the synthesis of $CaTiO_3$ samples and their densification. On one hand, synthesis methods and their techniques are explained. On the other hand, detailed procedure of its preparation is discussed. The application of electrodes and procedure of polishing for further characterization are also illustrated in this chapter.

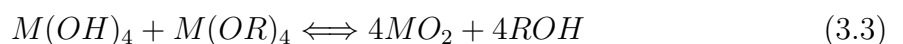
3.1 Sol-gel synthesis

The sol-gel method is a wet-chemical route for the bottom-up synthesis of non-metallic and inorganic materials, e.g. ceramics. It is widely used in laboratories and industries due to the possibility of creating nanostructured powders [68]. The advantage of sol-gel synthesis is that it reduces the sintering time and temperature. This leads to the decrease in thermal decomposition temperature and reduce phase transformation temperature, resulting in the smaller particle sizes and improvement of the diffusion process during sintering [69]. Basically, it is the formation of an oxide network through poly-condensation reactions of precursors in a liquid. Precursors which consist of organic metals or metalloids surrounded by legend, result in the creation of a solid network of nanoparticles due to hydrolysis and condensation. A sol is a stable dispersion of colloidal particles in a solvent. Whereas, a gel is the three dimensional continuous network built from agglomeration of colloidal particles [70].

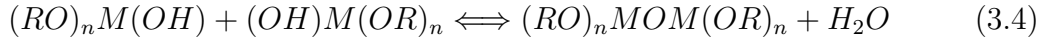
Hydrolysis starts when an organic metal reacts with water to form metal-hydroxide and organic molecules, shown in Equation 3.1.



where M is metal, R is legend, $M(OR)_4$ is organic metal precursor, $M(OH)_4$ is metal hydroxide molecule and ROH is organic product. At this stage, the sol is prepared and metal hydroxides are then transformed into gel by condensation or poly-condensation processes. Equations 3.2 and 3.3 are shown for dehydration and dealcoholization processes, respectively.



These equations are an ideal case of the formation of pure metal oxide particles due to condensation. However, in real system, monomers with hydroxide- and alkoxide-bondings are formed with monomer MOM and alkoxide-bondings $(RO)_n$, as presented in Equation 3.4.



The formation of gel due to agglomeration or Ostwald-ripening like chains can be influenced by different parameters, i.e. pH-value, water or alcohol to precursor ratio or synthesis temperature [71]–[73].

3.2 Spray drying

Spray drying is a continuous particle-processing drying operation. The feed can be suspension, dispersion, solution or emulsion and the end product can be produced in form of powders, agglomerates or granules. In spray dryer, there is almost an instantaneous transition between liquid and solid phases leading to amorphous material. The two important parameters which can affect the properties of end product are inlet and outlet temperatures of air [74]. It has the advantage of production of powder with reduced particle size as compared to drying in room temperature. Ultimately, this reduction of particle size can affect the properties of product.

3.3 Field assisted sintering technique

FAST is a low voltage, pulsed (on-off) direct current and uniaxial pressure sintering technique to densify powders under very low atmospheric pressure without melting. This becomes possible through the thermal activation of mass transport processes driven by reduction of surface and grain boundary energies. Sintering process requires high temperatures to obtain high density and to optimize thermal activation. To achieve high densification at lower temperatures and in shorter sintering time, electric current is the key to activate sintering [26], [29]. The advantages of FAST are cleaner grain boundaries in sintered ceramics, higher permittivity in ferroelectrics, increase in superplasticity of ceramics, enhanced thermoelectric properties, improved bonding quality or reduced impurity segregation at grain boundaries. Above all, the primary advantages of FAST are high heating and cooling rates which enhance the densification over grain growth. Therefore, it is possible to achieve high density of phase and grain boundaries which directly influence the physical properties of the densified material. [29], [75]. The technique consists of graphite dies which are attached to the mechanical loading system to compress powder placed inside these dies in the vacuum chamber and for delivering large electric currents. To apply mechanical load and pulsed direct current to a graphite die containing powder to be densified, two water cooled copper electrodes are used within the chamber, shown in Figure 3.1. Due to the good conductivity of material (graphite die) used in FAST and high power pulsed direct current (< 24 kA) in few milliseconds (ms) produced with very low voltage (< 8 V) during mechanical loading leads to Joule heating. Heating and cooling rates are in 1000° C/min and 400° C/min (under gas flow), respectively and the maximum force that can be applied is < 1250 kN. The sintering temperature is $< 2400^\circ$

C and heating power < 180 kW. When electrically insulating die is used, highest current density can be achieved by forcing the current to flow through the material [26]. During sintering, four mechanisms are involved due to the applied mechanical, thermal and electrical effects: (1) vaporization and solidification, (2) volume diffusion, (3) surface diffusion and (4) grain boundary diffusion on neck formation. In mechanical effect (applied pressure), it causes better contact between powders, which leads to enhance the grain boundary and lattice diffusion. The pressure in the range of MPa causes the particle rearrangement at low temperature, which results in reduction of pore sizes, increased packing and suppressed grain growth. Joule heating also plays an important role during FAST sintering by increasing densification. Heat flows through the material in a complex network because the material (powder) is not dense and completely homogeneous. As a result, due to high local current densities, fluctuating hot spots form within the network leading to the formation of microstructure instead of particle melting and recrystallization in standard sintering scenarios [26]. However, the exact influence of current on the sintering behaviour of powder is still largely unknown. Pulse duration and other parameters can strongly modify the conditions of sintering. Furthermore, the effects of plasma and spark generation are still under debate and investigation [28], [29], [75], [76].

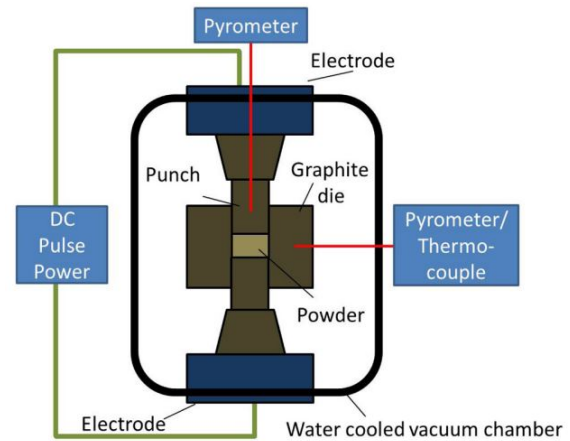


Figure 3.1: Schematic Diagram of FAST [26]

3.4 Conventional sintering

Most commonly used technique for sintering the sample is conventional sintering. In this sintering technique, sample is heated by a heat source which can heat the sample from outside. Electromagnetic radiation from heat source, i.e. electric heating rods, heats the sample and sinter. In conventional sintering, small heating rates (hours) are needed because the heat transfer from outside of the material to inside requires time, especially when ceramics are processed. This long time sintering process causes exaggerated grain growth and also consumes a lot of energy [77].

3.5 Preparation of $CaTiO_3$

3.5.1 Sol-gel synthesis

Calcium nitrate tetrahydrate ($Ca(NO_3)_2 \cdot 4H_2O$) with a purity of 99.0% and titanium isopropoxide ($Ti(OC_3H_7)_4$) with a purity of 97.0% were used in a sol-gel process as precursors. Equal ratios of calcium and titanium (1:1) were used to synthesize $CaTiO_3$.

$\text{Ca}(\text{NO}_3)_2 \cdot 4\text{H}_2\text{O}$ and $\text{Ti}(\text{OC}_3\text{H}_7)_4$ were mixed separately in ethanol using a magnetic stirrer and an ultrasonic bath for 0.5 h. Then, the solution of $\text{Ca}(\text{NO}_3)_2 \cdot 4\text{H}_2\text{O}$ was added drop-wise in $\text{Ti}(\text{OC}_3\text{H}_7)_4$ solution and stirred at room temperature for 24 h at 250 rpm.

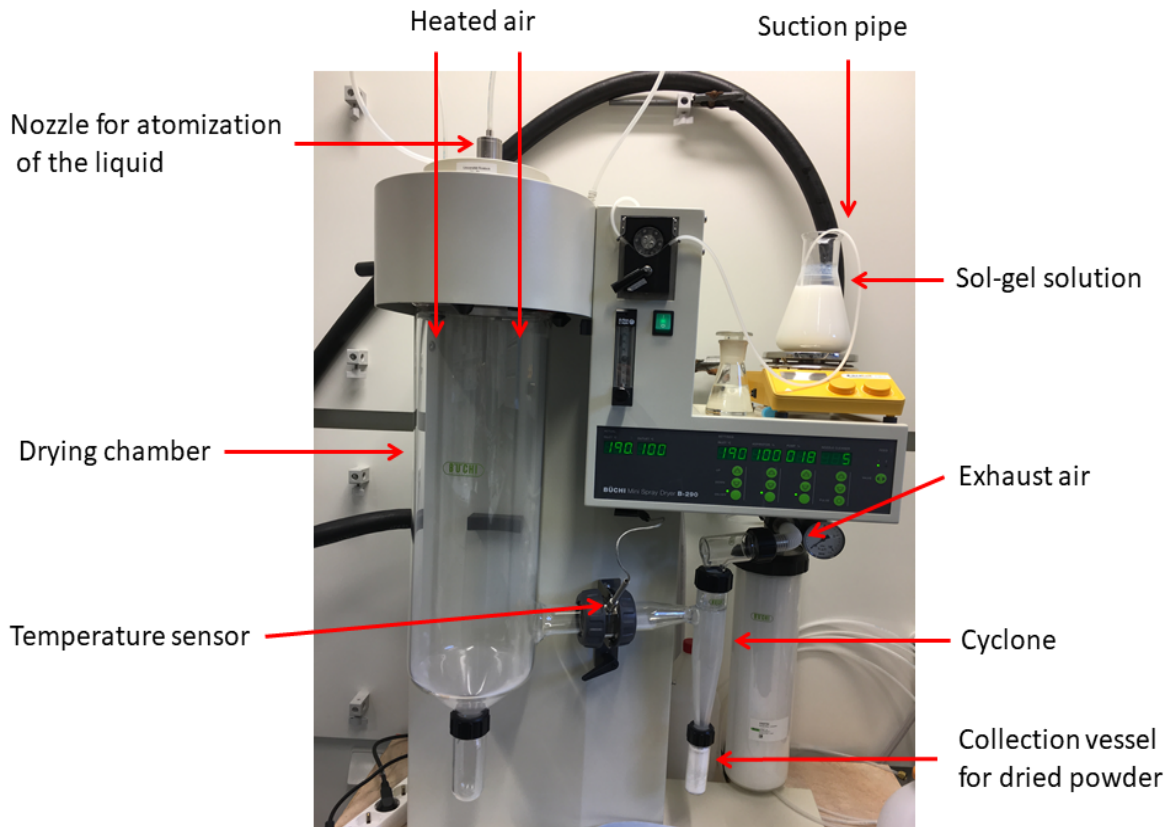


Figure 3.2: Photograph of spray dryer during the drying process of sol-gel prepared solution.

The resulting solution was then dried with spray dryer from Buchi (mini spray dryer B-290). The liquid of sol-gel solution passed through the suction pipe and contacted with air flow so that the moisture evaporates. When the gas flew with the solid, it entered the cyclone separator and the particles were then set in rotation and experienced centrifugal acceleration in the direction of the cyclone wall. As the cyclone constricts downwards, the velocity of particles increased and dried powder was passed into a collecting vessel [78]. For the moisture evaporation, the inlet temperature was set to $190\text{ }^\circ\text{C}$ and outlet temperature was $100\text{ }^\circ\text{C}$ to control final moisture content of the powder [74]. The setup of spray dryer is shown in Figure 3.2.

The powder was further dried in an oven at $180\text{ }^\circ\text{C}$ for 2 h to complete moisture evaporation. Afterwards, the powder was calcinated with heating rate of 5 K/m with holding temperature of $650\text{ }^\circ\text{C}$ for 2 h in air. At the end, powder was cooled down to room temperature with cooling rate of 10 K/m .

3.5.2 Field assisted sintering

The calcinated powder was densified using a HP D5 FAST unit from FCT Systeme GmbH Rauenstein, located in Tycho Sinterlab Rostock, Germany. Graphite die with diameter of 10 mm was filled with calcinated $CaTiO_3$ powder. Additionally, graphite foils were placed between the powder and inner walls of the die and punched to prevent the powder from reacting with the die and also to ensure good electric contact. The sintering was performed in vacuum of approximately 1 mbar. The applied pressure was 76 MPa and the heating rate 100 K/min.

Initially, the sintering temperature was varied to ensure good densification like in [79]. The temperature was varied from 1000 °C to 1100 °C. However, as temperature increases, the carbon diffusion also increases from the graphite foil to the sample, resulting in a change of colour of $CaTiO_3$ from white to grey. This also affects the electrical properties of $CaTiO_3$. Motivated by the mentioned experience, a sintering temperature of 1025 °C was selected to achieve maximum densification and avoid carbon diffusion. The sintering temperature was held for 5 minutes. Afterwards, the sample was cooled down. It is important to mention that due to technical limitations, the heating process above 400 °C was controlled by optical pyrometer and below 400 °C was monitored by a thermocouple. The optical pyrometer was focused in a hole drilled in the upper part of a graphite punch and thermocouple was attached to the graphite die. The whole process was monitored through computer during sintering. At the end, $CaTiO_3$ was cleaned from the protective graphite foil using a sand blaster. The sample after sintering was cylindrically shaped with almost 10 mm diameter and 8 mm thickness. For further characterization, this sample was precisely cut by using a diamond band saw in cylindrically shaped specimen with the dimensions of 10 mm diameter and 2 mm thickness for piezoelectric measurements. Another specimen was also created in 3d rectangular shape with the dimensions of 10 mm length, 2 mm height and 1.5 mm width for X-ray diffraction experiment. The images of both samples are shown in Figure 3.4a.

The density of $CaTiO_3$ was calculated by Archimedes principle:

$$\rho = \frac{m \cdot \rho_w}{m - M_w} \quad (3.5)$$

where ρ and ρ_w are the densities of sample and water, respectively. Moreover, m and M_w are the masses of sample in air and water. The relative density was $(91.2 \pm 0.4)\%$.

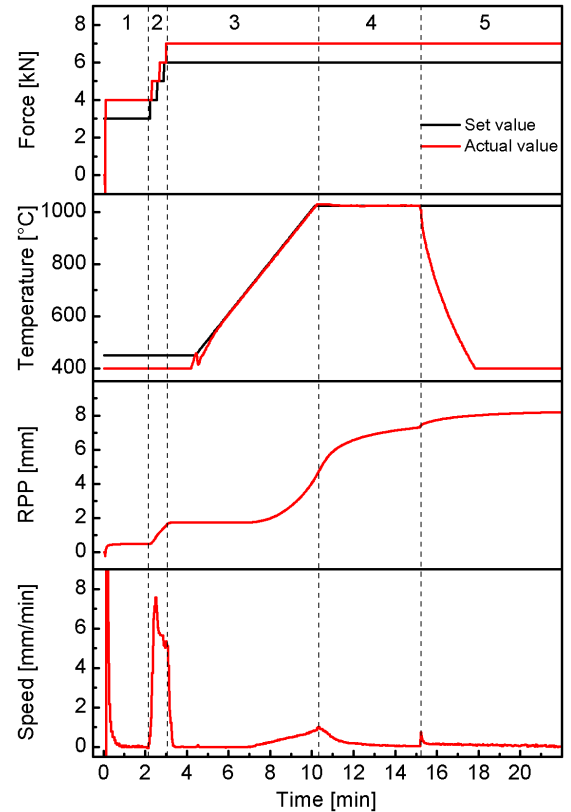


Figure 3.3: Response of $CaTiO_3$ powders at the time of sintering, sintered at 1025 °C.

The response of $CaTiO_3$ powder during sintering is shown in Figure 3.3. The figure represents the speed of moving piston, relative piston position (RPP), temperature and force. The force increases till 6 kN and is then kept constant. Temperature was measured by pyrometers starting from 400 °C onward. The initial peak of temperature curve is due to different pyrometer values: the gap between pre-heat and high temperature heating. This is due to the technical limitations as mentioned before. In speed curve, the speed of moving piston gives information about the process of densification. To gain a better understanding of RPP, Figure 3.3 is divided into 5 segments: segment 1 is the starting of process, 2 is the change in RPP because of applied force. In segment 3, the change in RPP is due to sintering till the end of segment 3. Segment 4 shows the holding time and 5 indicates the cooling. The RPP is used for indirect measurement of densification during sintering. The position indicates the changes in sample; positive and negative direction indicates the shrinkage or expansion respectively [80]. From the Figure 3.3, it can be clearly seen that the densification starts in segment 4 at approximately 750 °C when RPP starts changing. This densification is almost completed near the end of segment 4.

3.5.3 Conventional sintering

For comparison, the calcinated $CaTiO_3$ was sintered using conventional sintering. In the beginning, a green pellet was produced using a press model PW 40 manufactured by P/O/WEBER GmbH. The powder was filled in a stainless steel die with a diameter

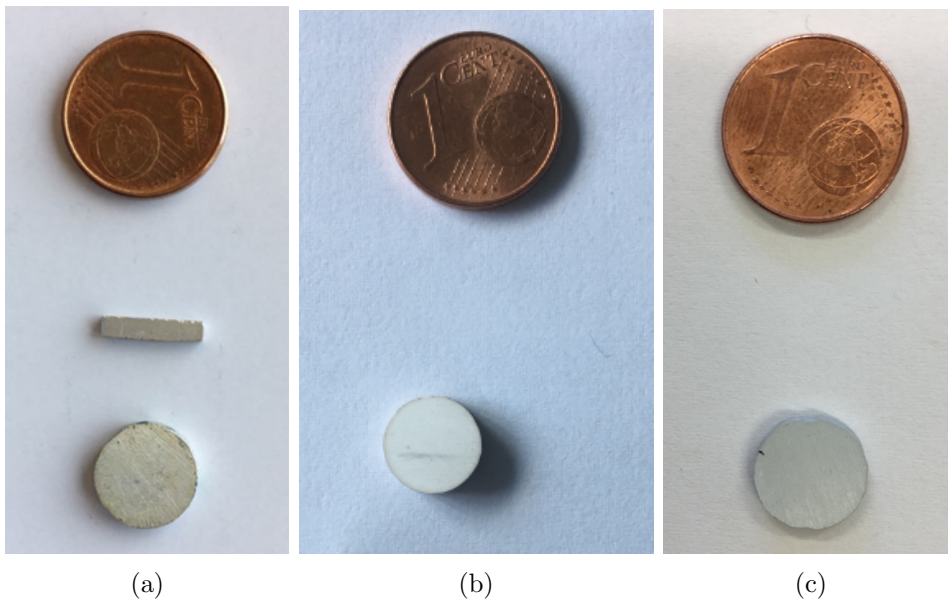


Figure 3.4: Images of (a) sputter coated FAST sintered samples, (b) conventionally as well as (c) FAST sintered $CaTiO_3$ after sintering with coins of one cent.

of 10 mm and pressed with a pressure of approximately 510 MPa for 5 minutes. Then, the green pellet was removed from the stainless steel die and placed in an oven model RHTH 120/600/18 manufactured by Nabertherm GmbH. The sample was heated to a sintering temperature of 1200 °C with a heating rate of 7 K/min. The temperature was kept constant for 4 h. Afterwards, the sample was cooled down to room temperature. The sample after conventional sintering was also cylindrically shaped like FAST sintered

$CaTiO_3$ with almost 10 mm diameter and 8 mm thickness. For further characterization, it was precisely cut in cylindrical shape with exactly same dimension as FAST sintered $CaTiO_3$. The density of conventionally sintered sample was also calculated using Equation 3.5 and its relative density was $(83.7 \pm 0.5)\%$. The images of conventionally and FAST sintered $CaTiO_3$ samples after cutting with diamond band saw and coin of one cent are shown in Figure 3.4b and Figure 3.4c, respectively.

3.5.4 Polishing

To polish the surfaces of samples, they were gradually removed by grinding with different grain sizes: with (Silicon Carbide) SiC wet grinding paper from 320 ($46 \mu m$) to 2500 ($10 \mu m$). It was then polished with alcoholic diamond suspension of grain size $6 \mu m$ and $3 \mu m$. Finally, polishing was done with active oxide polishing suspension ($0.05 \mu m$).

3.5.5 Sputter coating

Sputter coating was used to apply the electrodes on both sides of cylindrical as well as 3d rectangular shaped samples for piezoelectric and HEXRD experiments, respectively. The sputter coater, model SC7620 manufactured by quorum technologies limited, was equipped with a silver source, and sputtering was performed in an argon environment. The final thickness of silver electrodes on the $CaTiO_3$ samples was approximately 270 nm. The image of sputter coated samples for piezoelectric and in-situ HEXRD experiments is shown in Figure 3.4a. It is important to mention that the electrodes were applied in the FAST sintering field (SF) direction. Hence in all experiments, EEF was always applied in parallel to SF direction.

Chapter 4

Experimental methods and set-ups

Methods used for the characterization of $CaTiO_3$ powder, conventionally and FAST sintered samples are discussed in this Chapter. The working principles of well established characterization techniques along with the measurement procedures used during this work are briefly introduced. Furthermore, it also explains the design and usage of customized build setups like direct piezoelectric measurement technique with dynamic method and the in-situ X-ray diffraction measurements.

4.1 Differential scanning calorimetry

DSC is a technique for characterization of the physical properties of a material. It allows to determine the crystallization point, melting point and phase transition temperatures. It can also determine the changes in their corresponding enthalpy and entropy [81]. This can be measured as an energy change of the system in comparison to reference by differential thermal analysis (DTA). DSC captures the heat flux between sample and reference as a function of temperature of the reference, while DTA measures the temperature difference between them. By employing this method, the characteristic temperatures and calorimetric parameters of a sample are obtained.

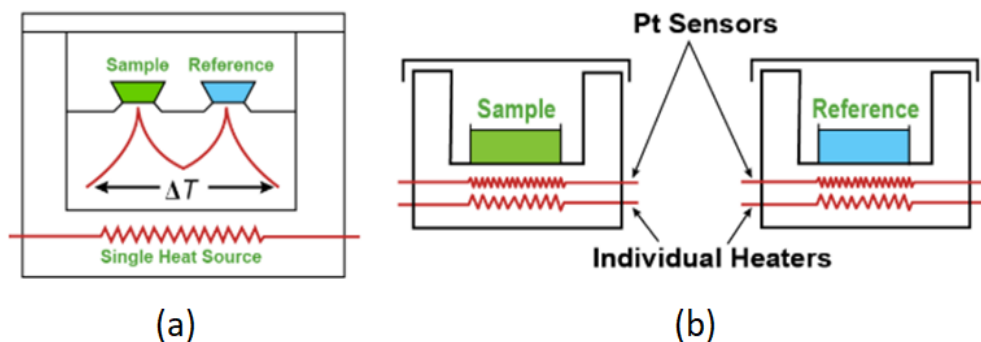


Figure 4.1: Schematic diagram of (a) heat flux and (b) power compensation types DSC [82].

There are two types of DSC techniques: the heat flux and power compensation, which are shown in Figure 4.1. In heat flux DSC, both sample and reference crucibles

are heated by a single heating source through heat resistor and sink [82]. Therefore, it is important that the sample and reference are in good thermal contact for an optimal heat transition. To maintain nearly identical temperature between the sample and reference, the difference in energy is required which is provided by the heat changes in the sample. If there is an excess of energy, then it is conducted between the sample and reference via conducting metallic disc [83].

In powder compensation DSC, both the sample and reference crucibles are heated by individual heaters. If any physical change occurs in the sample, then the platinum resistance thermometer in the detector detects the change. Afterwards, energy is removed or applied from the sample furnace to compensate the change in heat flow from the sample. The system directly measures energy flow from or to the sample. This leads to the system at “thermal null” state at all times. The energy changes occurring in the sample are directly proportional to the amount of power required to maintain system equilibrium [82], [83]. In both types of DSC, when the sample undergoes a phase transition, then heat is required to flow towards the sample for maintaining the same temperature of sample and reference. The amount of heat needed depends on the process which can be either exothermic or endothermic. For instance, if the sample goes through exothermic or endothermic process, then less or more heat is needed to raise the sample temperature, respectively. This change in heat flow between the sample and reference enables DSC to measure the amount of heat absorbed or released during phase transitions [82].

The typical DSC curve is shown in Figure 4.2. When the sample is heated, its temperature increases and at a certain temperature, the plot shifts downward suddenly. This happens when the sample has just gone through the glass transition temperature. If the temperature is increased further, the atoms try to arrange themselves in ordered form and when correct temperature is reached, they give off enough energy for ordered arrangements which can be observed in Figure 4.2 as a peak in the curve. This is called the crystallization of material. When the sample is heated further, then a temperature is reached when the material undergoes melting which can be seen as a dip in the DSC curve. This temperature is called the melting temperature of material [84]. Apart from crystallization and melting peaks in DSC curve, some peaks can also be observed which may be due to the crystal phase transition depending on material.

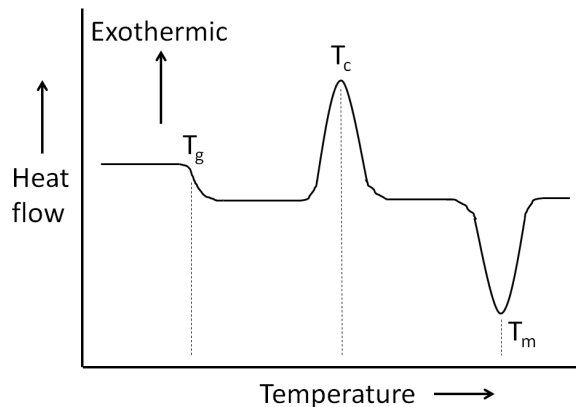


Figure 4.2: Typical DSC heat flow vs temperature curve.

4.2 Scanning electron microscope

SEM is a useful tool for the measurement of material microstructures like particle sizes of powder or grain sizes of densified material. In SEM, an electron beam is irradiated with the energy range of several keV over the sample, as shown in Figure 4.3a. It consists of: detectors, sample holder, electron gun and magnets for focusing electron

beam on the sample.

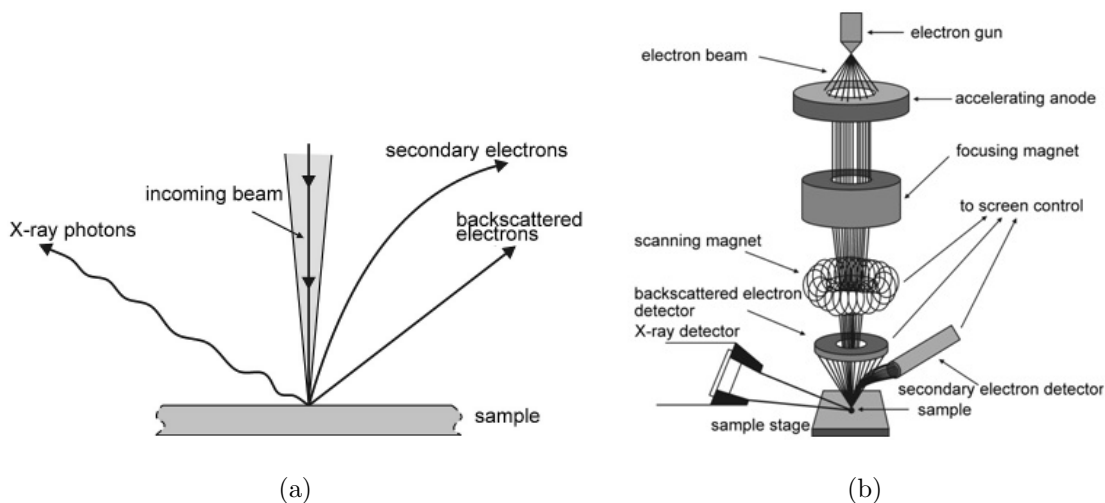


Figure 4.3: (a) Production of electron and X-rays due to interaction of electron-material and (b) setup of SEM [85].

When the electrons are accelerated, they are focused by magnetic lenses (according to Lorentz force) placed in the path of electrons. Subsequently, the electrons interact with the surface of sample which produce back-scattered and secondary electrons as well as X-ray photons, as shown in Figure 4.3b. These signals are collected by the detectors and the map is constructed on screen in the form of image. The back-scattered and secondary electrons contain different energy ranges of approximately 10-30 keV and 3-5 eV, respectively. Back-scattered electrons are electrons produced by elastic scattering and provide information from the deeper layers. However, secondary electrons are emitted due to inelastic scattering of incoming electrons and actually are electrons knocked out from the surface of sample. Hence, they provide information of near surface part of the sample only [85], [86].

4.3 Energy dispersive X-ray spectroscopy

EDX spectroscopy is used for elemental analysis or chemical characterization of a sample. In EDX, same electron beam source (SEM) can be used. The atoms of the sample are bombarded with incident electrons which release electrons of the sample in the excited state. When the atoms relax to their ground state, they release energy in the form of X-rays, Auger electrons or cathode luminescence. The X-rays are then used to identify the elemental concentrations in material. Additionally, chemical analysis can be performed by using Auger electrons [87].

4.4 X-ray photoelectron spectroscopy

XPS is a technique to investigate the chemical composition and stoichiometric relation of a material. Monoenergetic soft X-rays are irradiated on the sample and binding energy of detected electron is analyzed. The penetration power of X-rays on the material in this technique is in the range of μm . Thus, they mostly interact with the electrons of surface

atoms and cause them to emit through photoelectric effect. Apart from photoelectric effect, another event can also be detected that is caused by Auger effect. Auger effect is caused due to filling of inner shell vacancy of an atom by the emission of an electron from the same atom. Both effects are presented in Figure 4.4 [88].

There is a probability or cross-section of a photon to hit an electron in the specific orbit relative to 1s-orbit. Moreover, the Fermi level of an atom is considered to be zero binding energy and depth beneath the Fermi level indicates the binding energy of an electron of different atomic orbits. The energy of photoelectron can be measured by using Equation 4.1.

$$KE = h\nu - BE - \phi_s \quad (4.1)$$

where KE is kinetic energy, h is planks constant, ν is wavelength of X-rays, BE is binding energy of the atomic orbital and ϕ_s is work function of spectrometer [88].

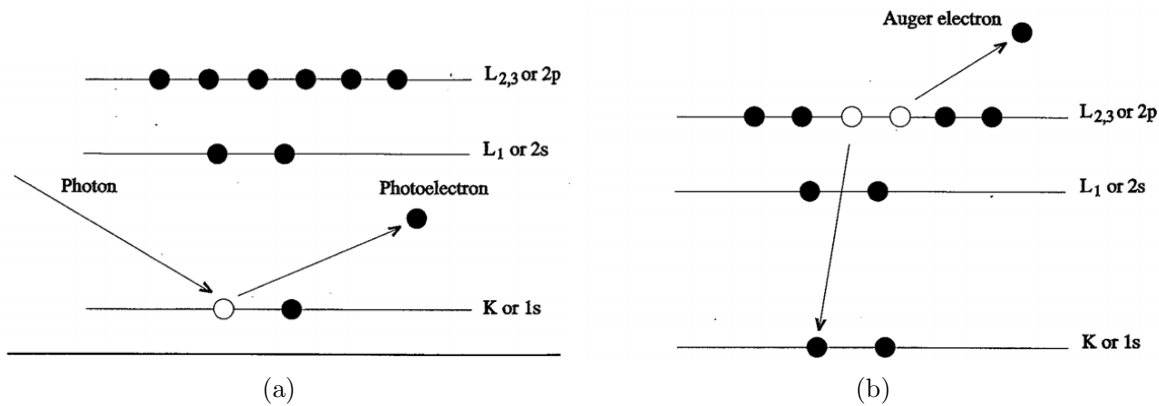


Figure 4.4: (a) Ejection of photoelectron caused by incoming photon and (b) filling of inner shell vacancy by electron of the same atom with emission of Auger electron by transferring the released energy to it [88].

4.5 Piezoelectric measurements

The piezoelectricity of any material can be measured by both direct and inverse piezoelectric effects. In direct piezoelectric effect, the electric charge develops when mechanical stress is applied to the material. The piezoelectric constant (d_{ij}) can be calculated by Equation 4.2 [89]

$$Q = d_{ij} \cdot F \quad (4.2)$$

where Q is the charge produced by applied force (F).

In inverse piezoelectric effect, the mechanical deformation of the crystal lattice occurs due to a strong EEF [55]. The strain in a material is taken to be zero when no EEF is applied, which is point A in Figure 4.5a. If EEF is applied then the crystal expands due to piezoelectric effect, which is shown as strain traces line ABC. This expansion continues up to its saturation which is point C. If EEF starts decreasing, then the sample traces the same line but in opposite direction, i.e. from point C to A. At this point, the strain in a material is again zero. When the EEF direction is changed (negative direction) then the crystal compresses with respect to point A and up to point D. The

EEF is large enough at point D to switch the direction of polarization and the strain becomes positive again which is point E. If EEF is increased further, then the strain increases to point F and decreases back to point A which is the initial point. The same sudden switching of polarization happens at point G if EEF is applied further. As shown in Figure 4.5a, the S-E curve is linear indicating that the strain is purely piezoelectric except points D and G, i.e. switching points. However, in reality the S-E curve is more complex. Real materials contain the movement of non-180° and 180° domains which significantly change the dimension of material as compared to the ideal situation. In real material, the domains switching is not sudden as in ideal case shown in Figure 4.5a because the coercive field can vary for different domains. In general, as shown in Figure 4.5b, the strain produced in a material due to the displacement of domain walls is strongly non-linear [54]. As mentioned above, the piezoelectric constant (d_{ij}) is calculated by Equation 4.3.

$$S = d_{ij}E_i = d_{ji}^t E_i \quad (4.3)$$

where S is resulting strain in a material, d_{ij} or d_{ji} is piezoelectric constant (third rank tensor), E_i is applied EEF and t is transposed matrix.

The d_{33} is calculated from the strain (S)-electric field (E) curve. The average d_{33} can be defined as the slope of the unipolar S-E curve. By using Equation 4.3, following equation can be derived:

$$d_{33} = \frac{S_2 - S_1}{E_2 - E_1} \quad (4.4)$$

If $E_2 - E_1$ is positive then the value of piezoelectric constant is d_{33+} and if $E_2 - E_1$ is negative then the value of piezoelectric constant is d_{33-} , as shown in Figure 4.5b. Where, d_{33+} and d_{33-} are related to the increase and decrease in dimensions, respectively.

The piezoelectric constants d obtained from both direct and inverse piezoelectric effects are thermodynamically identical ($d_{direct} = d_{inverse}$). Moreover, the units of direct and inverse piezoelectric constants are C/N and m/V, respectively [54], [55].

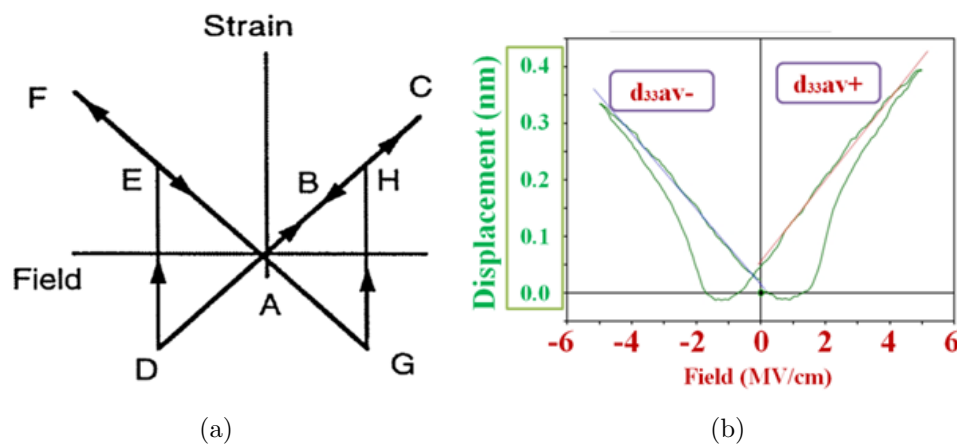


Figure 4.5: S-E curve in ferroelectrics (a) ideal loop of a crystal in which polarization reverses only by 180° domains and (b) in real material [54].

4.6 High energy X-ray diffraction

4.6.1 Synchrotron radiation

In order to get the detailed information about the structure in crystalline solids, the wavelength of scattering probe λ should be in the range of Angstroms. The typical range of X-rays in the electromagnetic spectrum is 10 keV having a wavelength of 1.24\AA . Therefore, X-rays are suitable candidate for investigating the structure of condensed matter like crystalline, amorphous or liquid materials.

Synchrotron radiation is emitted by charged particles accelerated on circular paths. The energy of these particles is in the range of GeV and the velocity is close to the speed of light. The relativistic form of the equation can be expressed as [90]:

$$P \simeq \frac{2e^2c}{R^2} \left(\frac{v}{c}\right)^4 \left(\frac{E_{el}}{mc^2}\right)^4 \sim \frac{(\gamma)^4}{R^2} \quad (4.5)$$

where R is the radius of storage ring, m is the rest mass, e is the charge of electron, v is the velocity of electron, E_{el} is the energy of particles, m is the mass of electron and $\gamma = E_{el}/mc^2$.

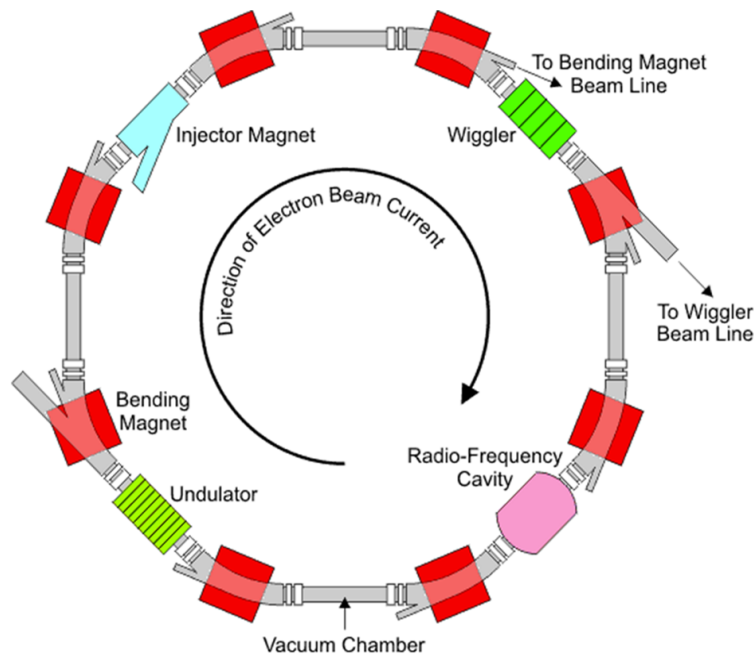


Figure 4.6: Visual representation of synchrotron storage ring [91].

X-rays generated with the help of synchrotron radiation are much more intense as compared to the ones generated by other laboratory sources. Due to this reason, they can be used to measure the powder diffraction accurately. Synchrotron radiation is emitted by charged particles when they are forced to follow a circular path in which they change their velocity as shown in Figure 4.6. The magnetic fields present in the storage ring are used to guide the electrons in circular path. Two geometries of magnetic fields, i.e. straight and curved, are used to perform this task. In the straight portion of storage ring, the alternating magnetic field is used to generate synchrotron radiation

from an oscillating electron. The normally used X-rays sources are bending magnets and insertion devices, i.e. wigglers and undulators. The orientation of magnetic fields generated by these components is vertical, which produces deflection of the electrons in horizontal plane [91].

4.6.2 Debye-Sherrer geometry

Previously used Debye-Sherrer cameras have now been transformed into transmission powder diffractometers that use perfect crystal monochromators. A monochromator is a single flat crystal that uses diffraction for performing the reflection of wavelengths. It reflects only those beams that satisfy the Bragg condition, i.e. $\lambda = 2d \sin \theta_m$. Commonly used crystals are silicon, germanium, quartz, diamond and graphite.

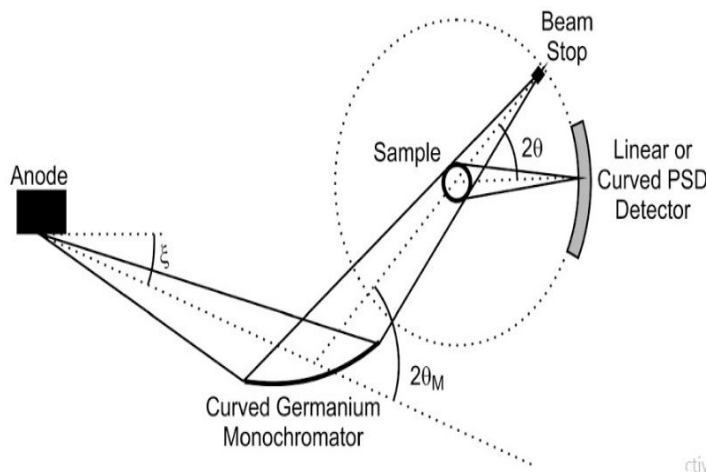


Figure 4.7: Debye-Sherrer diffractometer with a curved monochromator and capillary sample [91].

The X-rays are focused on 2θ measuring circle that lies after the sample. The measuring circle is used for more efficient data collection and in the ideal case, it has the shape of curved position sensitive detectors (PSD). In case of utilization of a straight PSD, it is positioned further away from the focusing circle. The sample powder can also be rotated about its axis to obtain a good powder average. The diffraction peaks can be obtained with a width of 0.1 degree. The orientation of samples is important. The correct orientation can help in achieving better transmission. The correction for absorbed intensities can also be made if the sample is placed in a proper orientation. Figure 4.7 shows the Debye-Sherrer geometry [91].

4.6.3 Rietveld refinement

Rietveld refinement method is used to refine the parameters of data obtained by HEXRD experiment to extract the information related to the structure of sample. In a polycrystalline sample, it is difficult to obtain detailed structural information due to loss of information as a result of random orientation of the crystalline material. More specifically, information is lost due to the overlapping of independent diffraction peaks of

powders [92]. However, Rietveld refinement method is modified to extract the maximum information from powder diffraction, which overcomes the fact that any detail in the profiles of these peaks is lost [93]. For the refinement of structural and microstructural disorder parameters of polycrystalline materials, Rietveld method is combined with the Fourier analysis for broader peaks. Caglioti Paoletti and Ricci formula [94] are replaced by crystallite size, shape and root mean square regarded as fitting parameters [95].

The diffractogram depends on: phases (crystal structure, phase quantity, cell volume, microstructure etc.), instrument geometry characteristics (Lorentz-polarization, background, beam intensity, resolution, aberrations, radiation etc.) and sample (position, shape, orientation and dimensions). All of these quantities can be written in terms of parameters that can be refined. Residual function is minimized by using the non-linear square algorithm which refines the crystal structure [96]:

$$WSS = \sum_i w_i (I_i^{exp} - I_i^{calc})^2 \quad (4.6)$$

where $w_i = \frac{1}{I_i^{exp}}$, I_i^{exp} and I_i^{calc} are the experimental and calculated intensities in powder diffractometer.

$$I_i^{calc} = S_F \sum_{j=1}^{Nphases} \frac{f_j}{V_j^2} \sum_{k=1}^{Nphases} L_k |F_{k,j}|^2 S_j(2\theta_i - 2\theta_{k,j}) P_{k,j} A_j + bkg_i \quad (4.7)$$

where P_k is the preferred orientation function, $S(2\theta_i - 2\theta_k)$ is the profile shape function and bkg_i is the background. The detailed description of each parameter is presented below:

1: The background is the polynomial function in 2θ : $bkg(2\theta_i) = \sum_{n=0}^{N_b} a_n (2\theta_i)^n$, where N_b is the polynomial degree and a_n the polynomial coefficients.

2: The scale factor for each phase: $S_j = S_F \frac{f_j}{V_j^2}$, where S_j is the phase scale factor, S_F is the beam intensity, f_j is the phase volume fraction and V_j is the phase cell volume.

3: The Lorentz-polarization factor: L_k depends on instrument, i.e. geometry, detector, beam size, sample position and angle α .

4: The structure factor: $|F_{k,j}|^2 = m_k \left| \sum_{n=1}^N f_n e^{-B_n \frac{\sin^2 \theta}{\lambda^2}} e^{2\pi i(hx_n + ky_n + lz_n)} \right|^2$, where N is the number of atoms, f_n is the atomic scattering factor, B_n is the temperature factor, m_k is the multiplicity of k reflection with h, k, l Miller indices and x_n, y_n, z_n are the coordinates of n^{th} atom.

5: The absorption factor: A_j depends on the thickness of sample.

6: The texture: $P_{k,j} = \frac{1}{m_k} \sum_{n=1}^{m_k} (P_{MD}^2 \cos^2 \alpha_n + \frac{\sin^2 \alpha_n}{P_{MD}})^{-\frac{3}{2}}$, where P_{MD} is the March-Dollase parameter, α_n is the angle between crystallographic plane hkl and preferred orientation vector.

The quality of refinement can be checked by two factors, R_{wp} and R_{exp} . For the good fit, $GofF = \frac{R_{wp}}{R_{exp}}$ cannot be lower than 1. These two factors depend on the following parameters:

$$R_{wp} = \sqrt{\frac{\sum_{i=1}^N [w_i (I_i^{exp} - I_i^{calc})]^2}{\sum_{i=1}^N [w_i I_i^{exp}]^2}} \quad (4.8)$$

$$R_{exp} = \sqrt{\frac{(N - P)}{\sum_{i=1}^N [w_i I_i^{exp}]^2}} \quad (4.9)$$

where N and P are the number of points and parameters [96].

4.7 Indentation test

Indentation test is a useful tool to determine the mechanical properties, i.e. elastic modulus and hardness of a material [97]. The typical indentation load vs displacement curve are presented in Figure 4.8. Load and displacement are measured during the indentation test. The important parameters which are measured from load-displacement curve, are: elastic unloading stiffness ($s = \frac{dP}{dh}$), maximum loading (P_{pmax}) and maximum displacement (h_{max}) as presented in Figure 4.10. To measure the hardness of a material, Oliver-Pharr method is implemented by using Equation 4.10 [98].

$$H = \frac{P_{max}}{Ah_c} \quad (4.10)$$

where A is the contact area of material and tip of the indentation at maximum load and h_c is the contact indentation depth calculated by load-displacement curves. In order to estimate the Young's modulus of a material, there is a relation between reduced modulus (E_r) and Young's modulus (E). Effects of non-rigid indenters on the load displacement behaviour can be effectively accounted by E_r which is given in Equation 4.11 [97].

$$\frac{1}{E_r} = \frac{1 - \nu^2}{E} + \frac{1 - \nu_i^2}{E_i} \quad (4.11)$$

and

$$E_r = \frac{S \sqrt{\pi}}{2 \sqrt{A}} \quad (4.12)$$

where E_i is the Young's modulus of diamond indenter. Moreover, ν and ν_i are Poisson ratios for the material and diamond indenter, respectively.

Oliver and Pharr method used for Young's modulus and hardness are extensions of the method proposed by Doerner and Nix [99],

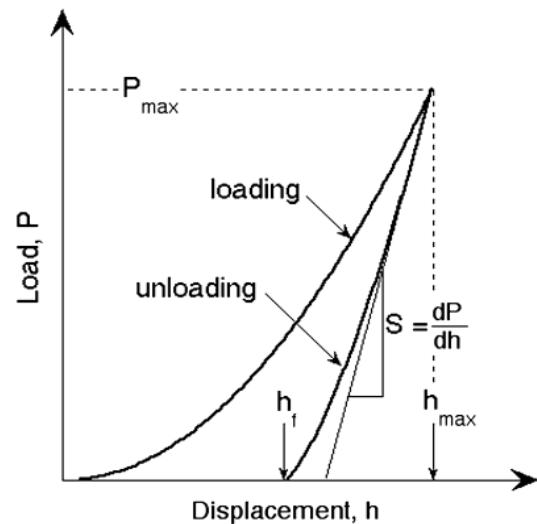


Figure 4.8: Typical indentation load vs displacement curve [97].

where they approximate that the contact area remains constant as the indenter is withdrawn and the resulting unloading curve is linear. However, it is not true experimentally and unloading curves (Equation 4.13) are approximated by the powder law [97].

$$P = \alpha(h - h_f)^m \quad (4.13)$$

where α and m ($1.2 \leq m \leq 1.6$) are power law fitting constants and h_f is the final depth of penetration after the indenter is fully unloaded.

4.8 Characterization of $CaTiO_3$

4.8.1 Differential scanning calorimetry

Sol-gel synthesized and spray dried powder before calcination was studied up to 900 °C in heat flux DSC model 404C Pegasus with corundum crucible. Both, sample and reference holders were mounted in a single furnace. To ensure that the corundum crucibles have minimal influence on the results, the reference crucible was kept empty. The measurements were carried out in Ar atmosphere. Pt/Pt-Rh 10% thermocouples are used to detect thermal signals, which were integrated in the holders below the sample and reference. The sample was heated and cooled with a heating rate of 10 K/m with an intermediate holding time of 5 minutes for signal stabilization.

4.8.2 Scanning electron microscopy and energy dispersive X-ray spectroscopy

The microstructure of $CaTiO_3$ powder as well as conventionally and FAST sintered $CaTiO_3$ samples were analyzed by a field emission SEM (MERLIN[®] VP Compact, Co. Zeiss, Oberkochen). Representative areas of the samples were analyzed by QUANTAX ESPRIT microanalysis software (version 2.0). The samples were mounted on 12 mm SEM-carriers with adhesive conductive carbon tape (Co. PLANO, Wetzlar) and sputter-coated with Au (about 10 nm) under vacuum (EM SCD 004, Co. Leica, Bensheim). SEM-images were taken from the selected regions. The particle size of powder and grain size of densified samples were analyzed and calculated using ImageJ software [100].

EDX spectroscopy was performed on the same machine used for SEM (mentioned above). The experiment was conducted to analyze the elemental composition of sample surfaces. The data was collected over a selected area of sample surface to determine chemical compositions. The EDX detector which was used has a capability to separate the characteristic X-rays of different elements into an energy spectrum and EDX system. The collected data was then used to analyze the energy spectrum in order to determine the abundance of specific elements. All measurements of SEM and EDX were taken with the assistance of Dr. Armin Springer (Elektronenmikroskopisches Zentrum) Universitätmedizin Rostock, Germany.

4.8.3 X-ray photoelectron spectroscopy

XPS was performed to determine the possible defects as well as the chemical composition. The measurements were carried out by Dr. Martin Hantusch using a PHI 5600ci spectrometer at the IFW Dresden, Germany. The source of X-rays was an Al-cathode and after monochromatization, Al- K_α with an energy of 1486.7 eV was selected. Electron gun was used to prevent the charging of sample. To obtain survey and detailed spectra, an analyzer with 20 eV pass energy and 0.05 eV step width as well as 5.85 eV pass energy and 0.05 eV step width were used, respectively. Before the measurement, samples were kept in floodgate in vacuum ($\approx 10^{-7}$ mbar) for approximately two hours to clear the surface from organic components [101]. The experimental setup is presented in Figure 4.9.

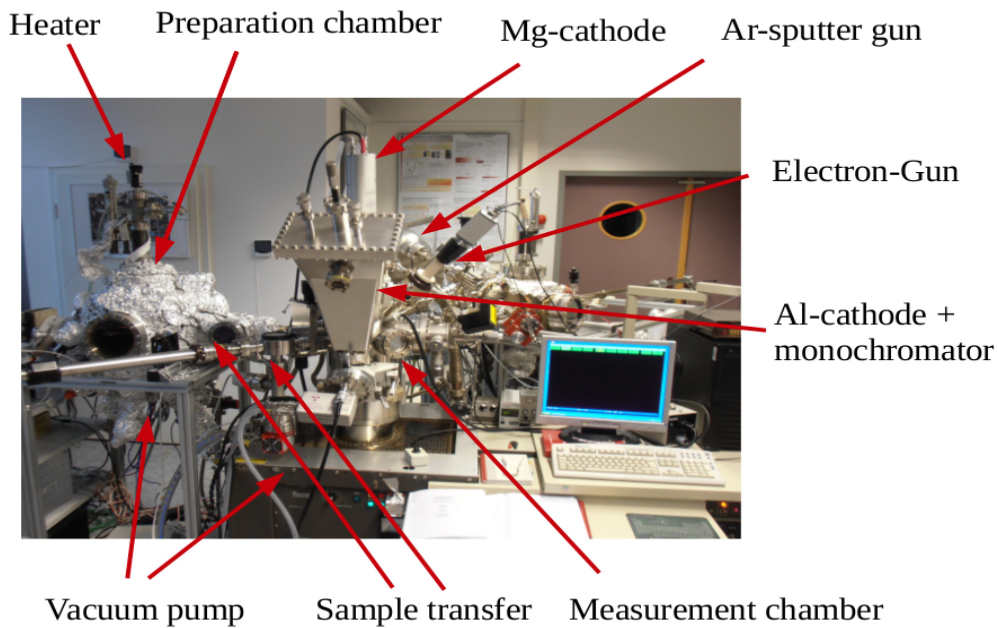


Figure 4.9: Photograph of XPS setup in IFW Dresden, Germany [73].

In order to determine the chemical composition of elements, Equation 4.14 is used [73]. The peak areas A_i used in the following equation are 2p-orbital for calcium and titanium. Moreover, they are 1s-orbital for oxygen and impurities.

$$at\%_i = \frac{A_i \cdot \sigma_i^{-1}}{\sum_j A_j \cdot \sigma_j^{-1}} \quad (4.14)$$

where $at\%_i$ is the atomic weight ratio of an element and σ is the cross-section of analyzed orbit [73].

To determine the chemical composition, survey measurement mode was used by the calculation of atomic ratios between different species through calculating the peak area ratios. The sensitivity factors used in Equation 4.14 for the calculation of chemical compositions are $\sigma_{Ca} = 1.634$, for Ca-2p, $\sigma_{Ti} = 1.798$ for Ti-2p, $\sigma_O = 0.711$ for O-1s, $\sigma_C = 0.296$ for C-1s and $\sigma_N = 0.477$ for N-1s [88]. The analysis about the defect dynamics are explained in Chapter 5.

Furthermore, an additional measurement was performed by using XPS setup which is

a depth profile measurement. The presence of each element in the sample with depth of approximately 100 nm was estimated. Non-monochromatized X-rays from Mg K_α source was used with measurement angle of 55° . Argon sputtering with a pressure of 3×10^{-7} mbar and flux of $30 \mu\text{A}$ resulted in approximately 3.5 nm depth per minute sputtering.

4.8.4 Piezoelectric measurement

Piezoelectric measurements of both direct and inverse piezoelectric effects were carried out for the conventionally and FAST sintered samples. Moreover, poling treatment was also performed in FAST sintered $CaTiO_3$ using inverse piezoelectric setup.

The direct piezoelectric measurement was performed using dynamic method. The setup was a modification of the one from Fukada and Yusuda [5]. The schematic diagram of the modified setup is presented in Figure 4.10. An alternating voltage of 10 V generated by a RIGOL DG4062 function generator was applied to the piezo-actuator. Moreover, a frequency of 10 Hz was selected. Consequently, the oscillating force was transmitted to the sample. When a piezoelectric material is used as a sample, an alternating voltage was produced due to the direct piezoelectric effect. This produced alternating voltage was collected using MMF M68D1 charge amplifier. The measurements were recorded with the help of PicoScope 6 (pico technology) which was attached to charge amplifier. Initially, a non-piezoelectric material (NPM) was clamped inside the metal frame between the screw and commercial piezo-actuator (type PICMA P-888.31 produced by PI ceramics) to perform the measurement. NPM was used as a reference material to determine the maximum noise of the setup. Afterwards, conventionally and FAST sintered $CaTiO_3$ were used. It is worth mentioning that the samples were isolated using corundum which was fixed with a screw and a piezo-actuator.

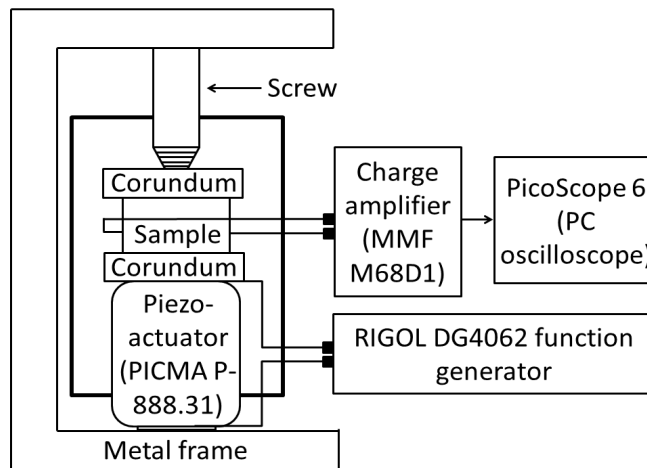


Figure 4.10: Schematic diagram of direct piezoelectric setup for dynamic measurement.

The inverse piezoelectric effect was investigated using FT analyzer 2000 E of aix-ACCT systems GmbH at Aachen, Germany. The sample holder was connected with FT analyser 2000 E and high voltage trek amplifier to apply strong EEF to the sample. Triangular voltage excitation signals were used to carry out the measurements. Displacements of samples due to inverse piezoelectric effect were determined using double

beam laser interferometer (aixDBLI) which was also connected with the sample holder. It is important to mention that aixDBLI allows to measure the thickness changes of thin films under EEF excitation with an accuracy of 0.2 pm/V [102]. This allows to measure very precise strain produced in a material due to EEF. Data of displacement and current density (J)-EEF characteristic curves was traced by aixPlover software (aixACCT systems GmbH). The values of d_{33+} and d_{33-} were computed by linear regression slope of displacement versus positive and negative EEF, respectively. Eventually, the average d_{33} value was calculated from d_{33+} and d_{33-} values. The image of inverse piezoelectric setup is shown in Figure 4.11.

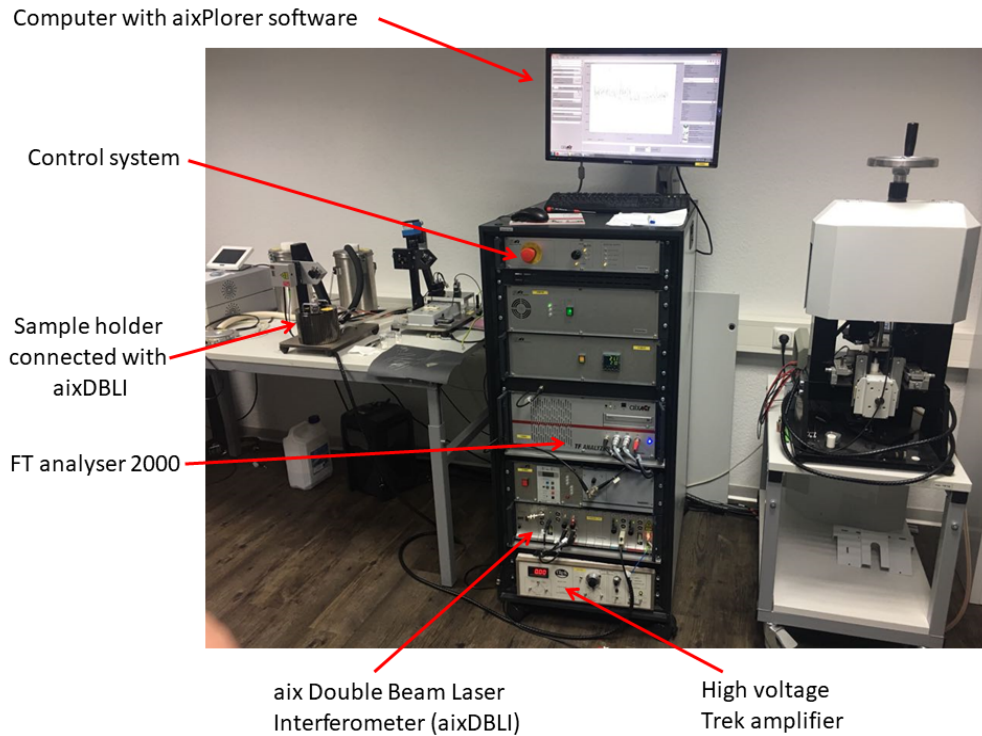


Figure 4.11: Photograph during the measurement of inverse piezoelectric effect of $CaTiO_3$ by static method in aixACCT systems GmbH, Aachen.

4.8.5 High energy X-ray diffraction

HEXRD was carried out at the high energy material science beamline P07 located at high brilliance synchrotron radiation storage ring PETRA III, DESY, Hamburg. The storage ring parameters are: energy of 6 GeV and current of 100 mA. A two meter long standard PETRA undulator was the source of X-rays. An indirectly water cooled single bounce monochromator with a Si(220) Laue crystal was used to select the radiation with a wavelength of $\lambda = 0.1424 \text{ \AA}$ [103], [104]. The experiments were performed in transmission Debye-Scherrer geometry. The diffraction patterns were collected with a 2D-area PerkinElmer detector. The experimental setup is shown in Figure 4.12. The green dashes were drawn to show the path of X-ray beam.

Firstly, HEXRD was performed on calcinated $CaTiO_3$ powder, conventionally and FAST sintered $CaTiO_3$ in order to examine the single shot diffraction patterns. Secondly, in-situ diffraction patterns were measured for FAST sintered $CaTiO_3$ which are

described in next Section. The sample to detector distances were 1230 mm and 1220 mm for single shot virgin samples and in-situ diffraction, respectively. It is also important to mention that all measurements were performed in air and at room temperature. The experiment was performed together with Dr. Kerstin Witte and Dr. Wiktor Bodnar (Physics of New Materials, University of Rostock).

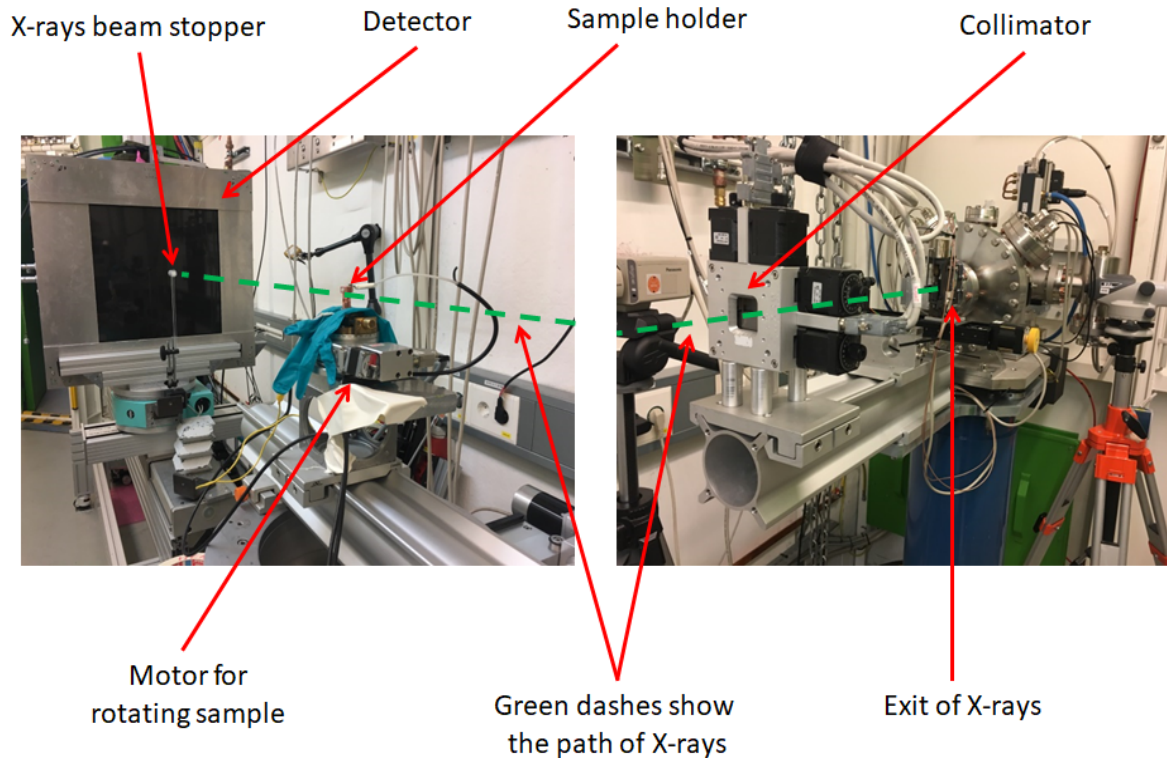


Figure 4.12: Photograph of HEXRD setup in HEMS beamline P07, DESY, Hamburg, Germany.

In-situ diffraction experiment

In the in-situ diffraction measurements, FAST sintered $CaTiO_3$ was mounted between copper electrodes and direct current (DC)-electric circuit was connected to these electrodes. In the start, diffraction pattern was recorded (without applying EEF) when SF was perpendicular to incident X-ray beam as shown in Figure 4.13a. Then, the sample was rotated horizontally by 90° and another diffraction pattern was recorded when SF was parallel to incident X-ray beam as shown in Figure 4.13b. Afterwards, EEF of 6.5 kV/cm was applied to the sample and diffraction pattern was measured when incident X-ray beam was in perpendicular and then parallel direction to EEF. Subsequently, EEF was increased to 13 kV/cm and again diffraction pattern was measured in both directions (perpendicular and parallel). EEF was then reduced to 6.5 kV/cm and afterwards to 0 kV/cm and diffraction patterns were also recorded again for both EEF values. In the same way, negative EEF was applied to the sample, i.e. -6.5 kV/cm, -13 kV/cm, -6.5 kV/cm and finally again to 0 kV/cm. At every point of EEF, diffraction pattern was measured subsequently in both perpendicular and parallel directions of EEF to incident X-ray beam. In this way, a complete cycle of EEF was applied to the sample as shown in Figure 4.14a. In total, nine diffraction patterns were

collected for each direction. All EEF values were held for the adequate time to acquire diffraction pattern in both directions (approximately 3 minutes).

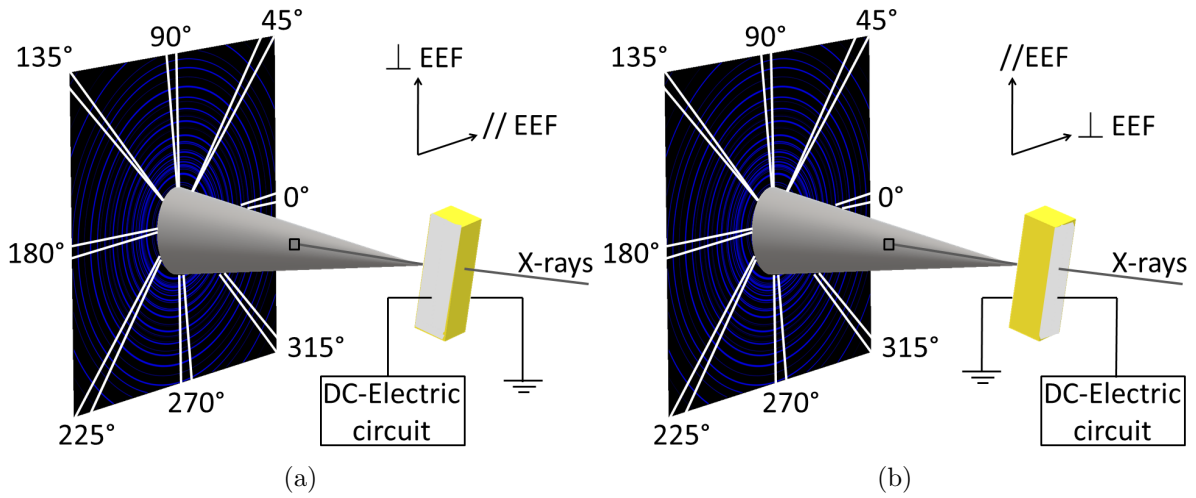


Figure 4.13: Schematic diagram of in-situ HEXRD experimental setup with DC-electric circuit and incident X-ray beam in (a) perpendicular and (b) parallel to EEF/SF direction.

During all EEF values measurement, resistance of the sample was also measured simultaneously through DC-electric circuit. The DC-electric circuit diagram is shown in Figure 4.14b. The resistance of sample (R_s) was measured indirectly via a reference resistance (R_R) and was calculated by Equation 4.15 [101]:

$$R_s = R_R \frac{U_0 - U_R}{U_R} \quad (4.15)$$

where U_0 is the applied voltage and U_r is the voltage across reference resistance.

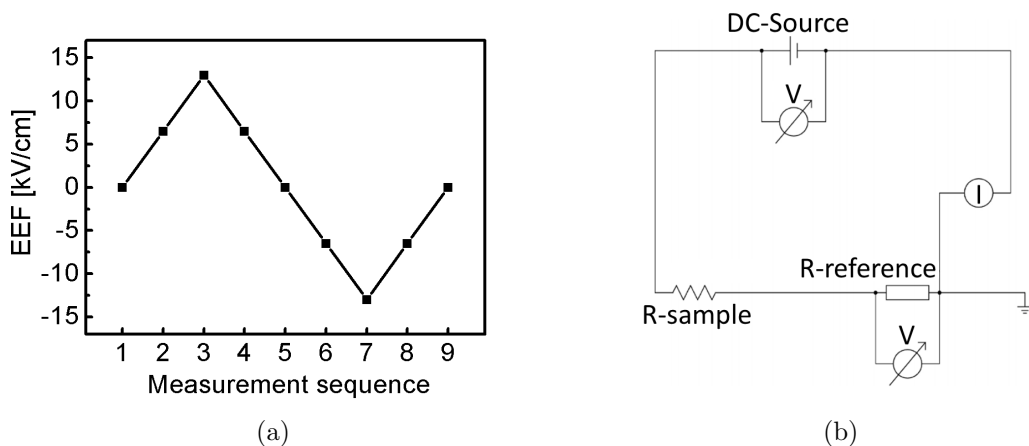


Figure 4.14: (a) Cycle of high voltage (EEF) measurement and (b) DC-electric circuit diagram [101] used for in-situ HEXRD experiment.

Assuming that the contact resistance between the sample and silver electrodes is negligible as compared to the intrinsic resistance of sample, the resistivity (ρ) of sample was

measured using Equation 4.15 derived from Equation 4.16.

$$\rho = R_s \frac{A}{l} \quad (4.16)$$

where A is the area of an electrode and l is the thickness of the sample [101].

Analysis and data reduction

Rietveld method is used with the help of material analysis using diffraction (MAUD) program [105], [106]. MAUD program allows to reduce 2D images into 1D patterns in intensity versus 2θ . The 2D images collected from single shot experiments of calcinated $CaTiO_3$ powder, virgin conventionally and FAST sintered samples were integrated (complete Debye-Scheere rings) in 5° steps. However, in-situ measurements were integrated after every 45° step in the azimuthal direction starting from 0° to 5° azimuthal sector up to 315° to 320° azimuthal sector. In this way, for a single measurement, 8 integrated diffraction patterns were created. Where, each azimuthal sector corresponds to a certain diffraction pattern. These azimuthal sectors were integrated with 1° steps. The azimuthal sectors are represented in the following way:

0° to 5° - 0°
 45° to 50° - 45°
 90° to 95° - 90°
 135° to 140° - 135°
 180° to 185° - 180°
 225° to 230° - 225°
 270° to 275° - 270°
 315° to 320° - 315°

The detailed illustration of azimuthal sectors is shown in appendix Figure A.1. Additionally, the diffraction patterns of each azimuthal sector, resulted from one measurement, are shown in appendix Figure A.2. It is important to mention that when incident X-ray beam is perpendicular to EEF direction, 0° or 180° and 90° or 270° azimuthal sectors are parallel and perpendicular to EEF direction, respectively, as shown in Figure 4.13a. However, the directions reversed when incident X-ray beam is parallel to EEF direction as shown in Figure 4.13b.

From data reduction, all integrated azimuthal sectors were separately analyzed by Rietveld refinement [92]. Moreover, to obtain reasonable atomic positions, phases weight percentage, crystallite sizes or lattice parameters, the initial states of sample in every measurement were refined in the beginning. During all types of refinement except texture analysis, arbitrary texture model and delft line broadening model were used. However, during the refinement of texture analysis, the orientation distribution function (ODF) was determined by using E-WIMV texture model and the parameter to generate symmetry was opted for as none. It is important to mention that for all data refinements, the number of iterations were kept equal in order to avoid misleading refinement results.

Visualization of electronic and structural analysis

To visualize the crystal structure of $CaTiO_3$ samples and calculation of their dimensions, visualization of electronic and structural analysis (VESTA) program [41] is used. Theoretically calculated Rietveld parameters, which include unit cell and atomic position parameters, were extracted by refinement of HEXRD data. These parameters were then used for plotting to visualize unit cell in 3D.

4.8.6 Nanoindentation test

Nanoindentation tests were performed with the assistance of Dr. Wiktor Bodnar (Physics of New Materials, University of Rostock) using a nanoindentation CETR UMT multi-specimen test system with a sharp Berkovich indenter tip. At least 7 points were chosen for each indentation load to get better statistic values. Young's modulus and hardness of (polished) conventionally and FAST sintered $CaTiO_3$ were measured by Oliver and Pharr method using Equation 4.13, which was implemented in the UMT software.

Chapter 5

Results

In this chapter, results of calcinated powder as well as conventionally and FAST sintered samples are presented. In the frame of this work, the main focus will be on finding the causes of highly localized defects (oxygen vacancies) as well as the trapping sites in bulk samples. Additionally, reasons of piezoelectric behaviour of FAST sintered sample and their comparison with conventionally sintered sample will be presented. To study the influence of the lattice strain, structural changes due to distortions will also be discussed.

5.1 Phase analysis - DSC

DSC was performed to observe the phase transition (amorphous to crystalline phase), since sol-gel prepared powder was completely amorphous. Figure 5.1a shows DSC curve of powder (without oven drying). First small endothermic peak between $75\text{ }^{\circ}\text{C}$ to $160\text{ }^{\circ}\text{C}$ (first arrow) is caused by the elimination of ethanol and water. Next, the first sharp exothermic peak (second arrow) results from the thermal decomposition of organic substances which caused enormous loss of mass [107]. Following this sharp exothermic peak, second endothermic peak (third arrow) is the formation of CaTiO_3 orthorhombic (pbnm) phase with onset temperature of $(495 \pm 10)\text{ }^{\circ}\text{C}$. The temperature of this phase formation is much lower than the required temperature in conventional ceramic route [108]. This lowering of temperature allows the formation of powder with controlled nanoparticle sizes which can positively impact on the properties of material. The total mass loss during the whole process (Figure 5.1a) was mainly caused, approximately 85%, by first sharp exothermic peak. Hence, sol-gel prepared powder was dried at $180\text{ }^{\circ}\text{C}$ in oven as described in Chapter 3.

DSC curve of oven dried powder is presented in Figure 5.1b. In first run, small endothermic signal between $100\text{ }^{\circ}\text{C}$ to $180\text{ }^{\circ}\text{C}$ (first two arrows) is caused by elimination of ethanol and water, respectively. The exothermic peak with onset temperature of $(345 \pm 5)\text{ }^{\circ}\text{C}$ (third arrow) occurs due to the phase transformation from amorphous to titanium dioxide phase [107]. Following the exothermic peak, second sharp endothermic peak with onset temperature of $(495 \pm 10)\text{ }^{\circ}\text{C}$ (fourth arrow) shows the formation of CaTiO_3 orthorhombic (pbnm) phase. Total mass loss during the whole process of first run (Figure 5.1b) was approximately 33.6%. In the second run, there is no peak due to previous orthorhombic CaTiO_3 phase formation in first run as shown in Figure 5.1b. It is important to mention that the reason for the selection of calcination temperature

of $650\text{ }^{\circ}\text{C}$ (discussed in Chapter 3) was to be sure about the complete phase formation of CaTiO_3 . Since, the complete end of the phase formation peak of CaTiO_3 was at $(595 \pm 8)\text{ }^{\circ}\text{C}$ which can be seen in Figure 5.1b.

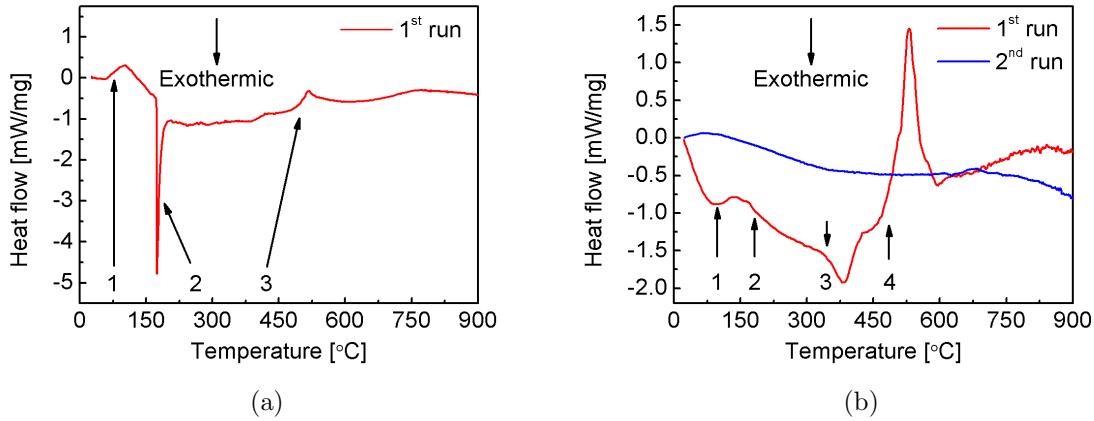


Figure 5.1: DSC curves of sol-gel synthesized powder (a) before and (b) after oven drying.

5.2 Structure analysis - HEXRD

Samples	d [nm]	Phases [wt%]			
		CaTiO_3	$\alpha\text{-TiO}_2$	$\gamma\text{-TiO}_2$	CaO
Calcinated powder	98 ± 3	83.8 ± 0.5	4.2 ± 0.3	6.7 ± 0.4	5.4 ± 0.6
Conventionally sintered	406 ± 4	94.6 ± 0.3	5.4 ± 0.1	-	-
FAST sintered	200 ± 1	94.4 ± 0.2	5.6 ± 0.6	-	-

Table 5.1: Crystallite sizes and phases weight fractions of calcinated powder, conventionally and FAST sintered CaTiO_3 derived by single shot HEXRD experiments.

The experimental, fitted and differential patterns of calcinated CaTiO_3 as well as conventionally and FAST sintered samples measured by single shot HEXRD experiments are presented in Figures 5.2a and 5.2b, respectively. The corresponding Bragg positions of all contributed phases are also shown. Additionally, after the magnification of diffraction pattern of calcinated powder in Figure 5.2c and FAST sintered CaTiO_3 in Figure 5.2d, the peaks are showing a clear view of Bragg positions. In all patterns, orthorhombic (pbnm) phase of CaTiO_3 was present, but the crystallite sizes (d) of the CaTiO_3 were increased significantly from calcinated powder $d = (98 \pm 3)\text{ nm}$ to FAST sintered $d = (200 \pm 1)\text{ nm}$ due to recrystallization process during sintering [26]. The conventionally sintered sample showed significantly larger crystallite size $d = (406 \pm 4)\text{ nm}$ compared to FAST sintered sample as a result of the longer sintering time. Small amounts of other phases, such as brookite ($\gamma\text{-TiO}_2$), rutile ($\alpha\text{-TiO}_2$) and calcium oxide (CaO), were found in calcinated powder. However, after conventional and FAST sintering, only $\alpha\text{-TiO}_2$ phase was present. This indicates that TiO_2 and CaO form

CaTiO_3 phase upon the sintering process. It is also possible that excess amount of $\gamma\text{-TiO}_2$ transformed into $\alpha\text{-TiO}_2$, as $\alpha\text{-TiO}_2$ is more stable and $\gamma\text{-TiO}_2$ prefers to be transformed to $\alpha\text{-TiO}_2$ when heated [109]. The crystallite sizes and weight fractions of the corresponding phases are presented in Table 5.1. The lattice parameters extracted from Rietveld refinement as well as R_{wp} and R_{exp} values [92] are also shown in appendix Table A.1.

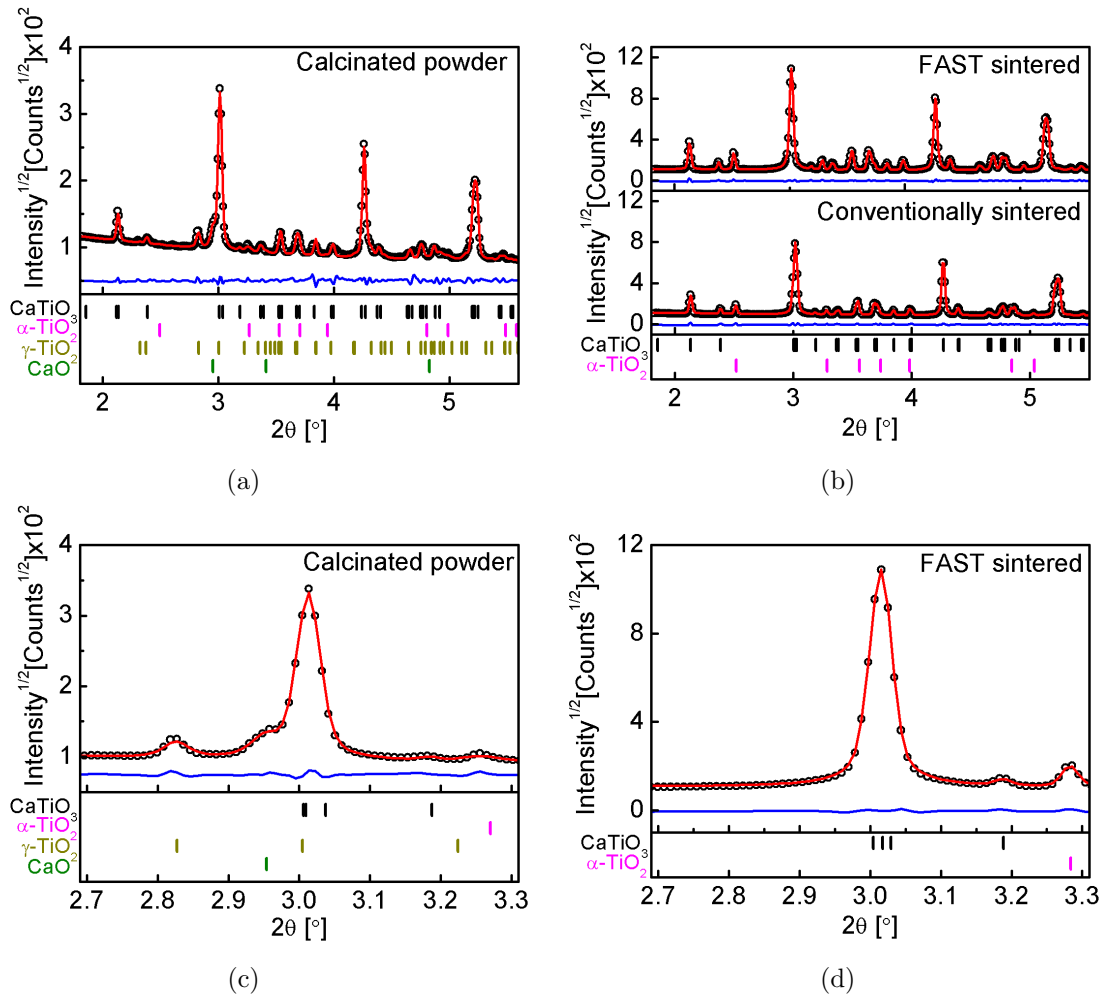


Figure 5.2: HEXRD patterns of (a) calcinated powder, (b) conventional and FAST sintered CaTiO_3 as well as magnification of (c) calcinated powder and (b) FAST sintered CaTiO_3 . Dots - experimental pattern, red line - fitted pattern, black line - differential pattern. Additionally, corresponding Bragg positions of all contributed phases are shown.

5.3 Surface morphology - SEM

Exemplary SEM images of calcinated powder, conventionally and FAST sintered CaTiO_3 with the particle and grain size distribution are presented in Figure 5.3. ImageJ software [110] was used for the determination of particle and grain sizes. The average

particle as well as grain sizes were estimated assuming a log normal distribution represented by solid blue line in the graph. In Figure 5.3a, it can be seen that most of

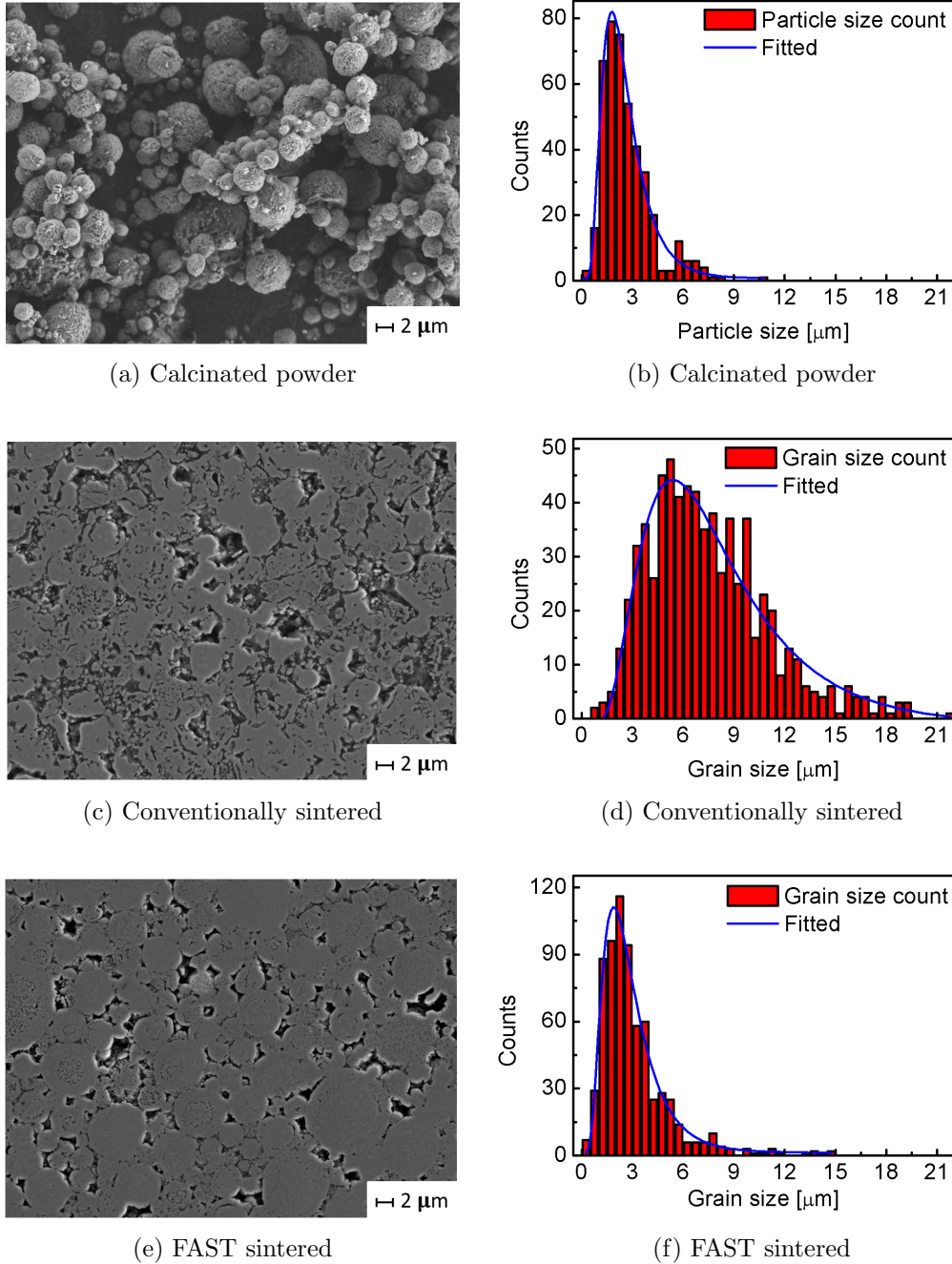


Figure 5.3: Exemplary SEM images of (a) calcinated powder (c) conventionally and (e) FAST sintered samples as well as their corresponding particle and grain size distribution of (b) calcinated powder (d) conventionally and (f) FAST sintered samples. Additionally, a log normal distribution was fitted to determine the average value.

the particles are spherical in shape. These particle size distributions are presented in Figure 5.3b which are in range of $\sim 0.5 \mu\text{m}$ to $\sim 8.5 \mu\text{m}$ and average particle size of $(2.3 \pm 0.1) \mu\text{m}$. Figures 5.3c and 5.3e show the polished surfaces of conventionally

and FAST sintered $CaTiO_3$ along with their grain size distributions shown in Figures 5.3d and 5.3f, respectively. The grain shape of the FAST sintered sample is spherical with grain size range of $\sim 0.5 \mu m$ to $\sim 9 \mu m$ and average grain size of $(2.5 \pm 0.1) \mu m$. However, conventionally sintered sample has ambiguous grain shape with broad range of grain size $\sim 1 \mu m$ to $\sim 19 \mu m$ and average of $(7.2 \pm 0.3) \mu m$. This is probably due to abnormal Ostwald ripening which also causes irregular elongation of grains [26]. As $CaTiO_3$ ceramic is brittle [111], it is possible that a part of the grains broke into small pieces and settled down into pores during the polishing process. These pores can be observed in images as dark areas between the brighter grains.

It is suggested that the process of grain growth can be divided into two parts: the initial sintering stage when density is less than 90% and the later stage when density is greater than 90%. The major grain growth happens in later part of sintering due to the reason that pores in the later stage are almost closed and the effect of open pores on pinning of grain boundaries decreased as compared to initial stage sintering [26], [112]. This means that grain boundary migration is the dominant process for grain growth. In contrast, experimental results also show that the grain growth occurs significantly even in the initial stage of sintering due to coarsening [112]. Additionally, in general the average grain size of a sample increases with increasing sintering temperature and time of sintering [26]. This trend is observed in conventionally sintered $CaTiO_3$ with the abnormally increased grain size. However, grain size is suppressed in FAST sintered $CaTiO_3$. The reasons are low heating rate (7 K/m) and increased holding time (4 h) at elevated temperature during conventional sintering. As a result, relatively large average grain size is produced in conventional sintering sample due to coarsening at the initial stage which continues to elevated temperature. On the contrary, the average grain size of FAST sintered $CaTiO_3$ is almost same as the particle size of calcinated powder because of high heating rate (100 K/m) and less holding time (5 min) at elevated temperature. Hence, controlled grain size of FAST sintered $CaTiO_3$ was produced with relatively increased grain boundary areas (discussed in Chapter 6). The exemplary SEM images of conventionally and FAST sintered samples with low magnification are also presented in Appendix Figure B.1.

5.4 Chemical composition - EDX

The EDX spectroscopy is used to determine the chemical composition of the samples. To collect information about deeper atomic layers, calcinated powder was cold pressed before EDX measurement. The Figure B.2 in appendix shows the presence of calcium, titanium, oxygen and carbon atoms. No other elements were detected. The atomic ratios are estimated by EDX spectroscopy of elements in samples and are presented in Table 5.2. It can be seen that very small amount of carbon is present in the samples, especially FAST sintered $CaTiO_3$. This suggests that there is no significant diffusion of carbon from graphite foil to sample. It is possible that the carbon atoms detected in samples are organic substances adsorbed on the surfaces of samples due to the contact with air. These results prove that FAST sintering conditions prevent the diffusion of carbon. This diffusion should be avoided, otherwise there might be a significant change in conductivity.

It is worth mentioning that the difference between K_α line of carbon and L_α line of calcium is not sufficient for quantification. In the same way, the difference between K_α

Element	Atom [%]		
	Calcinated powder	Conventionally sintered	FAST sintered
Oxygen	56.4±4.6	58.6±5.1	54.3±4.2
Calcium	18.4±1.1	17.1±1.1	19.8±1.1
Titanium	17.3±1.3	17.4±1.4	20.2±1.4
Carbon	7.9±0.6	6.9±0.6	5.7±0.4

Table 5.2: Atomic percent with absolute error of elements in calcinated powder, conventionally and FAST sintered $CaTiO_3$ determined by EDX spectroscopy.

line of oxygen and L_α line of titanium is not sufficient. This is because the resolution of EDX spectroscopy detector is 0.126 keV and the difference between these characteristic lines is smaller than the resolution of detector. The quantification of carbon is done by integrating only over the K_α line but there is an overlapping of K_α carbon and L_α calcium. Similarly, quantification of oxygen is done by integrating only over the K_α line but there is an overlapping of K_α oxygen and L_α titanium. Therefore, the fraction of carbon and oxygen may be slightly overestimated. Regardless of overestimation, it can be seen in appendix Figure B.2a, B.2c and B.2e that an increase in counts per second (cps) of oxygen atoms is observed after conventional sintering. Whereas, cps of oxygen is decreased after FAST sintering of calcinated powder. Although these values are in the error range (Table 5.2), still there is a trend of increase in oxygen atomic percent in conventionally sintered sample and decrease in FAST sintered one. This indicates that even if the oxygen vacancies (defects) were present in calcinated powder, they healed during conventional sintering. This healing occurred due to oxygen environment as well as longer sintering time which provided enough time for the elimination of oxygen vacancies. This led to the increase in oxygen atomic percent. However, FAST sintering in vacuum environment and shorter sintering time increased the amount of oxygen vacancies causing the decrease of oxygen atomic percent.

5.5 XPS spectra

Firstly, the chemical composition of calcinated powder and FAST sintered $CaTiO_3$ is determined to investigate any additional element in the material. Secondly, the defects close to surfaces are analyzed by measuring detailed spectra of Ca-2p, Ti-2p and O-1s peaks. The peaks were fitted by using CasaXPS [113] and fityk [114] software for survey measurement and defect analysis, respectively. Moreover, to observe the depth profiles (100 nm) of elements, gnuplot is used [115].

5.5.1 Chemical composition

The survey measurements of calcinated powder and FAST sintered $CaTiO_3$ with identified peaks are presented in Figure 5.4. In calcinated powder, only calcium, titanium and oxygen with small amount of carbon is detected. However in FAST sintered sample, the additional peak of nitrogen is also observed. There is a possibility that during FAST sintering at high temperature and pressure, some of the oxygen vacancies are immediately replaced by nitrogen. These types of nitrogen substitutions are commonly

observed in the case of transition metal oxides [116]. The chemical compositions determined by survey measurements (Figure 5.4) of calcinated powder and FAST sintered $CaTiO_3$ are presented in Table 5.3. The FAST sintered $CaTiO_3$ contains high amount

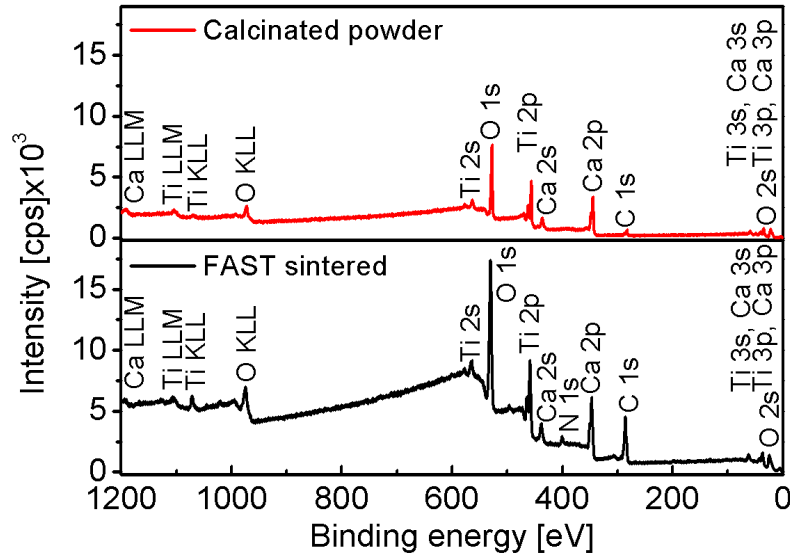


Figure 5.4: Survey measurements of calcinated powder and FAST sintered $CaTiO_3$.

of carbon which is most likely to diffuse during sintering. However, the reason of high amount of carbon species detected as compared to the results of EDX in FAST sintered $CaTiO_3$ is not clear. There is a possibility that carbon species were overestimated in XPS during survey measurement. To determine this and estimate the diffusion of carbon, depth profiles of elements were measured, which are presented in appendix Figure B.3. It can be seen in appendix Figures B.3b, B.3a and B.3c that calcium, titanium and oxygen are detected till maximum observed depth but carbon is only present on the surface (appendix Figure B.3d) and detected till the depth of 14 nm. This indicates that carbon was not diffused completely in a material during FAST sintering and is present only on the surface. Apart from the FAST sintering, there is a possibility that carbon species are adsorbed due to exposing sample in air and its storage in air filled boxes. However, the amount of carbon from Table 5.2 shows that only small amount of carbon is present as compared to XPS data. This suggests that there is no significant diffusion of carbon which is consistent with the XPS depth profile.

Element	Calcinated powder		FAST sintered	
	Atom [%]	[%] StDev	Atom [%]	[%] StDev
Oxygen	57.1	0.5	46.1	0.3
Calcium	16.0	0.2	9.1	0.1
Titanium	16.9	0.3	10.7	0.1
Carbon	10.0	0.5	31.3	0.3
Nitrogen	-	-	2.8	0.3

Table 5.3: Atomic percent of elements with standard deviation (StDev) of calcinated powder and FAST sintered $CaTiO_3$ determined by XPS.

5.5.2 Defect analysis

Lattice point defects close to surface are examined by measuring detailed spectra of Ti-2p, Ca-2p and O-1s peaks of powder and FAST sintered $CaTiO_3$. It was noticed that the spectral peaks of FAST sintered $CaTiO_3$ are broadened as compared to the spectral peaks of calcinated powder. Moreover, the doublet separation of Ti-2p in FAST

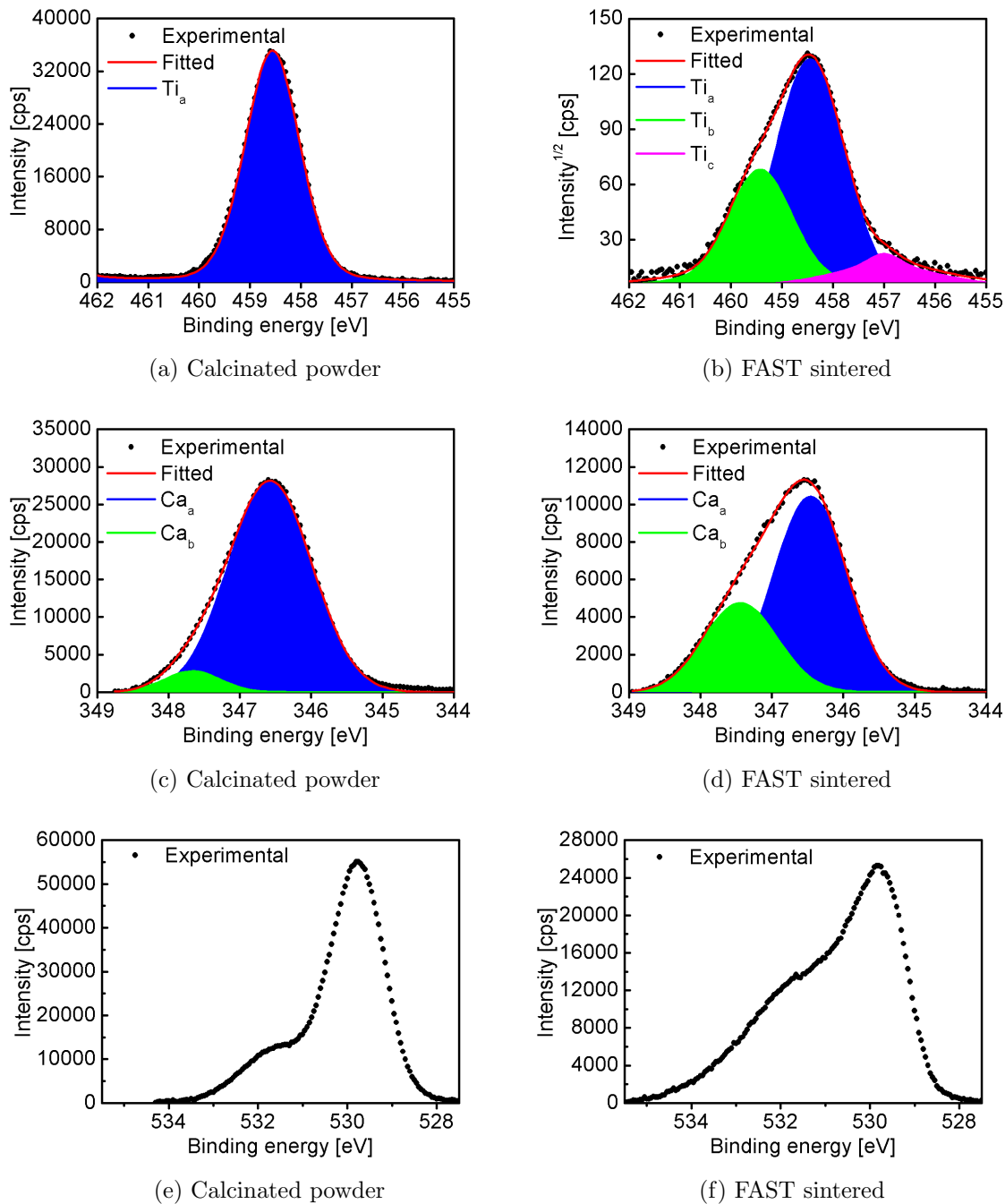


Figure 5.5: XPS detailed spectra of (a) $Ti - 2p_{3/2}$, (c) $Ca - 2p_{3/2}$, (e) $O - 1s$ peaks of calcinated powder and (b) $Ti - 2p_{3/2}$, (d) $Ca - 2p_{3/2}$, (f) $O - 1s$ peaks of FAST sintered $CaTiO_3$ after background subtraction. The experimental (dots), the fitted (red solid line) and sub-fitted peaks are also presented.

sintered $CaTiO_3$ is ($\sim 5.82 \pm 0.02$) eV, which is slightly larger than one of the calcinated powder ($\sim 5.71 \pm 0.02$) eV (see appendix Figure B.4). These facts indicate the splitting of binding energy due to different chemical environments which can be influenced by FAST sintering [117], [118]. Hence, the data of calcinated powder and FAST sintered $CaTiO_3$ were analyzed by careful fitting. The Shirley background was subtracted for all spectra before Pseudo-Voigt line shape fitting [114].

The defect analysis is performed on $Ti - 2p_{3/2}$, $Ca - 2p_{3/2}$ and $O - 1s$ peaks of detailed spectra of calcinated powder and FAST sintered $CaTiO_3$. Figure 5.5a and 5.5c present the spectra of Ti and Ca species in calcinated powder, respectively. Similarly, Figures 5.5b and 5.5d show the spectra of Ti and Ca species for the FAST sintered sample. All spectra are plotted with normal intensity values except in Figure 5.5b, which is plotted in square root scale to achieve same statistical derivation on the maxima and the background [119]. The fraction of species are calculated by using Equation 5.1.

$$S_i(\%) = 100\left(\frac{A_i}{\sum A_i}\right) \quad i \in a, b, c \quad (5.1)$$

where S_i is the fraction of a particular specie and A_i is the area under the curve of specie determined by fitting of spectral peaks.

It is a well known fact that the change in electron density or chemical environment around examined atom is drastically influenced by the surrounding atoms, which results in the shift or splitting of binding energy. This might be the direct charge like oxidation state or it is also possible in electric dipoles because electric dipoles are the charge distribution [120]–[124]. It is also reported that an atom can have more than one splitting of binding energies caused by lattice distortions as it also changes the chemical bonding between the atoms [125]. Hence, distortion in the atom is caused by off centered Ti atom which can have different charge environment with significant difference in binding energies that can be detected by XPS.

Figure 5.5a shows only one type of TiO_6 octahedral specie, i.e. Ti_a , which is observed in $Ti - 2p_{3/2}$ peak of calcinated powder. However, three different types, i.e. Ti_a , Ti_b and Ti_c species are observed in FAST sintered $CaTiO_3$ (Figure 5.5b). Ti_a specie can correspond to non-distorted (normal) structure of TiO_6 octahedral (bound with $CaTiO_3$ as well as TiO_2 impurity). Whereas, Ti_b is a newly formed specie detected in bulk $CaTiO_3$ after FAST sintering and can be related to a distorted structure of the TiO_6 octahedra. Additionally, a small amount of reduced Ti_c specie (TiO_5 octahedra) is located in the low energy shoulder of the $Ti - 2p_{3/2}$ peak. This is caused by the oxygen vacancies produced by FAST sintering in vacuum [26] leading to a shift of binding energy of $Ti - 2p_{3/2}$ peak, when Ti^{+4} is reduced to Ti^{+3} . It is also possible that the nitrogen atom is replaced with oxygen atom in the lattice due to doping [126].

In Figure 5.5c and 5.5d, two different types of calcium species, i.e. Ca_a and Ca_b , can be identified. It is most probable that Ca_a specie in both samples is bound to Ti_a and Ca_b specie to Ti_b specie in FAST sintered sample. Their quantities are comparable to one another, so it is suggested that these species are bound together (Table 5.4). However, Ca_b specie in calcinated powder appears probably due to the impurity of CaO in calcinated powder which is also detected in HEXRD pattern [88].

Figures 5.5e and 5.5f show O-1s peaks of calcinated powder and FAST sintered $CaTiO_3$, respectively. The O-1s peaks of both samples are not fitted. The reason is that a large number of different oxygen species are possible: non-structural oxygen

Species	Calcinated powder			FAST sintered		
	BE_{center} [eV]	fwhm [eV]	%	BE_{center} [eV]	fwhm [eV]	%
Ti _a	458.5 ± 0.2	1.26 ± 0.02	100.00	458.4 ± 0.2	1.13 ± 0.03	75.06
Ti _b	-	-	-	459.4 ± 0.2	1.10 ± 0.01	21.42
Ti _c	-	-	-	457.0 ± 0.1	1.10 ± 0.02	3.52
Ca _a	346.6 ± 0.2	1.38 ± 0.03	90.66	346.5 ± 0.2	1.30 ± 0.02	71.77
Ca _b	347.5 ± 0.3	1.33 ± 0.02	9.34	347.6 ± 0.1	1.30 ± 0.01	28.23

Table 5.4: The binding energy of peak center, fwhm and fraction of the specie (%) of $Ti - 2p_{3/2}$ and $Ca - 2p_{3/2}$ in calcinated powder and FAST sintered $CaTiO_3$ determined by XPS.

as O-O, C-O or O-H, distorted structural oxygen, non-distorted structural oxygen or oxygen bound to TiO_2 as well as bound to $CaTiO_3$. Therefore, it is a challenge to fit O-1s peak because it can satisfy any fitting procedure due to the possibility of large number of species. Nevertheless, it can be seen that O-1s peak of FAST sintered sample is relatively broader as compared to calcinated powder. This observation indicates that newly oxygen species could be formed after FAST sintering due to lattice distortion. To summarize, the results indicate that there are two different types of crystal structures present in FAST sintered $CaTiO_3$, which were not observed in the calcinated powder. These two types of crystal structures can be interpreted as one with stress (distorted structure) and other without stress (non-distorted structure). The binding energy of peak center (BE_{center}), fwhm and quantities of particular species are presented in Table 5.4. It is also important to mention that a small shift in binding energy of species may happen due to the usage of electron gun during the experiment.

5.6 Piezoelectric response

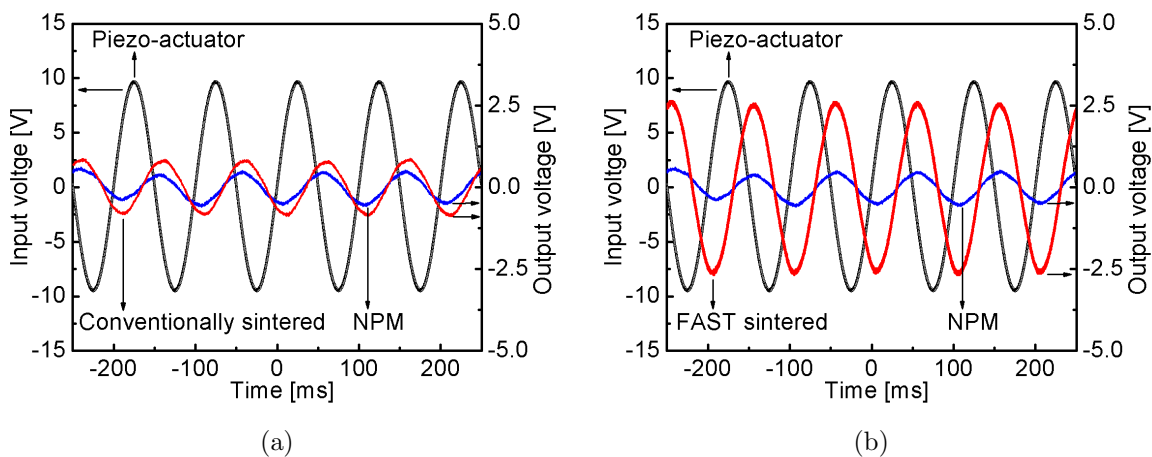


Figure 5.6: Voltage measurements of NPM, (a) conventionally and (b) FAST sintered $CaTiO_3$ measured with the direct piezoelectric effect produced by dynamic method.

Both direct and inverse piezoelectric measurements were carried out for the conventionally and FAST sintered $CaTiO_3$ samples. The results of the direct piezoelectric

measurements are presented in Figure 5.6. The output alternating voltages (red colour) produced by conventionally and FAST sintered $CaTiO_3$ are presented in Figures 5.6a and 5.6b, respectively. All measurements were taken with gain of 1000 mV/pC of charge amplifier. It is important to mention that phase shift of the output voltage is due to the time delay of charge amplifier. The shown alternating input voltage is the voltage applied to the piezo-actuator for its oscillation. It can be seen that small alternating output voltage (blue colour) is produced by NPM (V_{NPM}). This is interpreted as the maximum noise produced by the setup. The conventionally sintered $CaTiO_3$ shows a minor increase in the signal (V_{CaTiO_3}) as compared to the NPM. This could be due to the small amount of charges present on the surface of the conventionally sintered $CaTiO_3$ resulting from silver electrodes. The alternating output voltage (V_{CaTiO_3}) of the FAST sintered $CaTiO_3$ is significantly larger than the ones of the other tested samples. This significant increase in V_{CaTiO_3} is the first evidence that FAST sintered $CaTiO_3$ shows piezoelectric behaviour. The magnitude of charge produced through direct piezoelectric effect is discussed in next Chapter.

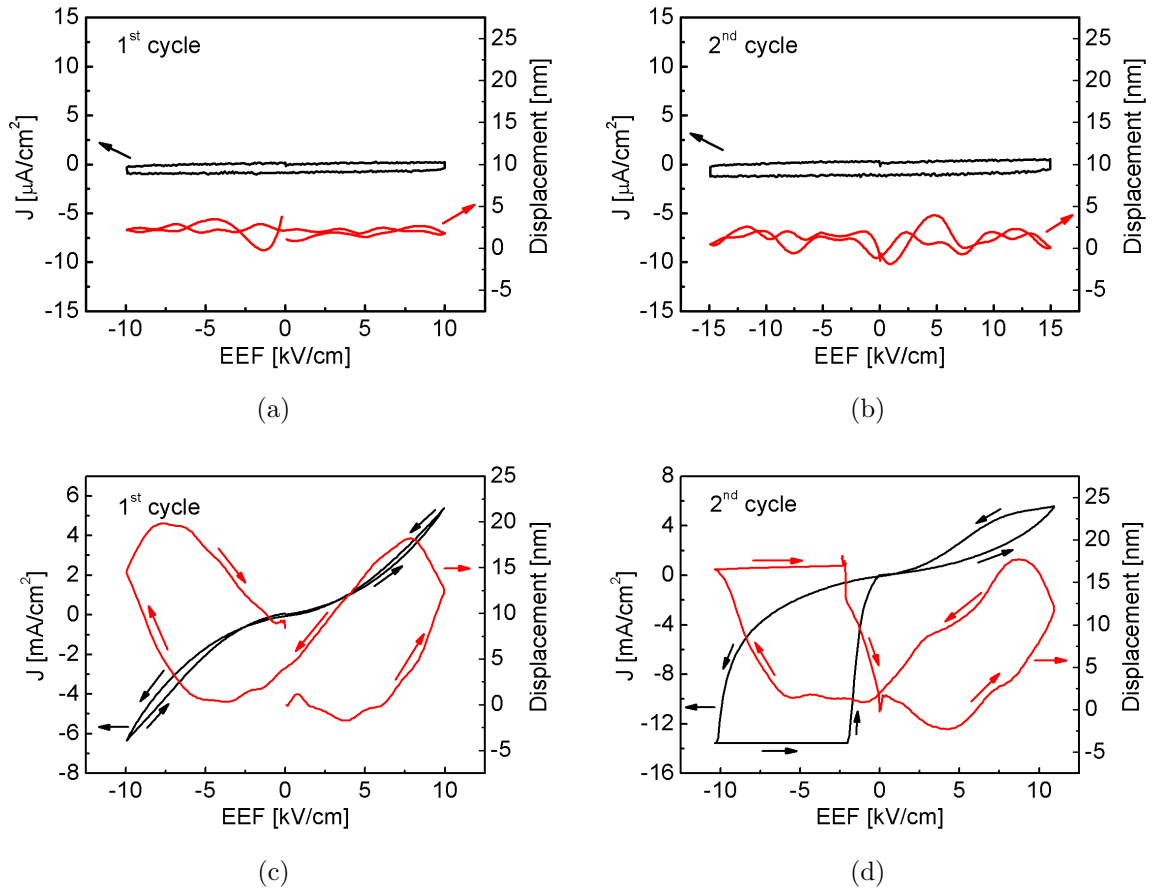


Figure 5.7: Displacement and J-EEF characteristic curves with EEF of (a) ± 10 kV/cm (1st cycle) and (b) ± 15 kV/cm (2nd cycle) applied to conventionally sintered as well as EEF of (c) ± 10 kV/cm (1st cycle) and (d) ± 11 kV/cm (2nd cycle) applied to FAST sintered $CaTiO_3$, measured by inverse piezoelectric effect at room temperature and frequency of 1 Hz.

The measurements to investigate inverse piezoelectric effect of the conventionally (± 10 kV/cm in 1st cycle and ± 15 kV/cm in 2nd cycle) and the FAST sintered $CaTiO_3$ (± 10 kV/cm in 1st cycle and ± 11 kV/cm in 2nd cycle) are presented in Figure 5.7. It can be seen that no measurable displacement occurred in conventionally sintered $CaTiO_3$ in both cycles. There is approximately no flow of electric current (Figure 5.7a and 5.7b). However, in the FAST sintered $CaTiO_3$ a typical “butterfly” shaped hysteresis curve can be seen. During the 1st cycle of EEF, the displacement is observed, when the EEF was increased from 0 kV/cm to +10 kV/cm. This displacement then decreases, when EEF goes from +10 kV/cm to 0 kV/cm. The same kind of displacement is also observed on the negative side of the EEF. Finally, the displacement goes approximately back to its initial position when the EEF is again reduced to 0 kV/cm. This observed displacement is the second evidence of piezoelectricity in FAST sintered $CaTiO_3$. The same process is repeated during 2nd cycle and displacement is observed again, but this time the conductivity increases slightly in the direction of positive EEF as compared to 1st cycle. In addition, there is an overflow of electric current in negative EEF direction which was beyond the limitations of the experimental setup. However, it goes back to a measurable value when the EEF is reduced to approximately -2 kV/cm and then returns to 0 kV/cm. The values of d_{33+} and d_{33-} computed by Figure 5.7 and their average d_{33} are presented in Table 6.1. It is important to mention that only d_{33+} (not d_{33-}) value is reported for the 2nd cycle of FAST sintered $CaTiO_3$, because of lost displacement curve data in negative EEF direction.

5.7 Structure evolution - HEXRD

The piezoelectric behaviour is purely generated from the crystal structure of any material, i.e. breaking of perfect crystal symmetry [35]. The observed piezoelectric behaviour in $CaTiO_3$ is generated due to the structural changes (defects or distortions) during FAST sintering. Lattice distortion in any material results in the change of lattice parameters [127]. Therefore, lattice parameters of all samples are compared. Additionally, structural distortions in FAST sintered $CaTiO_3$ are analyzed in detail without EEF as well as under EEF, which are discussed in this Section as well as in next Chapter.

5.7.1 Lattice parameters

Lattice parameters of calcinated powder, conventionally and FAST sintered $CaTiO_3$ from single shot experiment (without EEF) are presented along with literature values (dotted lines) [40] in Figure 5.8. In the calcinated powder, the lattice parameter b is very close to the corresponding literature value, but a and c are significantly larger. This may be caused by the interstitials present on well-defined lattice sites [45]. A significant decrease in the lattice parameters a and c is noticed, while b remains approximately constant after conventional sintering of calcinated powder. This decrease in lattice parameters can be interpreted as the removal of interstitials from lattice sites. Another possible reason is that, if the defects were present in calcinated powder, they could cure themselves during conventional sintering in air. As a result, the lattice parameters of conventionally sintered $CaTiO_3$ are comparable to literature values. For the FAST sintered sample, the lattice parameters b and c decrease slightly and a remains approximately constant as compared to the calcinated powder. The lattice parameters a and

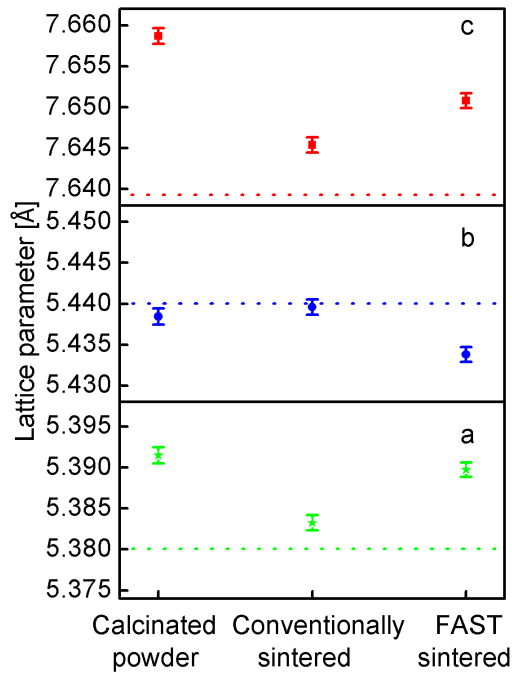


Figure 5.8: Lattice parameters of calcinated powder, conventionally and FAST sintered $CaTiO_3$. The literature values in dotted lines are also presented [40].

c are still significantly larger than the literature values, but b becomes significantly smaller. The lattice parameters differ significantly from literature values indicating the possibility of a large amount of oxygen lattice vacancies and distortions produced by defects inside the lattice. These defects are produced most probably by FAST sintering in vacuum, similar to those observed in $BaTiO_3$ under reducing sintering conditions [31].

5.7.2 Lattice distortion

In polycrystalline material, the random orientation of individual crystallites prevents to provide full representation of the material, which is an important component when evaluating ferroelectric or piezoelectric materials under EEF (or without EEF). Whereas, azimuthal sectors dependent data gives full information of the material. These azimuthal sectors provide information about the planes which are orientated at a certain angle with the initial angle of azimuthal sector [128]. This means that if 002, 020, 200 or any other reflection for the 90° azimuthal sector is examined, then the lattice planes in diffraction pattern measured for this sector are oriented 90° away from the initial angle. This initial angle of sample is denoted as the 0° azimuthal sector. Therefore, structural evolution can be determined dependent on azimuthal sectors.

The evolution of integrated 2D reflections of FAST sintered $CaTiO_3$ was examined when incident X-ray beam was subsequently in parallel and perpendicular direction to SF. This measurement was taken before in-situ HEXRD experiments (without EEF). Figures 5.9a and 5.9b present the main peak reflections with highlighted 90° and 180° azimuthal sectors shown in white region. Their contour plots of diffraction intensities

are presented in Figures 5.9c and 5.9d, respectively. The 2D pattern of main peak is almost straight (Figure 5.9a) and there is no observable difference in its corresponding peak (Figure 5.9c) when the SF was parallel to incident X-ray beam. Whereas, when the SF was perpendicular to incident X-ray beam, it produced 2D zigzag pattern of the

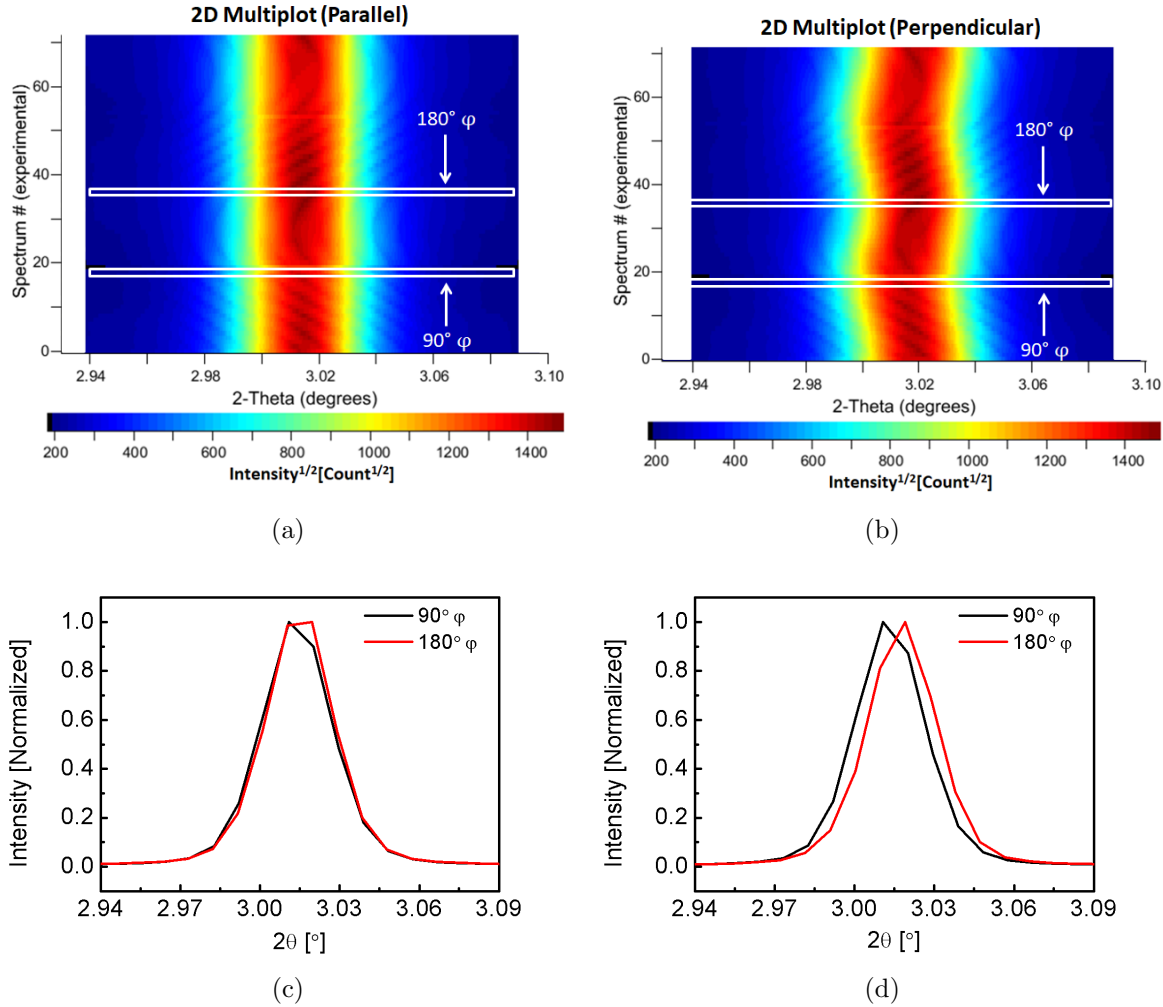


Figure 5.9: The evolution of integrated 2D main peak reflection at 90° and 180° azimuthal sectors when incident X-ray beam was (a) parallel and (b) perpendicular directions to SF. (c) and (d) contour plots of diffraction intensities of main peak reflections which are the projection of (a) and (b), respectively.

main peak (Figure 5.9b), which resulted in the shift of its corresponding peak (Figure 5.9d). This is the evidence that lattice distortion is present in the sample influenced by FAST sintering. However, it is unclear that why structural distortions are observed just in perpendicular but not in parallel direction of incident X-ray beam to SF. It is possible that complete structural information in perpendicular direction was collected which was not possible in parallel direction.

Supposedly, the sintering current flows in a straight path during FAST sintering. This means that when sample was exposed to X-rays during HEXRD measurements, the sintering current direction was initially perpendicular and then parallel to incident X-ray beam after sample rotation of 90°. It can be interpreted that X-rays intersect every foot print of sintering current in the sample when incident X-ray beam was perpendicular

to SF, leading to observable lattice distortions. Whereas, the intersection between X-rays and foot prints of sintering current were minimized when incident X-ray beam was parallel to SF direction. As a result, complete structural information was not collected. This can be understood with the help of Figure 5.10a which shows the scheme of flow of sintering current through the sample during FAST sintering. The ideal foot prints of the direction of current flow are denoted by blue arrows. Moreover, the part of the sample exposed by X-rays during HEXRD is also shown (with green region) in both perpendicular and parallel direction of SF.

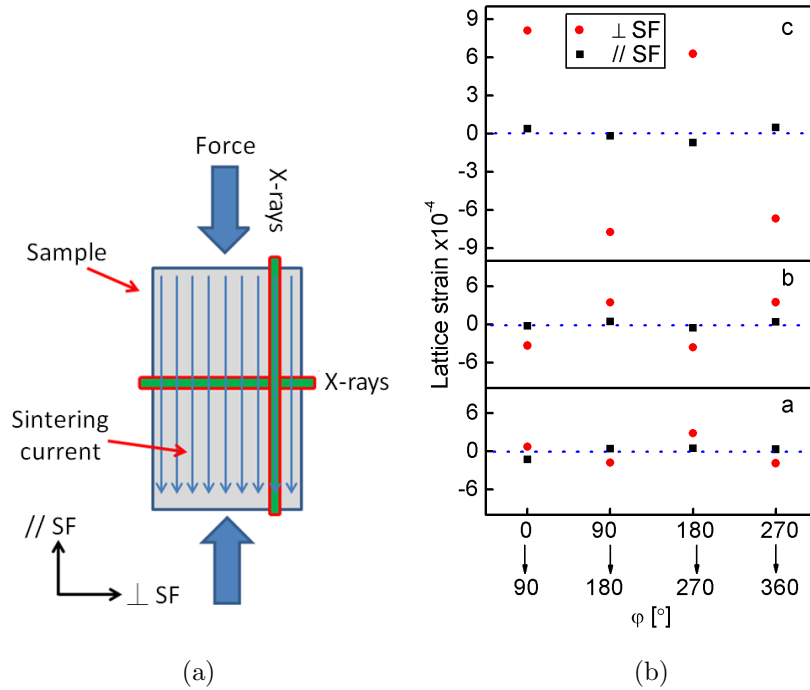


Figure 5.10: (a) Schematic flow of sintering current through sample during FAST sintering and intersection of their foot prints with incident X-rays during HEXRD experiment in perpendicular and then parallel direction. (b) Lattice strain vs azimuthal sector (without EEF). The red and black points represent the lattice strain when incident X-ray beam was perpendicular and parallel directions to SF, respectively. Additionally, blue dotted line presented the points having zero strain.

The change in actual d spacing due to applied stress on $CaTiO_3$ influenced by FAST sintering can reduce or expand the lattice spacing depending on the increase or decrease of the distance between lattice planes [10]. To validate this, the lattice parameter values of individual azimuthal sectors; 0° (360°), 90° , 180° and 270° were extracted by Rietveld refinement and then strain (ε) was calculated by using Equation 5.2.

$$\varepsilon = \frac{d - d_o}{d_o} \quad (5.2)$$

where d denotes the average value of lattice parameters at initial azimuthal sector and d_o is the average value of lattice parameters at final azimuthal sector [129].

The lattice strain in lattice parameters a, b and c vs azimuthal sectors is presented in Figure 5.10b, which provides complete information about lattice strain evolution

at every 90° step of azimuthal sectors. For example: the lattice strain shows the extent of distortion present in lattices from 0° to 90° azimuthal sector and so on. As mentioned before, no significant distortion in lattice parameters a, b and c was observed in parallel direction of incident X-ray beam to SF. Whereas, in perpendicular direction, maximum lattice stain is produced in lattice parameter c but lattice strain in a and b is also observed. This suggests that the maximum lattice strain influenced by FAST sintering is in lattice parameter c and for a and b is due to lattice redistribution in the crystal structure, which is influenced by the distortion produced in c. It is also worth mentioning that lattice strain in a and c is always produced in the same direction but the direction is opposite for b. Moreover, the lattice stains from 0° to 90° and 90° to 180° azimuthal sectors are always generated in the opposite directions. Similarly, 180° to 270° and 270° to 360° azimuthal sectors are also produced in the opposite direction. This means that the Debye-Scherrer rings of FAST sintered $CaTiO_3$ are not circular but elliptical in shape which ultimately generate electric dipole moments by shifting of negative and positive charges [130]. This is the evidence of structural change which creates piezoelectric response in FAST sintered $CaTiO_3$.

5.7.3 Lattice distortion under external electric field

Lattice distortion in FAST sintered $CaTiO_3$ at different azimuthal sectors as well as under an EEF is studied in this work for the first time. Appendix Figure C.1 presents HEXRD patterns when incident X-ray beam was parallel and perpendicular to EEF direction (with ± 13 kV/cm) at 0° azimuthal sector. No additional or new phase was observed under EEF except silver, which was identified when incident X-ray beam was parallel to EEF direction. This phase is observed due to silver electrodes applied on both sides of the sample. The lattice parameters extracted from the refinements of in-situ HEXRD are then plotted.

Figure 5.11 shows the lattice distortion in lattice parameters a, b and c under EEF at 0° and 90° azimuthal sectors. The lattice distortion in parallel and perpendicular direction of incident X-ray beam to EEF can be seen in Figures 5.11a and 5.11b, respectively. Other results of lattice distortions at 45°, 135°, 180°, 225°, 270° and 315° azimuthal sectors are presented in appendix Figures C.2, C.3 and C.4.

Total nine points are presented in these figures which are the measurement values with applied EEF. Point 1 represents the lattice parameter values of virgin sample, i.e. before applying EEF. The measurement was first executed in the positive EEF direction and then changed to the negative direction. Details of all points (1 to 9) are discussed in Chapter 4.

In Figure 5.11a, there is no notable shift in lattice parameters a, b and c without EEF (point 1) at each evaluated azimuthal sector when incident X-ray beam was parallel to EEF (reason already described in previous Section). Whereas, all lattice parameters under EEF always show linear expansion in both positive and negative direction of EEF. When EEF was removed (applied in positive or negative directions, i.e. point 3 or 7), all lattice parameters go back to their initial position (point 1) which are presented as point 5 and 9.

In Figure 5.11b, when incident X-ray beam was perpendicular to EEF, at point 1, i.e. without EEF, there is a significant shift in lattice parameter c from 0° to 90° azimuthal sector. This shift is due to distortion in the material as a result of FAST sintering. Slight

shift in lattice parameter b and no notable shift in a are also observed. Additionally, lattice parameter c compresses linearly and a expands linearly at 0° azimuthal sector under both (positive and negative) EEF directions. No change in lattice parameter b is observed under EEF. Whereas, at 90° azimuthal sector, all lattice parameters expand linearly under EEF, similar to the response observed when incident X-ray beam was parallel to EEF direction. It has to be noticed that every time after the removal of EEF, lattice parameters go back to their initial positions and do not expand or compress permanently. It indicates that electric dipoles are present inside the crystal structure and the domains are switchable. This kind of response should not be observed in non-ferroelectric and non-piezoelectric ceramics because it is purely piezoelectric response of a material [14]. The complete evolution of lattice distortion in lattice parameters a , b and c with each examined azimuthal sector as well as their expansion or compression under EEF is discussed in next Chapter.

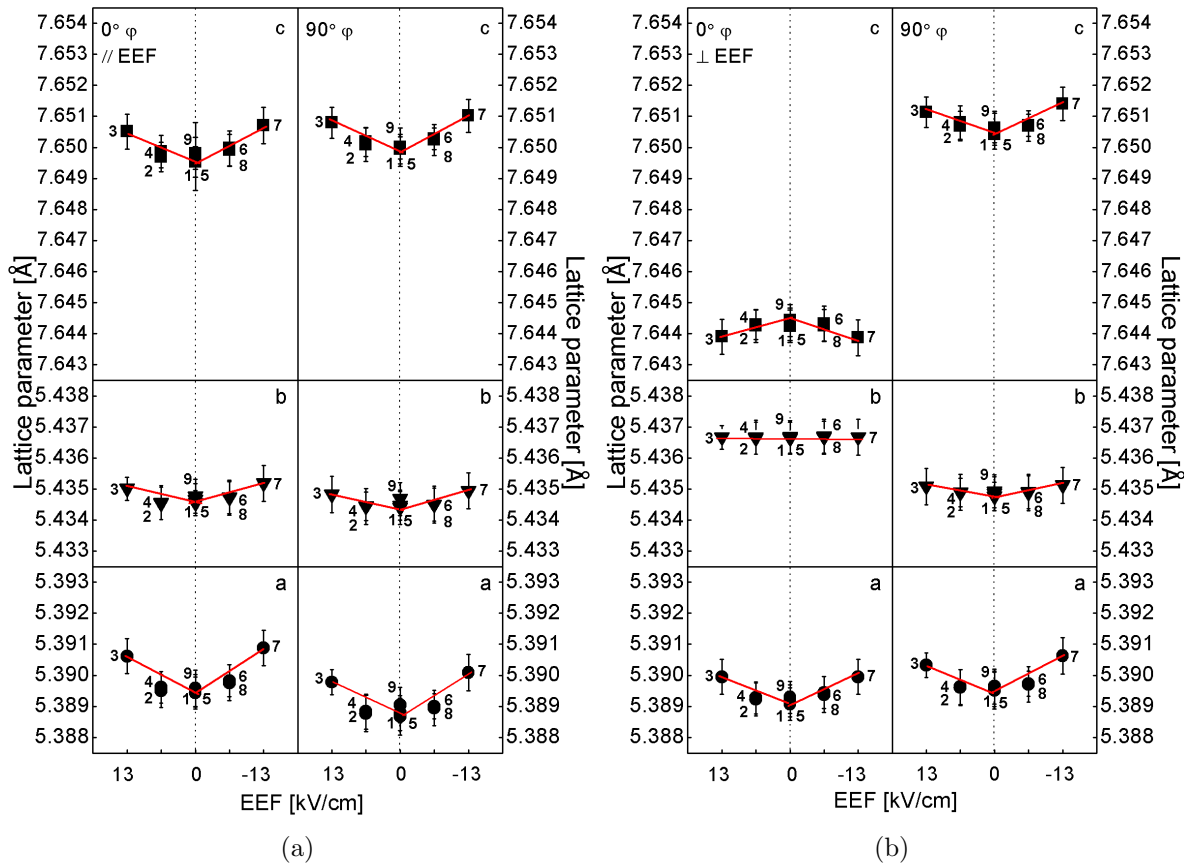


Figure 5.11: Evolution of lattice parameters of FAST sintered $CaTiO_3$ at 0° and 90° azimuthal sectors under EEF. Presented data points are measured when incident X-ray beam was in (a) parallel and (b) perpendicular direction to EEF.

5.7.4 Resistivity

During the in-situ HEXRD experiment, resistivity was also calculated from Equation 4.16 which is plotted against EEF in Figure 5.12. The points shown in the Figure are measurement sequence points (discussed in Chapter 4). It is worth mentioning

that in positive part of EEF cycle, the resistivity decreases from point 2 to point 4, which denotes initially applied EEF (6.5 kV/cm) and returns from point 3 (13 kV/cm), respectively. Similar trend of decrease in resistivity from point 6 to 8 (-6.5 kV/cm) is also observed in negative part of EEF cycle. Additionally, resistivity measured at point 7 (-13 kV/cm) also slightly decreased relative to point 3 (13 kV/cm). To summarize, it shows that the resistivity decreases significantly after a complete cycle indicating that apart from domains switching, slight diffusion of defects also happened at strong EEF which is referred to leakage current.

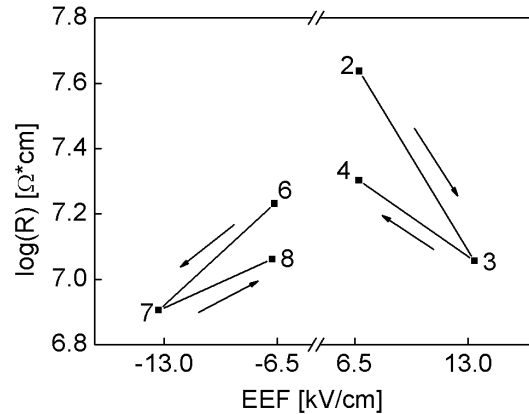


Figure 5.12: Resistivity of FAST sintered $CaTiO_3$ measured during in-situ HEXRD experiment. The reference resistance was $R_R = 1 \text{ M}\Omega$.

5.8 Mechanical effect - Nanoindentation

The indentation test was performed on FAST sintered $CaTiO_3$ with applied loads of 10, 20, 30, 40 and 50 mN with at least multiple of 7 measurements for each load. It was observed that after 30 mN, most of the loading curves exceed the calibrated depth which resulted in large errors in the values. Hence, indentation was eventually made at 10, 20 and 30 mN with large statistical values to ensure accurate values for the Young's modulus and hardness. The indentation load and unloading curves are presented in appendix Figure D.1. The Young's modulus and hardness determined from the nanoindentation are presented in Figure 5.13. It can be seen that the Young's modulus decreases from $(126.7 \pm 6.4) \text{ GPa}$ to $(117.8 \pm 5.5) \text{ GPa}$ with increase in applied load. This decrease in Young's modulus is caused by the effect of microstructure like grain boundaries or porosity present in sample [131], [132]. Whereas, all three values of hardness remain between $(12.5 \pm 0.7) \text{ GPa}$ to $(11.7 \pm 0.8) \text{ GPa}$.

Pure Ti that is widely used as implant material, has a disadvantage due to low strength and insufficient hardness. To optimize the Young's modulus and hardness, Ti alloys are successfully prepared with the range of hardness from $(2.4 \pm 0.3) \text{ GPa}$ to $(5.3 \pm 0.4) \text{ GPa}$ and Young's modulus from $(64.7 \pm 4.3) \text{ GPa}$ to $(122 \pm 6.2) \text{ GPa}$ [1]. However, they lack bioactive functionality (as mentioned in Chapter 1). Few years ago, mechanical properties of sol-gel $CaTiO_3$ (bioactive) coating on titanium were investigated by Stanishevsky et al and Young's modulus of $(160 \pm 10) \text{ GPa}$ and hardness from $(7.0 \pm 1.5) \text{ GPa}$ to $(9 \pm 1) \text{ GPa}$ were reported [131]. These values are very close to the values

of Young's modulus and hardness reported in this work. This finding opens the possibility of implanting pure FAST sintered $CaTiO_3$ without surface coating which will also provide bioactive functionality. However, it may cause osteopenia (stress shielding) [133] which can be overcome via increasing the porosity of $CaTiO_3$ by optimizing the sintering conditions.

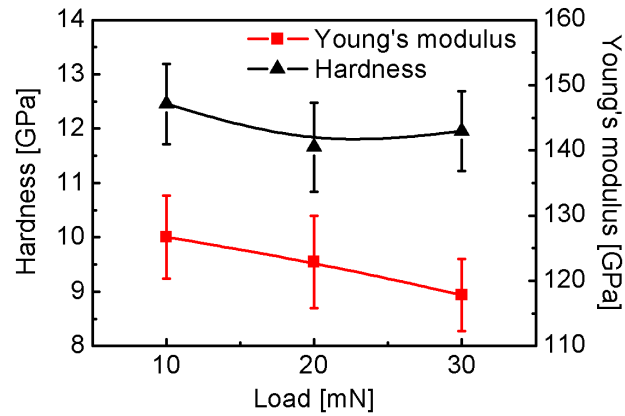


Figure 5.13: Young's modulus and hardness of FAST sintered $CaTiO_3$ as a function of applied load.

Chapter 6

Discussion

Controlled grain size, lattice oxygen vacancies (point defects) and lattice strain (distortions) are noticed in $CaTiO_3$ which was densified by FAST sintering. It also exhibits piezoelectric behaviour. Moreover, the change in its crystal structure under EEF is observed. All these observations will be discussed in the following ways:

Firstly, possible reasons of observed piezoelectric behaviour in FAST sintered $CaTiO_3$ will be described. Overflow of electric current in FAST sintered samples with the application of repeated EEF will be interpreted. The charge produced by densified samples and the piezoelectric constants of piezoelectric ceramics, bone, tendon and FAST sintered $CaTiO_3$ will be compared.

Secondly, the changes in crystal structure of FAST sintered $CaTiO_3$ observed by in-situ HEXRD experiment including *non* – 180° domain wall motion, lattice vibrations under the application of alternating voltage and lattice strain under EEF will be discussed. Detailed evolution of lattice parameters (without or under EEF) with azimuthal sectors will be linked to observed piezoelectric behaviour of FAST sintered $CaTiO_3$.

Thirdly, the visualization of defective crystal structure of FAST sintered $CaTiO_3$ and changes in its bond angles and bond lengths caused by oxygen vacancies or lattice distortions will be linked to in-situ HEXRD results.

Fourthly, texture evolution and the preferred orientation as well as effect of poling treatment will be discussed.

6.1 Pseudo piezoelectricity in field assisted sintered $CaTiO_3$

As presented in Section 5.6, the FAST sintered $CaTiO_3$ shows a response for both direct and inverse piezoelectric effect. This observation is referred to as a pseudo piezoelectric effect, due to the fact that $CaTiO_3$ belongs to the space group which does not show piezoelectric behaviour. The observed piezoelectric effect is most likely a result of the defective structure of $CaTiO_3$ and therefore referred to as a pseudo piezoelectric behaviour. Oxygen vacancies generate lattice distortions in $CaTiO_3$ at elevated temperature during FAST sintering in vacuum. This process can be described with the help of Kröger-Vink notation [39] by following equilibrium [42]:



where O_o is a lattice oxygen, V_o is a lattice oxygen vacancy and e is an electron. The equilibrium constant K of this reaction leads to information regarding the concentration of lattice oxygen vacancies inside FAST sintered $CaTiO_3$ [42]:

$$[V_O] = Kn^{-2}p(O_2)^{-1/2} \quad (6.2)$$

with n being the concentration of electrons and $p(O_2)$ is the surrounding oxygen pressure (discussed in detail in Chapter 2).

Equation 6.2 shows that the formation of lattice oxygen vacancies increases under vacuum conditions. Experimental results of lattice parameters and defect analysis confirmed the presence of defects due to oxygen vacancies as well as the lattice distortions in FAST sintered $CaTiO_3$. It is possible that the defects create instability of normal TiO_6 octahedra, which results in slight shift of the geometrical midpoint. This type of geometrical configurations carries electric dipole moments leading to piezoelectric behaviour [25], [134]. However, the defects have to be localized. There are two possibilities to fulfill this condition. First possibility

is by suppressing the grain growth and increasing grain boundary areas as pinning points. These grain boundaries can act like blocking positions for migration and prevent diffusion of defects causing permanent electric dipoles [135]–[137]. Second possibility is the stabilization of domain walls by preventing the defects of migration into their equilibrium configuration, through significantly increasing the mobility of domain walls. This can be accomplished by rapid cooling above the Curie temperature, which freezes the distorted state of the defects [25]. Both requirements are met by FAST sintering as it has the advantage of short heating and cooling times, while applying a pressure which allows fast densification, limited grain growth and increased grain

boundary areas as well as the freezing of distorted state of defects [32], [138]. It is also shown that oxygen vacancies of $CaTiO_3$ prefer to reside within twin boundary walls being energetically favourable, which results pinning of the walls [52]. Furthermore, oxygen vacancies can preferably exist near grain boundaries in $SrTiO_3$ [139]. Another reason for lattice distortions in the investigated sample can be the flow of direct current pulses inside the sample during FAST sintering. Since, powder inside the die is not completely homogeneous or dense, this feature of the powder creates a complicated network of current. The fluctuating hot spots formed in the path of current due to Joule heating may lead to lattice distortions, which freeze themselves due to rapid heating and cooling rates [26]. Therefore, the observed pseudo piezoelectricity of FAST sintered $CaTiO_3$ is most likely an outcome of lattice distortions resulting from the formation of defects and their localization during the sintering process.

It is also worth mentioning that the FAST sintered $CaTiO_3$ showed a piezoelectric re-

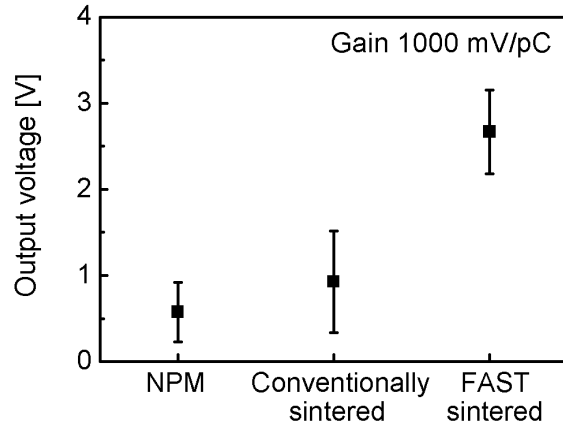


Figure 6.1: Output voltage produced by NPM, conventionally and FAST sintered $CaTiO_3$ measured by direct piezoelectric effect with dynamic method.

sponse using direct piezoelectric method without a poling treatment. The reason for generating such effect could be that some of the electric dipoles already aligned themselves during the FAST sintering process due to the pulse directed current. Figure 6.1 presents the output alternating voltage generated by NPM, conventionally and FAST sintered $CaTiO_3$ measured by direct piezoelectric effect with dynamic method. It can be seen that FAST sintered sample produces significantly increased output alternating voltage as compared to conventionally sintered sample and NPM which are close to zero value. The charge (Q) produced on the surfaces of conventionally and FAST sintered $CaTiO_3$ with this effect is calculated by Equation 6.3:

$$Q_{CaTiO_3} = \frac{V_{CaTiO_3}}{Gain} - \frac{V_{NPM}}{Gain} \quad (6.3)$$

where V_{NPM} and V_{CaTiO_3} are output alternating voltages of NPM and $CaTiO_3$, respectively.

The generated surface charges on conventionally and FAST sintered $CaTiO_3$ are found to be (0.9 ± 0.6) pC and (2.7 ± 0.5) pC, respectively.

The displacement observed using the inverse piezoelectric method occurred due to polarization, which leads to an alignment of more electric dipoles (domain switching) by applying a strong EEF. When an EEF is applied, some electrons flowing through the material reduce the metal cations, i.e. Ti^{+4} to Ti^{+3} or Ca^{+2} to Ca^{+1} , which were created by the trapping of electrons. This effect is observed in the J-EEF characteristic curve during the 2nd cycle (see Figure 5.7d), which shows relatively high conductivity in the range of +11 kV/cm to 0 kV/cm as compared to 0 kV/cm to +11 kV/cm. This reveals an increase in the number of defects which increases the flow of electrons in an EEF [24]. As a result, it causes the increase in electric dipole moments which also start to align due to the EEF. The alignment of electric dipoles becomes stronger in the next cycle of the EEF which is a consequence of electron flow due to the measurement procedure. In every cycle, more defects are produced which can act as trapping sites for charge carriers. Eventually, the material has enough defects and electric dipole density that it opens conducting channels causing an overflow as in $SrTiO_3$ [140]. It is also important to mention that electrical conductivity is a defect sensitive property, because defects are electrically charged [42]. At a certain limit, defects' concentration can overcome the enthalpy of motion for charge carriers, leading to their diffusion under strong EEF. Therefore, there should be enough defects to create electric dipoles with significant strength, but not too many defects to open conducting channels causing overflow. This overflow is observed during the 2nd cycle in Figure 5.7d in negative EEF direction, which indicates the disappearance of the pseudo piezoelectric behaviour. In addition, HEXRD results showed the α - TiO_2 phase impurity of (5.6 ± 0.6) wt% which can also contribute to an increasing conductivity, as TiO_2 can significantly reduce resistivity even under small EEF [24]. Nevertheless, the presence of restoring force upon reducing the EEF in every cycle can be seen, which can arise from the contribution of stress-induced instability of the ferroelastic domain wall switching.

Aging effect was also tested through direct piezoelectric measurement after keeping the sample at room temperature for 4 weeks. Approximately, same value of charge was generated as produced immediately after FAST sintering. This suggests a very low diffusion or migration of defects at lower temperature and without strong EEF.

6.2 Piezoelectric matrix and constant

A complete set of d_{ij} can be represented by the matrix shown as M_1 [141]. This matrix can be deduced based on non-centro-symmetric point groups in crystals. For instance, the matrix of the piezoelectric ceramic belongs to crystals of the tetragonal symmetry (point group 4mm) represented as M_2 [19]. Moreover, M_3 represents the matrix of certain structures of living organisms such as bone and tendon [142]. The orthorhombic crystal structure of $CaTiO_3$ belongs to centro-symmetric point group (mmm). This implies that all of its d_{ij} values are zero. However, in the defective structure of FAST sintered $CaTiO_3$, the d_{33} value is not zero.

Piezoelectric ceramics, bone and tendon	Piezoelectric constant	References
PZT	up to 600 pC/N	[4]
$BaTiO_3$	$d_{33} = 68.5 - 316.6$ pm/V $d_{31} = -33.4 - (-103.3)$ pm/V	[14]
Bone of ox Bone of man	$d_{14} = 0.2 - 0.7$ pC/N $d_{14} = 0.12$ pC/N	[5]
Animal cortical bone	shear $d = 0.1 - 0.3$ pm/V	[143]
Achilles tendon of ox and horse	$-d_{14} = d_{25} = 2.66$ pC/N $d_{15} = d_{24} = 1.4$ pC/N $d_{31} = d_{32} = 0.087$ pC/N $d_{33} = 0.067$ pC/N	[6]
Dried beef bone Wet beef bone (with pH 5.0) Dried beef bone Wet beef bone (with pH 6.88)	$d_{33} = 0.15$ pC/N $d_{33} = 0.73$ pC/N $d_{31} = 0.066$ pC/N $d_{31} = 9.33$ pC/N	[144]
FAST sintered $CaTiO_3$ (1 st cycle)	$d_{33+} \sim 7.134$ pm/V $d_{33-} \sim -5.950$ pm/V average $d_{33} \sim 0.595$ pm/V	
FAST sintered $CaTiO_3$ (2 nd cycle)	$d_{33+} \sim 7.189$ pm/V	

Table 6.1: Comparison of d_{33} values of FAST sintered $CaTiO_3$ with other d_{ij} values of perovskite ceramics, natural bone and tendon.

$$M_1 = \begin{bmatrix} d_{11} & d_{12} & d_{13} & d_{14} & d_{15} & d_{16} \\ d_{21} & d_{22} & d_{23} & d_{24} & d_{25} & d_{26} \\ d_{31} & d_{32} & d_{33} & d_{34} & d_{35} & d_{36} \end{bmatrix}$$

$$M_2 = \begin{bmatrix} 0 & 0 & 0 & 0 & d_{15} & 0 \\ 0 & 0 & 0 & d_{15} & 0 & 0 \\ d_{31} & d_{32} & d_{33} & 0 & 0 & 0 \end{bmatrix}$$

$$M_3 = \begin{bmatrix} 0 & 0 & 0 & d_{14} & d_{15} & 0 \\ 0 & 0 & 0 & d_{15} & d_{-14} & 0 \\ d_{31} & d_{32} & d_{33} & 0 & 0 & 0 \end{bmatrix}$$

Fukada and Yasuda demonstrated the piezoelectric effect in bones of ox and man for the first time in 1975 and measured the corresponding d_{14} values [6]. Since then, different d_{ij} values of bone have been reported [6], [141], [142]. The variation in these values is mainly caused by the contribution of streaming potentials in bone. These streaming potentials can differ with pH value of the solution and are responsible for change in d_{ij} values of the bone. It is reported that d_{31} values vary approximately by two order of magnitude in the same bone depending on the conditions [144]. Even though, all d_{ij} values of bone are very small as compared to well-known perovskite piezoelectric ceramics [4], [14]. The d_{33} values of FAST sintered $CaTiO_3$ are very close to the ones of natural bone (Table 6.1). The reason for having small d_{33} value can be due to low electric dipole density and stability. FAST sintered $CaTiO_3$ is possibly showing pseudo piezoelectric behaviour due to localized defects with lattice distortions, but not from its normal crystal structure like other perovskite piezoelectric ceramics, e.g. PZT, $BaTiO_3$ or $SrTiO_3$. Using FAST sintered or similar $CaTiO_3$ ceramics as an implant material can be advantageous over commonly used materials due to the pseudo piezoelectric behaviour, which may increase osseointegration leading to bone remodelling and growth.

6.3 Non-180° domain wall motion

In ferroelectric materials, two types of domain walls are present which are 180° and non-180° domains. These domains separate in orientation by 180° and non-180° rotations, as described in Section 2.3.4. The motion of these domain walls can be driven by the application of EEF or mechanical stress. From the point of view of single unit cell (Figure 6.2), it can be considered that 180° domain wall motion results in polarization response and non-180° domain wall motion leads to the lattice distortion response [145]. The non-180° domains reorientation can be quantified by Bragg diffraction with the application of EEF. This Bragg diffraction is sensitive to non-180° domains reorientation, which leads to a preferred distribution of diffraction pattern intensity as a function of azimuthal sector angle [128].

Hence, diffraction pattern can be used to observe the contribution of non-180° domains reorientation causing lattice distortions and piezoelectric response [146]. However, 180° domains reorientation is not sensitive to Bragg diffraction.

Figure 6.3 presents the diffraction patterns with corresponding Miller indices of FAST sintered $CaTiO_3$ along with α - TiO_2 phase at 0°, 45° and 90° azimuthal sectors with an

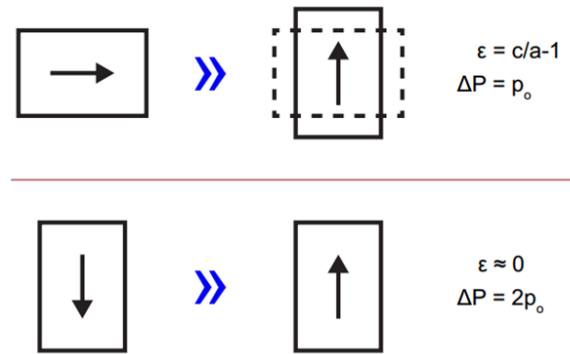


Figure 6.2: Schematic representation of (top) non-180° domain reorientation contributed to lattice distortion and (bottom) 180° domain reorientation contributed to polarization. The change in polarization (ΔP) is presented as the polarization (P_o) of single crystal [145].

EEF amplitude of +13 kV/cm. In both figures, top and bottom patterns correspond to the diffraction peaks when EEF was parallel and perpendicular to incident X-ray beam, respectively. The peaks shown in the figures are small segments of larger diffraction pattern, which are used for direct comparison of the intensity change in $CaTiO_3$ and α - TiO_2 phases. No significant change in all intensities is observed in both (top left

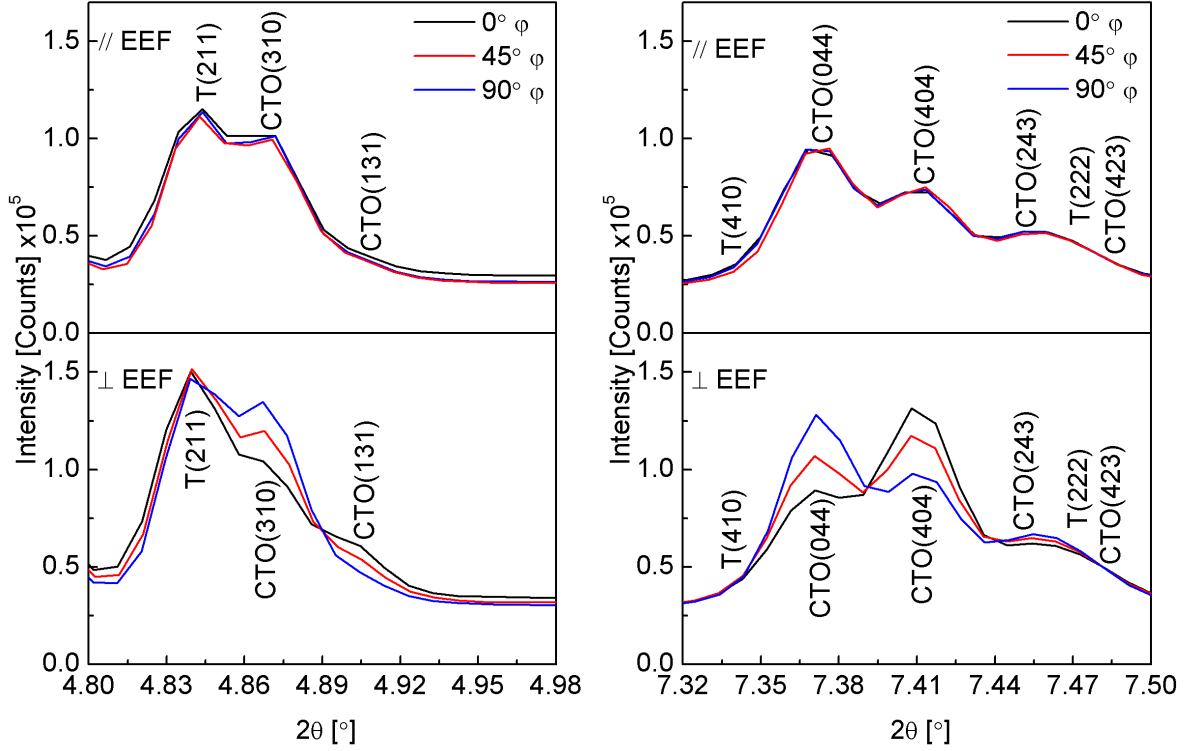


Figure 6.3: HEXRD patterns of three different azimuthal sectors under EEF of +13 kV/cm applied in parallel and perpendicular directions to incident X-ray beam. The peaks of FAST sintered $CaTiO_3$ and α - TiO_2 are labeled by corresponding Miller indices ($CaTiO_3$ - CTO and α - TiO_2 - T).

and top right) figures. This can be due to the same reason discussed before. However, it is noticed in Figure 6.3 (left bottom) that there is no change in (211) reflection of α - TiO_2 . Whereas, intensity of (310) and (131) reflections of FAST sintered $CaTiO_3$ changes from 0° to 90° azimuthal sectors. Similar trend of intensity changes in (044), (404) and (243) reflections of FAST sintered $CaTiO_3$ is also noticed in Figure 6.3 (right bottom). On the contrary, (423) reflection of FAST sintered $CaTiO_3$ which is a tail of the peak and (410) and (222) reflections of α - TiO_2 phases remain unchanged. These intensity changes are an uncommon phenomena observed in FAST sintered $CaTiO_3$. It suggests that non-180° domains reorientation occurred and was accompanied by lattice distortions in crystal structure. This is a proof of structural changes which are observed directly by diffraction pattern leading to pseudo piezoelectric behaviour in FAST sintered $CaTiO_3$. Additionally, no intensity change in α - TiO_2 phase at all azimuthal sectors confirms that structural changes occurred only in $CaTiO_3$ but not in α - TiO_2 phase.

Apart from comparing the distribution of diffraction pattern intensities as a function of 2θ at different azimuthal sectors, comparison of peaks with (± 13 kV/cm) and without (0 kV/cm) EEF is performed, as presented in appendix Figure C.5. It also confirmed that the intensity of diffraction peaks significantly changed when EEF was applied from 0 kV/cm to ± 13 kV/cm. This change in intensity suggests further reorientation of non- 180° domains in FAST sintered $CaTiO_3$ when EEF was applied during in-situ HEXRD experiment.

6.4 Lattice strain and lattice vibration under external electric field

Lattice strain

The piezoelectric property of polycrystalline material is generated by the distortions in crystal structure produced by lattice strain [147]. This lattice strain is observed in $CaTiO_3$ after FAST sintering (virgin sample) as a function of azimuthal sectors (discussed in Section 5.7.2).

Currently, the lattice strain is examined as a function of azimuthal sectors under EEF. This estimates the magnitude of expansion or compression of crystal structure caused by lattice strain. To perceive the lattice strain evolution produced with EEF of ± 13 kV/cm at individual (0° (360°), 45° , 90° , 135° , 180° , 225° , 270° and 315°) azimuthal sectors, Equation 5.2 is used for lattice strain calculation. However, this time, d denotes the values of lattice parameters without EEF and d_o denotes the values of lattice parameters under EEF. In other words, it is assumed that d is strain free lattice parameter (without EEF) and d_o is lattice parameter with lattice strain (under EEF). The calculated lattice strains at each azimuthal sector are then plotted and presented in appendix Figures C.6, C.7, C.8 and C.9.

Figure 6.4 presents azimuthal sector versus lattice strain produced by EEF of ± 13 kV/cm. These values of lattice strain at individual azimuthal sector with EEF of $+13$ kV/cm and -13 kV/cm are averaged and then plotted. Each point in the figure represents the lattice strain at every 45° step of azimuthal sector. It is important to

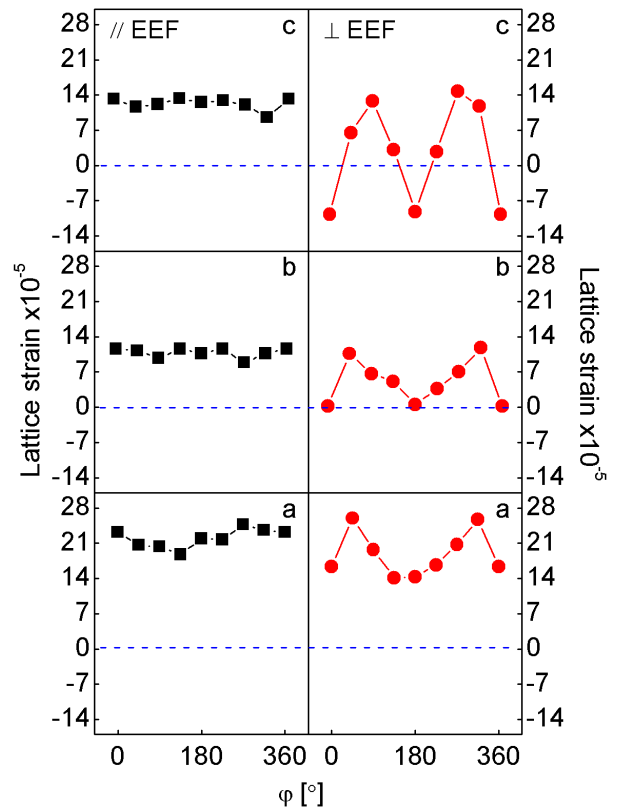


Figure 6.4: Azimuthal sector vs lattice strain under EEF of ± 13 kV/cm applied in parallel (black) and perpendicular (red) directions to incident X-ray beam. Blue dotted lines represent zero lattice strain (without EEF).

mention that the lattice strain already present in $CaTiO_3$ due to FAST sintering is neglected and it is assumed that lattice parameters are without strain when no EEF is applied which are shown as blue dotted lines.

When incident X-ray beam was parallel to EEF direction, the lattice strain produced only in positive direction in all lattice parameters is shown by black colour. The maximum lattice strain is observed in lattice parameter a, minimum in b and intermediate in c. Additionally, the lattice strain produced in each lattice has almost same magnitude at all azimuthal sectors. This indicates the expansion of all lattice parameters, i.e. the expansion of crystal structure in range of 10^{-5} at all azimuthal sectors.

The results generated when EEF was in perpendicular direction to incident X-ray beam are different from those when EEF was in parallel direction and also conform to the previous results. The lattice parameters show dependence of lattice strain on azimuthal sectors presented by red colour. It can be seen that at 0° azimuthal sector, the lattice strain in lattice parameters c and a is in negative and positive direction respectively, with no lattice strain generated in b. This indicates that when a expands, c compresses with no change in b. After 45° step which is 45° azimuthal sector, an increase in lattice strain is observed in a and b. Whereas, lattice strain in c decreases and then increases again. Following 45° azimuthal sector, a decrease in lattice strain in a and b is observed till 180° azimuthal sector. However, lattice strain in c increases further till 90° azimuthal sector. It then decreases almost till 135° azimuthal sector and increases again in opposite (negative) direction till 180° azimuthal sector. At this (180°) azimuthal sector, the produced lattice strains are very similar to those observed in 0° azimuthal sector. This is the region of azimuthal sector with half circle of Debye-Scherrer ring. The other half circle seems to be the mirror image of first half of Debye-Scherrer ring which causes the “M”like shape.

It can also be seen that the rise and decline in magnitude of lattice strain generated by EEF between 0° and 180° azimuthal sectors are almost 1.5 times in lattice parameter c as compare to a and b. This indicates that the maximum distortion upon applying EEF is produced in c because of expansion (positive lattice strain) and compression (negative lattice strain) as a function of azimuthal sector. Previously, it was also noticed that maximum lattice strain was generated in c after FAST sintering (without EEF Figure 5.10b). These results suggest that main contribution in the generation of pseudo piezoelectric behaviour is exhibited by lattice parameter c and the change in a and b is influenced by c. This also implies that the expansion or compression of crystal structure is mainly dependent on lattice parameter c.

Lattice vibration

Apart from in-situ HEXRD experiment with DC source and high EEF, the experiment with AC source was performed to verify the piezoelectric response of FAST sintered $CaTiO_3$ produced by dynamic method. An attempt was carried out to examine the lattice vibrations by two techniques: Firstly, the periodic mechanical stress was applied to FAST sintered $CaTiO_3$ through piezo-actuator with the help of direct piezoelectric setup (described in Section 4.8.4). Secondly, the alternating voltage of 10 V with frequency of 10 Hz was applied directly to FAST sintered $CaTiO_3$ through RIGOL DG4062 function generator. During both measurements, diffraction patterns were also recorded simultaneously. Additionally, after the measurements, sample was rotated 90° and again periodic mechanical stress as well as alternating voltage were applied one

after another and diffraction patterns were also recorded. In this way, multiple patterns were recorded in both parallel and perpendicular direction of incident X-ray beam to SF.

MAUD program [105] was used to reduce 2D images into 1D patterns: intensity versus 2θ , by integration of complete Debye-Scherrer rings in 5° steps. The resulting diffraction patterns as well as the diffraction patterns of virgin FAST sintered $CaTiO_3$ were further examined using fityk software [114]. The main peaks of all patterns were fitted and fwhm values were compared. A trend in increase of fwhm of FAST sintered $CaTiO_3$ under oscillating mechanical stress or alternating voltage relative to virgin samples was noticed. This can be interpreted as; when the lattices of sample vibrate upon oscillating mechanical stress or alternating voltage, it causes broadening of the main peak. This is another proof of structural changes observed in FAST sintered $CaTiO_3$ which are not observed so far. Hence, due to these lattice vibrations, the charge produced on the surface of FAST sintered $CaTiO_3$ was observed in direct piezoelectric measurement (Figure 5.6b). It is worth mentioning that the trend of broadening of main peak by applying oscillating mechanical stress verifies direct piezoelectric response. In the same way, trend of broadening of main peak by applying alternating voltage verifies inverse piezoelectric behaviour of the sample.

6.5 Evolution of lattice parameters with azimuthal sectors

Pole diagrams are presented in Figure 6.5 to determine the complete evolution of lattice parameters of FAST sintered $CaTiO_3$ without and under EEF (± 13 kV/cm) as well as their comparison with literature values [40]. These pole diagrams are plotted to understand the phenomenon of distortions in crystal structure depending on EEF direction as well as the function of azimuthal sectors. The lattice parameter values of FAST sintered sample with positive and negative EEF are averaged and then plotted (as mentioned in Section 6.4). It is assumed that there is no change in literature values of lattice parameters as a function of azimuthal sector, as it has not been determined so far. Additionally, it is supposed that literature values of lattice parameters are without distortions.

It is important to mention that when EEF is parallel to incident X-ray beam, then after the scattering of X-rays, the EEF direction can be illustrated as perpendicular to 0° or 180° and parallel to 90° or 270° azimuthal sectors. Similarly, when EEF is perpendicular to incident X-ray beam, then after the scattering of X-rays, the EEF direction can be illustrated as parallel to 0° or 180° and perpendicular to 90° or 270° azimuthal sectors as presented in pole diagrams.

Firstly, the literature values [40] are compared with lattice parameters of FAST sintered $CaTiO_3$. Secondly, evolution of lattice parameters without EEF is determined. Thirdly, evolution of lattice parameters under EEF is examined. It can be seen that the literature values of lattice parameters a and c in Figures 6.5a, 6.5b, 6.5e and 6.5f are significantly smaller than the lattice parameters of FAST sintered $CaTiO_3$ (at 0 kV/cm as well as at ± 13 kV/cm). Whereas, literature value of lattice parameter b is slightly larger than FAST sintered sample as presented in Figures 6.5c and 6.5d. These results indicate that lattice oxygen vacancies cause lattice distortions which leads to

the expansion of lattice parameters a and c . However, slight compression in lattice parameter b relative to literature value is probably due to the lattice redistribution in crystal structure which resulted from expansion in a and c .

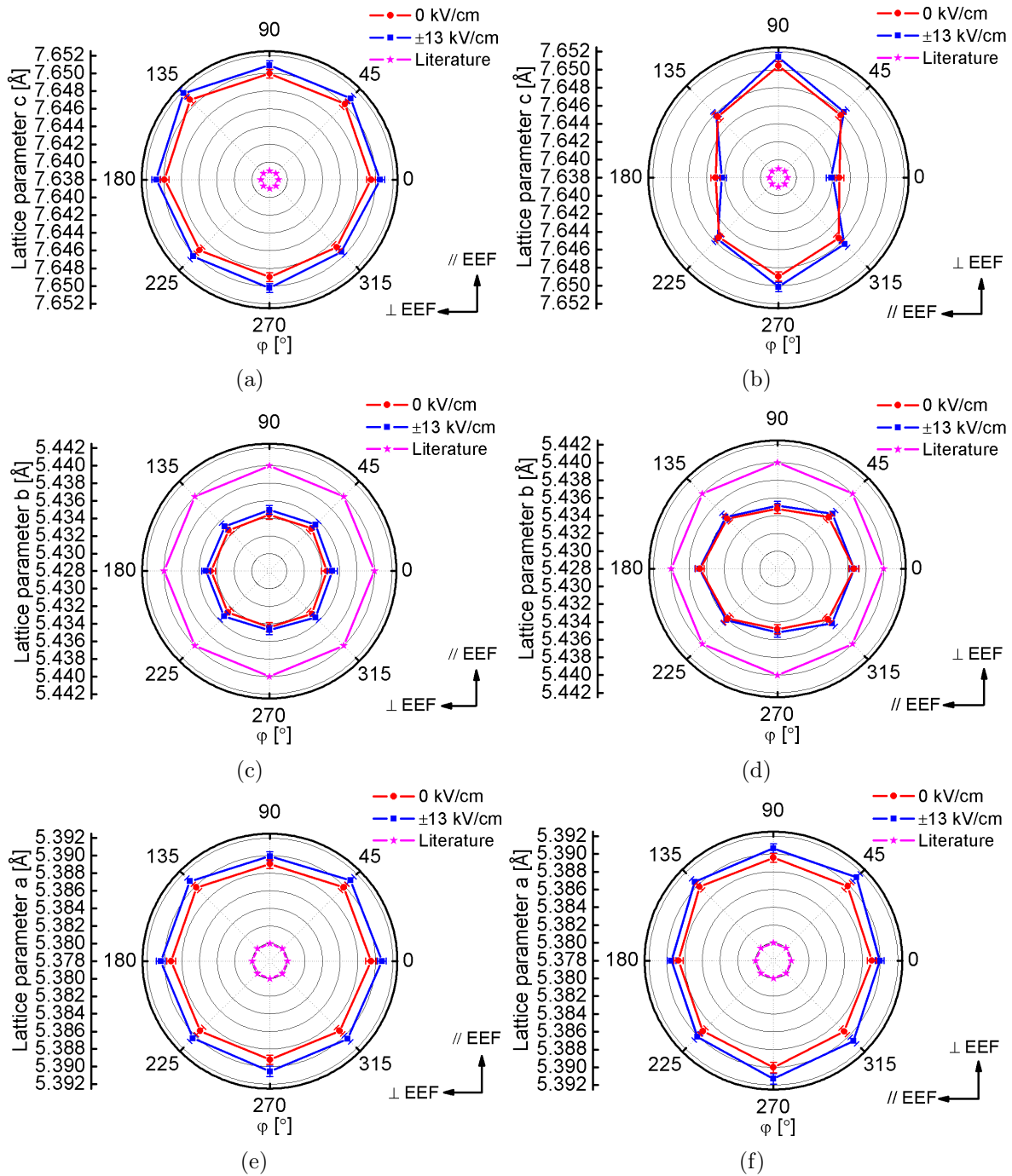


Figure 6.5: Pole diagrams representing azimuthal sectors vs lattice parameters of FAST sintered $CaTiO_3$. (a) Lattice parameter c , (c) lattice parameter b and (e) lattice parameter a , when EEF was in parallel direction to incident X-ray beam. (b) Lattice parameter c , (d) lattice parameter b and (f) lattice parameter a , when EEF was in perpendicular direction to incident X-ray beam. The lattice parameters with EEF (blue) and without EEF (red) as well as literature values (pink) [40] are presented.

Figures 6.5a, 6.5c and 6.5e show that all lattice parameters remain approximately unchanged as a function of azimuthal sectors when SF (without EEF) was parallel to incident X-ray beam. When EEF was perpendicular to incident X-ray beam, the response of crystal structure is more realistic and supports the previous results. All lattice parameters at this point will be discussed with the reference to literature values. It can be seen in Figure 6.5b that lattice parameter c of FAST sintered sample at 0° or 180° azimuthal sector has expanded less, relative to 90° or 270° azimuthal sectors and intermediate at 45° , 135° , 225° , 315° azimuthal sectors (without EEF). In contrast, lattice parameter b shown in Figure 6.5d at 0° or 180° azimuthal sector has compressed relatively more than that at 90° or 270° azimuthal sectors and intermediately at 45° , 135° , 225° , 315° azimuthal sectors (without EEF). Lattice parameter a , presented in Figure 6.5f, responds similar to c but the response of expansion as a function of azimuthal sector is very small (without EEF). It can also be seen that the maximum lattice distortion (function of azimuthal sector) is present in lattice parameter c , minimum in a and intermediate in b . Besides that, the minimum lattice distortion is generated in lattice parameter b with respect to literature values. It also shows that when lattice parameters a and c increase, b decreases as a function of azimuthal sector. This indicates that due to the expansion of lattice parameter c at certain azimuthal sectors, a also slightly expands but b compresses and vice versa. This is true in both ways, without considering the comparison with respect to literature values or with it. This means that the observed effects remain same and are independent of the assumption that literature values are without distortions.

Lattice parameter	$\varphi [^\circ]$	$\varepsilon(//SF)$	$\varepsilon(\perp SF)$
a	0	0.0017	0.0017
	90	0.0017	0.0018
b	0	-0.0010	-0.0006
	90	-0.0010	-0.0009
c	0	0.0014	0.0007
	90	0.0014	0.0015

Table 6.2: Lattice strain values of FAST sintered $CaTiO_3$ with respect to azimuthal sectors when SF was parallel and perpendicular to incident X-ray beam (without EEF).

As of now, the lattice strain in lattice parameters of FAST sintered $CaTiO_3$ is determined by two ways. Firstly, lattice strain (without EEF) as a function of azimuthal sectors is discussed in Section 5.7.2. Secondly, lattice strain generated as a function of EEF (from 0 kV/cm to ± 13 kV/cm) is discussed in Section 6.4. The lattice strain present in the sample relative to literature values and as a function of azimuthal sector is not included. It is supposed that it also contributes to the distortion of crystal structure. To calculate that, Equation 5.2 is used and it is assumed that literature values of lattice parameters are strain free. As an example, lattice strain values at 0° and 90° azimuthal sectors is calculated and presented in Table 6.2. The lattice strains in all lattice parameters have same values at 0° and 90° azimuthal sectors when sample was exposed to X-rays with SF in parallel direction. Whereas, lattice strain values at 0° azimuthal sector are significantly different from 90° azimuthal sector when sample was exposed to X-rays with SF in perpendicular direction. This difference in lattice strain is very small in lattice parameter a which slightly increases in b and notably in c (Table

6.2). Additionally, maximum lattice strain relative to literature values is produced in lattice parameter a and minimum in b .

As mentioned in Table 6.2 and discussed previously, the maximum lattice strain generated with respect to azimuthal sectors is in lattice parameter c . This implies that maximum impact of lattice distortion caused by FAST sintering is produced in lattice parameter c and change in a and b are regulated by c . Additionally, it is observed in Figure 6.5b (red color) that maximum elongation direction of lattice parameter c is at 90° or 270° ($\perp SF$) and minimum at 0° or 180° ($//SF$) azimuthal sectors. The reason of these maximum and minimum elongations in lattice parameter c is discussed in next section.

It is also worth mentioning that lattice strain generated after FAST sintering in lattice parameters a and c has positive values but negative in b , as presented in Table 6.2. This shows that lattice parameters a and c expand but b compresses after FAST sintering. Moreover, when incident X-ray beam was parallel to EEF, expansion of lattice parameters a , b and c in all azimuthal sectors is noticed when EEF was increased from 0 kV/cm to ± 13 kV/cm. It leads to the assumption that crystal structure always expands under EEF which is not true. It can therefore be interpreted that the structural information is overlooked. The possible reason of this error is already explained in Section 5.7.2. When EEF was applied to the sample in perpendicular to incident X-ray beam direction, both the elongation and compression were noticed. It can be seen in Figure 6.5b that lattice parameter c compresses at 0° or 180° and elongates at 90° or 270° as well as minor elongation at 45° , 135° , 225° and 315° azimuthal sectors under EEF. This suggests that if electric dipoles were slightly aligned during FAST sintering, they would have aligned further due to high EEF applied in the same (SF) direction which led to more distortion of lattice parameter c . However, lattice parameter b in Figure 6.5d remains unchanged at 0° and 180° azimuthal sectors (when lattice parameter c compresses) and a minor increase is observed at all examined azimuthal sectors (when lattice parameter c elongates). Though, lattice parameter a in Figure 6.5f always elongates regardless of azimuthal sectors. All of these responses of lattice parameters under EEF can be understood by crystal structure point of view, which will be discussed in next section.

It should also be mentioned that as the crystal structure is overlooked when EEF was parallel to incident X-ray beam, it was only possible to collect the information which is similar to 90° or 270° azimuthal sectors of EEF direction in perpendicular to incident X-ray beam.

6.6 Structure defects

The determination of defects near the surface analyzed through XPS (in Figure 5.5) suggested that oxygen vacancies are present in FAST sintered $CaTiO_3$. Moreover, due to lattice distortions and off centered Ti atom, pseudo piezoelectric behaviour is observed. This response originates from crystal structure which is analyzed in previous sections. To understand and visualize defective crystal structure of FAST sintered $CaTiO_3$, the graphical representation of unit cell of $CaTiO_3$ with defects is presented in Figure 6.6. The EEF/SF direction presented in Table 6.3 is referred to its direction which is parallel (0° azimuthal sector) or perpendicular (90° azimuthal sector) to diffracted X-rays.

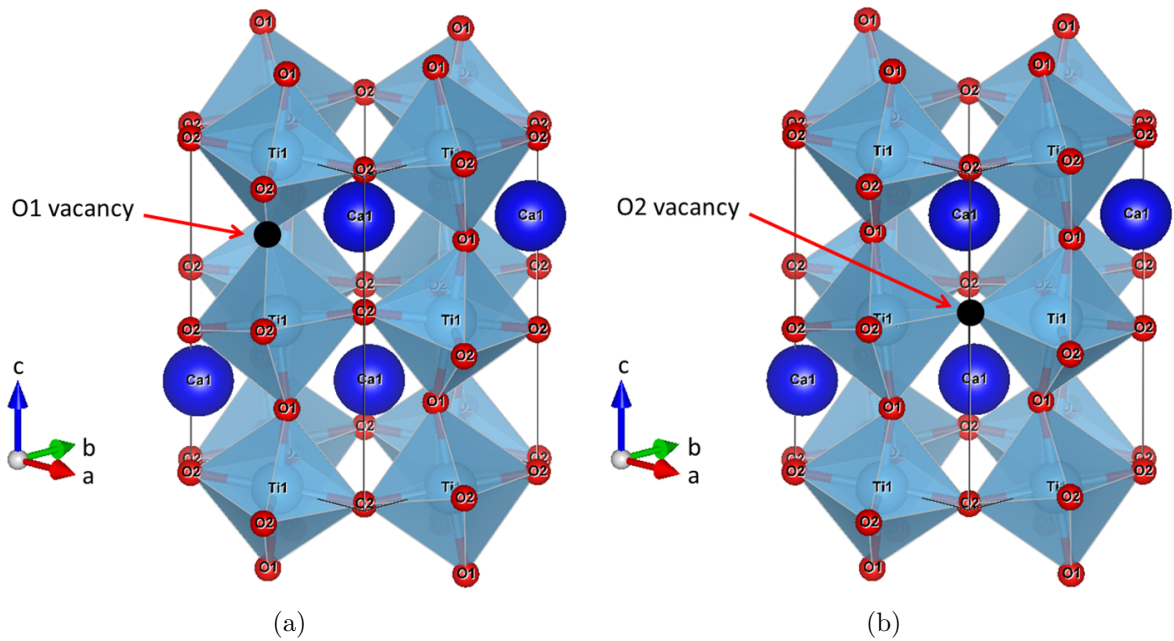


Figure 6.6: Graphical representation of the unit cell of $CaTiO_3$ with (a) O1 and (b) O2 vacancies, plotted by VESTA program [41].

Various defect sites can be present in octahedron, i.e. top-to-top site (O1) or in-plane site (O2). These defects are shown in Figure 6.6a as top-to-top and Figure 6.6b as in-plane sites of oxygen vacancies. If oxygen is cation which attracts Ti anions and O1 vacancy (Figure 6.6a) is formed then the repulsion between Ti-Ti atoms is created due to like charges. This means that highly localized oxygen vacancies can change the charge configuration similar to $SrTiO_3$ [148]. As a result, charges are shifted and ionic bonds dominate, thus generating electric dipoles. This is interpreted as the elongation of lattice parameter c which occurs due to slight straightening of bond angles. Similar phenomenon can happen if O2 vacancy is formed (Figure 6.6b). In such a case, the elongation of lattice parameter c occurs again, as slight straightening of bond angles is expected. This implies that regardless of oxygen vacancy site, the maximum impact is developed in lattice parameter c . It also explains the reason of maximum lattice distortion observed in lattice parameter c as discussed before.

The strengthening of bond angles caused by oxygen vacancy and lattice distortions in crystal structure of FAST sintered $CaTiO_3$ is further examined. Rietveld refined parameters at 0° and 90° azimuthal sectors are extracted (when EEF was perpendicular to incident X-ray beam). This data is then plotted, i.e. individual unit cell model, in VESTA program [41], and compared. Additionally, the impact of SF or EEF on its bond angles and lengths is also determined, as presented in Table 6.3. It is noticed that without EEF (0 kV/cm), average bond angle O1-O1-O1 connected in-between Ti atom at 0° azimuthal sector is slightly decreased (156.757 ± 0.001) relative to 90° (156.773 ± 0.002). There can be two possible reasons. Firstly, during sintering, oxygen vacancies preferred to reside in perpendicular direction of SF which are 90° or 270° azimuthal sectors, causing elongation of lattice parameter c in perpendicular SF direction. Secondly, while current also flew inside the material due to sintering current pulses, electrons might have trapped at sites of oxygen vacancies and caused compression of

lattice parameter c in parallel SF direction. Furthermore, when EEF (+13 kV/cm) was applied, the average bond angle O1-O1-O1 at 0° azimuthal sector decreased further (156.753 ± 0.001). Whereas, the average bond angle O1-O1-O1 is slightly increased (156.778 ± 0.002) at 90° azimuthal sector. This gives the impression that upon applying EEF, electric dipoles aligned further in the same direction of their alignment during FAST sintering. This leads to the further elongation of lattice parameter c at 90° azimuthal sector (when EEF was perpendicular to diffracted X-rays). Additionally, at 0° azimuthal sector, if some of the electrons were trapped in holes due to FAST sintering current, they could have attracted Ti cations to some degree resulting in a slight bending (decrease) of bond angles. This process causes compression in lattice parameter c (when EEF was parallel to diffracted X-rays) and leads to the alignment of electric dipoles in same direction. This effect is observed in Figure 6.5b which supports the previous explanation.

EEF or SF	φ	0 kV/cm		+13 kV/cm	
		O1-O1-O1 [$^\circ$]	O1-O1 [\AA]	O1-O1-O1 [$^\circ$]	O1-O1 [\AA]
//	0°	156.757 ± 0.001	3.9022 ± 0.0001	156.753 ± 0.001	3.9020 ± 0.0001
\perp	90°	156.773 ± 0.002	3.9051 ± 0.0002	156.778 ± 0.002	3.9055 ± 0.0002
		O2-O2 [\AA] (1^{st})	O2-O2 [\AA] (2^{nd})	O2-O2 [\AA] (1^{st})	O2-O2 [\AA] (2^{nd})
//	0°	3.9146 ± 0.0001	3.9177 ± 0.0001	3.9148 ± 0.0002	3.9181 ± 0.0002
\perp	90°	3.9140 ± 0.0002	3.9176 ± 0.0002	3.9142 ± 0.0002	3.9180 ± 0.0002
		O2-Ti-O2 [$^\circ$] (1^{st})	O2-Ti-O2 [$^\circ$] (2^{nd})	O2-Ti-O2 [$^\circ$] (1^{st})	O2-Ti-O2 [$^\circ$] (2^{nd})
//	0°	89.285 ± 0.001	90.715 ± 0.001	89.277 ± 0.002	90.723 ± 0.002
\perp	90°	89.261 ± 0.002	90.740 ± 0.002	89.256 ± 0.002	90.744 ± 0.002

Table 6.3: Bond angles (O1-O1-O1 and O2-Ti-O2) and bond lengths (O1-O1 and O2-O2) are presented with EEF in parallel or perpendicular to azimuthal sector (when incident X-ray beam was perpendicular to SF/EEF).

Another interesting finding is uneven bond lengths of O2-O2 atoms which are perpendicular (lattice parameters a and b) to lattice parameter c . It has been found that the O2-O2 bond lengths in both planes, i.e. O2-O2 length in one direction (1^{st} bond length) and O2-O2 (2^{nd} bond length) in other direction, are exactly same (3.9140 \AA) according to the literature [40]. On the contrary, FAST sintered $CaTiO_3$ has different O2-O2 bond lengths in both directions as presented in Table 6.3. This finding also supports the theory of off centering of Ti atom. At the end, bond angles between O2-Ti-O2 are analyzed and significant change in these bond angles at 0° and 90° azimuthal sectors are also noticed. These bond angle differences between 1^{st} O2-Ti-O2 and 2^{nd} O2-Ti-O2 (Table 6.3) decrease when EEF was applied as compared to bond angles which are without EEF. These changes in both angles are the result of the changes observed in lattice parameters a and b (discussed in previous section). The bond angles (O2-Ti-O2) and bond lengths (O2-O2) of $CaTiO_3$ shown in Table 6.3 can be understood with the help of Figure 6.7, which presents the 3D visualization of unit cell model of $CaTiO_3$ plotted in VESTA program [41].

In real system of polycrystalline materials, high amount of crystalline-crystalline-interfaces is formed due to grain boundaries described as a rigid amorphous fraction. This rigid amorphous fraction links two different crystals. The covalent bonded oxygen inside this

rigid amorphous fraction is called bridging oxygen and this oxygen has the weakest point and hence highest possibility of forming oxygen vacancy [53]. This third type of oxygen vacancy is also highly localized because it is placed inside the interface (close to lattice distortions). If this bridging oxygen is O1 which is top-to-top axis of a titania octahedron, then a periodic alignment along the grain boundary is possible. However, these lattice oxygen vacancies and Ti^{+3} or Ca^{+1} sites as well as hole trapping sites localized at interfaces are hardly observable.

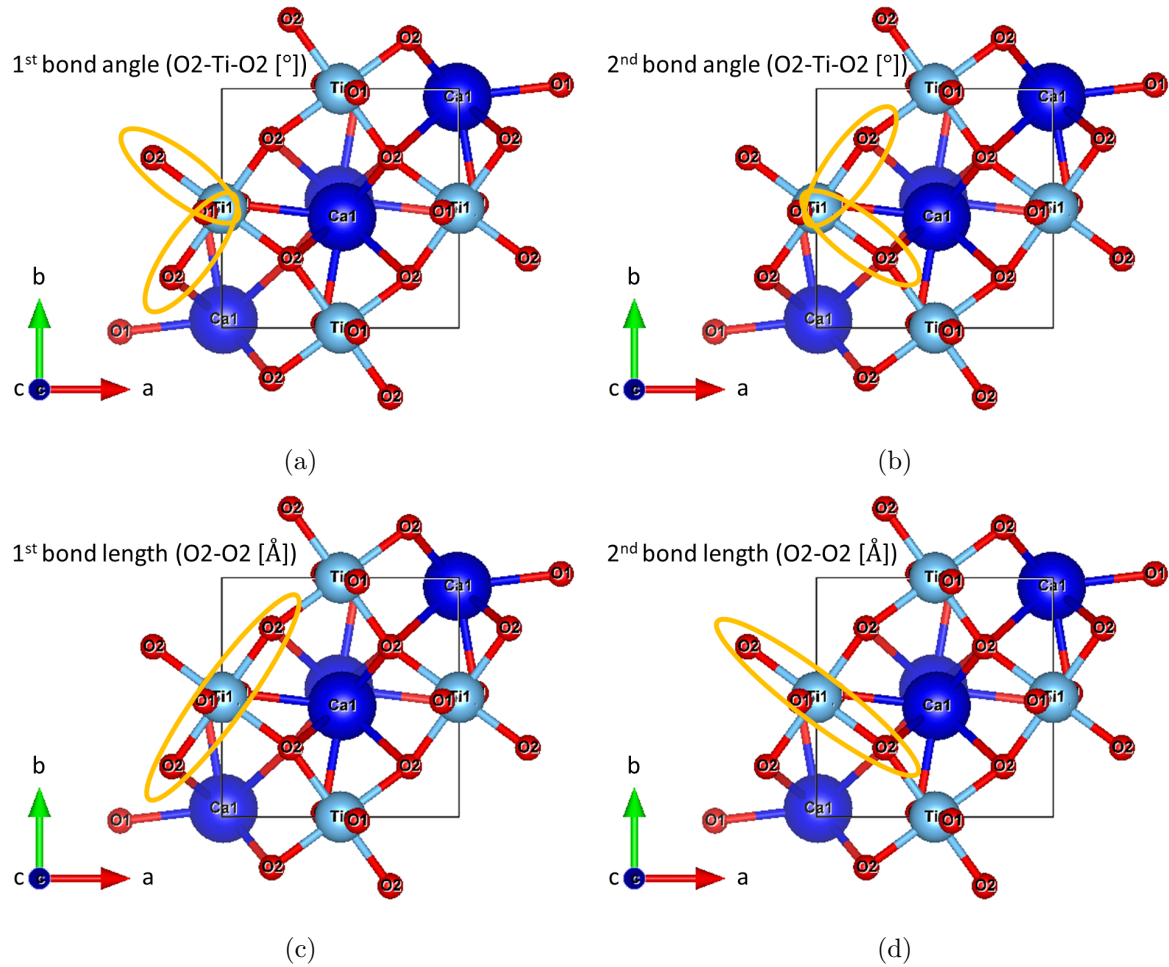


Figure 6.7: (a) 1st and (b) 2nd O2-Ti-O2 bond angles as well as (c) 1st and (d) 2nd O2-O2 bond lengths in $CaTiO_3$, covered with orange colour are presented.

In addition to 3D visualization, diffraction pattern of virgin FAST sintered sample is also examined in detail and all reflections are analyzed individually. Figure 6.8 presents three individual peaks of larger diffraction pattern at 0° , 45° and 90° azimuthal sectors (parallel as well as perpendicular SF direction to incident X-ray beam). The corresponding Miller indices are also shown. It is found that some of the reflections of FAST sintered $CaTiO_3$ shift as a function of azimuthal sectors when SF was perpendicular to incident X-ray beam. No shift on any other peaks is observed. Additionally, SF in parallel direction to incident X-ray beam does not show any shift of the peaks which means that they exactly overlap each other. This indicates that only those peaks shift which have (020), (022) and (024) as well as (200), (202) and (204) planes. It is possible that these planes are referred to as the motion of domain walls which cause the

polarization reorientation in the material [145]. Hence, these defects can also play an important role in the polarization reorientation in $CaTiO_3$.

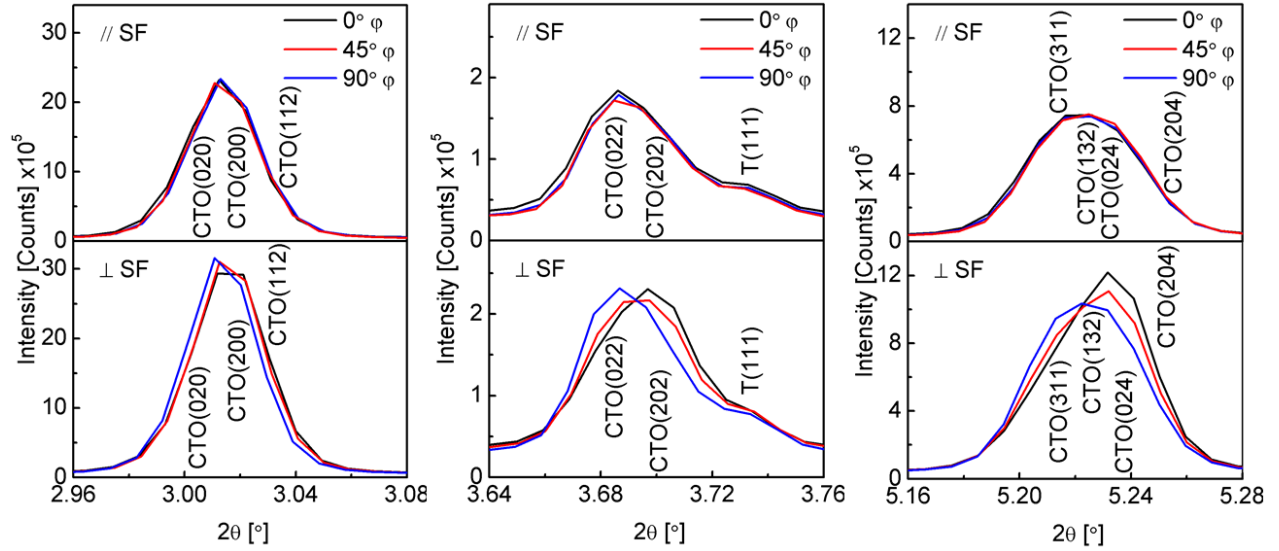


Figure 6.8: HEXRD patterns at three different azimuthal sectors (without EEF) when incident X-ray beam was in parallel and perpendicular direction to SF. The reflections of FAST sintered $CaTiO_3$ and α - TiO_2 are labelled by corresponding Miller indices ($CaTiO_3$ - CTO and α - TiO_2 - T).

It is well known that Miller indices (hkl) are the planes that intercept the three points a/h , b/k and c/l . This represents that Miller indices are inversely proportional to the intercepts of planes as vector quantities. It means that the planes do not intersect the axis if any of the indices is zero. Moreover, h, k and l Miller indices directions correspond to the directions along lattice parameters a, b and c, respectively [149]. According to this fact, two types of shifted planes are observed in FAST sintered $CaTiO_3$. Firstly, when there is no intercept at all with axis in lattice parameter a, it leads h to zero, k unchanged ($k = 2$) and change only in l, i.e. (020), (022) and (024). Secondly, when there is no intercept at all with axis in lattice parameter b, it leads k to zero and h unchanged ($h = 2$) but change in l occurs, i.e. (200), (202) and (204). This implies that intercept of planes with axis along lattice parameter c direction is mainly responsible for shifting of the presented peaks. It can be interpreted that O1, O2 and Ti atoms are displaced mainly along the lattice parameter c by forming four unequal Ti-O2 and two unequal Ti-O1 bond distances. This unequal distance of bonds generates electric dipole moments by the displacements of cations and anions from their equilibrium positions in the opposite direction. This finding supports the previous results, i.e. lattice parameter c is mainly responsible for pseudo piezoelectric behaviour. Similar findings are also reported, i.e. in tetragonal perovskite, structural distortion is relaxed only by the degree of freedom along the lattice parameter c and is an important factor in the mechanism of physical properties, mainly ferroelectricity [150]. However, in tetragonal perovskite structure, four equal Ti-O2 and two unequal Ti-O1 bonds are formed because the lattice parameter a and b are equidistant in tetragonal structure.

3D visualization of unit cells of $CaTiO_3$ with lattice planes shown in green color (020), (022), (024) and (200), (202), (204) are produced by VESTA program [41] and are presented in Figures 6.9a and 6.9b, respectively. Figure 6.9a shows the lattice planes

with no intercept at all with axis in the direction of lattice parameter a and Figure 6.9b shows the lattice planes with no intercept with axis in the direction of lattice parameter b.

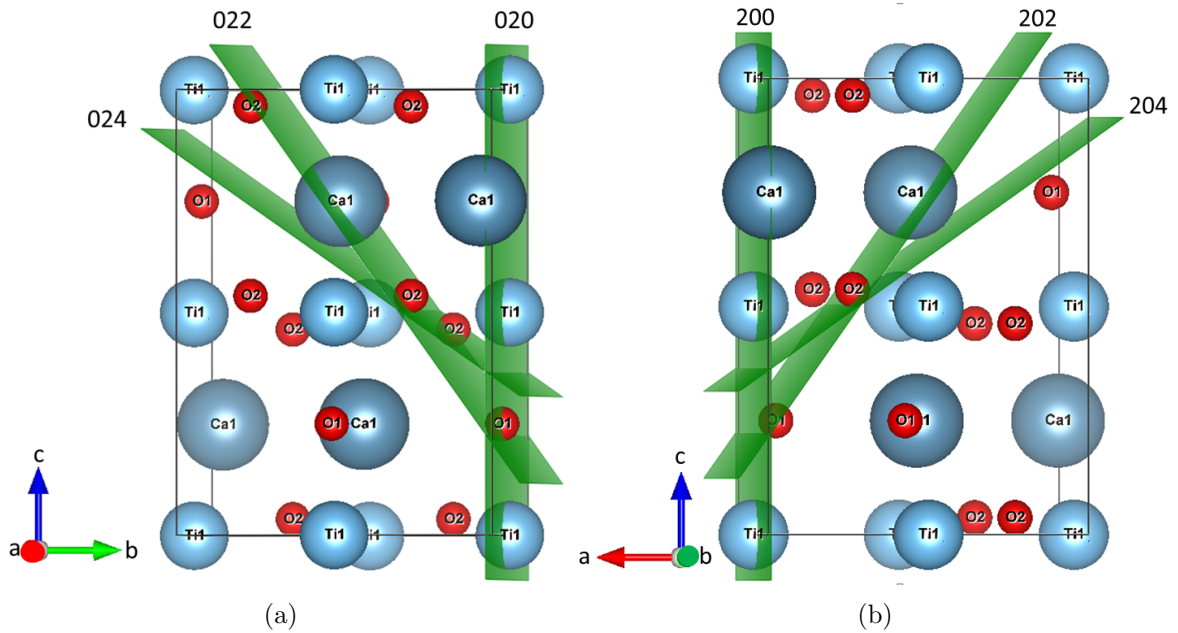


Figure 6.9: 3D visualization of unit cell of $CaTiO_3$ with (a) (020), (022), (024) and (b) (200), (202), (204) lattice planes.

6.7 Texture evolution

In polycrystalline materials unlike single crystals, atoms are randomly oriented due to grain boundaries. Whereas, some preferred orientations are possible which influence the intrinsic property of anisotropy [151]. The integrated intensity of a reflection peak from diffraction pattern is directly associated to the number of crystallites aligned with the direction of scattering of X-rays [152]. Additionally, preferred orientation among the grains in diffraction volume is manifestation of the non-uniform distribution of intensity along azimuthal angle of Debye-Scherrer cone. Therefore, the integration at different azimuthal sectors also gives information about the amount of crystallites oriented in the sample orientation space [63], [146]. Strictly speaking, the whole orientation distribution function (ODF) can be obtained which is generally given as multiples of random distribution (MRD), regarding the non-oriented state.

In this work, pole figures of virgin FAST sintered sample are presented when SF was perpendicular to incident X-ray beam. Figure 6.10 shows (002), (020) and (200) planes at 0° , 45° and 90° azimuthal sectors. MRD scale of these pole figures (before plotting) was kept same for comparison. Larger value of MRD indicates a high degree of orientation. At 0° and 45° azimuthal sectors, a small increase in MRD can be seen in all planes from 1 to almost 1.3 MRD. This indicate a very small amount of preferential orientation distribution at these azimuthal sectors. Whereas, MRD increases significantly (especially in 002 plane) and the texture can be seen at 90° azimuthal sector due to some preferred orientations likely caused by SF. This suggests that $CaTiO_3$ was most probably partially

poled during FAST sintering because unpoled sample shows random distribution of domains and as a consequence no notable texture should be seen [153]. It is also reported that sintering contributes significantly in the grain orientation and also assists the creation of texture [154].

To summarize, maximum orientation of lattice planes is at 90° azimuthal sector which is perpendicular to SF direction. In other words, preferred orientation in lattice planes (002), (020) and (200) of 90° azimuthal sector is 90° away from the lattice planes of sample in azimuthal direction which is 0° azimuthal sector (parallel to SF). It has been reported that large stresses in the material result in the generation of a large number of defects in the grains leading to textured ceramics [155]. Accordingly, it can be suggested that maximum defects in the grains are generated at 90° azimuthal sector (perpendicular direction of SF) during FAST sintering which supports the previous explanations.

It is important to mention that in general, the electric dipole orientation distribution function can be described as the probability of non- 180° domains reorientation events [145]:

$$f_{non-180^\circ} = 3 \frac{\frac{I_{002}}{I'_{002}}}{\frac{I_{002}}{I'_{002}} + 2 \frac{I_{200}}{I'_{200}}} \quad (6.7)$$

where I_{00h} and I'_{00h} are the integrated intensities of $00h$ reflection for electrically poled and randomly oriented states of tetragonal materials.

However, the data cannot be analyzed further as an electric dipole orientation distribution function because of three reasons. Firstly, Equation 6.7 is only valid for tetragonal materials and the FAST sintered $CaTiO_3$ has an orthorhombic crystal structure. Secondly, the plane reflections are too close to each other in $CaTiO_3$ that they superimpose and it is not possible to separate them and analyze their individual contributions as a function of intensity. Thirdly, according to pole figures, it is more likely that $CaTiO_3$ is partially poled and there is no significant information available about the reflections for random orientated states which is required for further analysis.

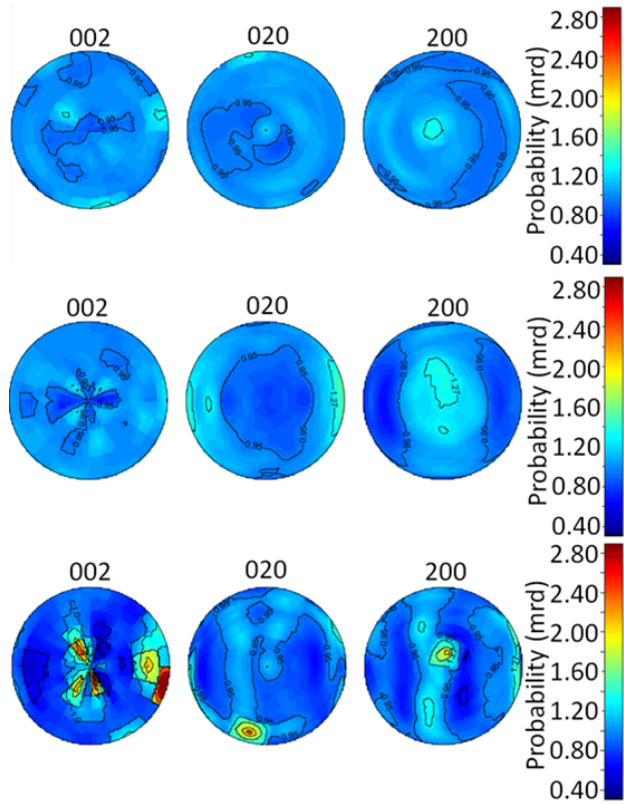


Figure 6.10: Pole figures of FAST sintered $CaTiO_3$ of (002), (020) and (200) planes at (top) 0° , (middle) 45° and (bottom) 90° azimuthal sectors (without EEF) when SF was perpendicular to incident X-ray beam.

6.8 Poling treatment

Poling treatment or its optimization strongly influences the piezoelectric constant values [156]. This is tested to study the possibility of further alignment of electric dipoles and optimize the piezoelectric constant values.

Figure 6.11 shows the poling treatment of virgin FAST sintered $CaTiO_3$ sample. The current is presented as (black color) current density and applied voltage (red color) as EEF. Initially, sample was heated at $100\text{ }^\circ\text{C}$ and kept constant. Then EEF of 10 kV/cm was applied for poling treatment. It can be seen that there is no flow of current when sample is heated

till $100\text{ }^\circ\text{C}$. This suggests that no change occurred in defective structure upon heating, i.e. no flow of charges. When EEF of 10 kV/cm is applied, a slight increase in current is observed till approximately 6 mA/cm^2 and EEF remains constant at 10 kV/cm . This can be associated to the alignment of electric dipoles. However, a breakdown just after approximately 13 seconds is observed with rapid increase in current. As a result, voltage drops which indicates the significant decrease in resistivity. After that, the sample remains in the same configuration showing the charge transport. This can be interpreted that minimum resistivity is reached due to the maximum defect formation in FAST sintered $CaTiO_3$ and these defective charges flow inside the material. It also shows that when EEF is applied for long period of time at elevated temperature, then after certain time it can overcome the enthalpy of motion for charge carriers leading to the diffusion of charges. This results in the opening of conducting channels instead of electric dipole alignment. Hence, poling treatment of FAST sintered $CaTiO_3$ is a challenging task.

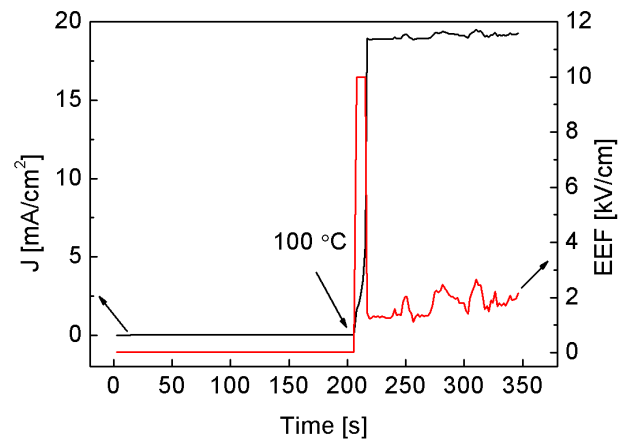


Figure 6.11: Poling treatment of FAST sintered $CaTiO_3$ at elevated temperature.

Chapter 7

Conclusion

$CaTiO_3$ powder was successfully prepared by sol-gel synthesis and densified using conventional and FAST sintering after calcination. The achieved relative densities of conventionally and FAST sintered $CaTiO_3$ were $(83.7 \pm 0.5)\%$ and $(91.2 \pm 0.4)\%$, respectively. After sol-gel synthesis, the phase transition from amorphous to polycrystalline $CaTiO_3$ was observed by performing DSC. It was noticed that $CaTiO_3$ orthorhombic (pbnm) phase was formed with the onset temperature of $(495 \pm 10) ^\circ C$. Therefore, powder was calcinated at $650 ^\circ C$ in air before densification.

HEXRD pattern of all samples revealed that orthorhombic (pbnm) phase of $CaTiO_3$ was obtained after calcination as well as after conventional and FAST sintering. It was found that a small amount of impurities like $\alpha-TiO_2$, $\gamma-TiO_2$ and CaO was present in calcinated powder. However, after conventional and FAST sintering, only $\alpha-TiO_2$ impurity was found. This happened because $\gamma-TiO_2$ and CaO formed $CaTiO_3$ phase upon heating during sintering. There was also a possibility that excess amount of $\gamma-TiO_2$ phase transformed to $\alpha-TiO_2$. Furthermore, the crystallite sizes of the $CaTiO_3$ were increased significantly from calcinated powder $d = (98 \pm 3)$ nm to FAST sintered $d = (200 \pm 1)$ nm due to recrystallization process during sintering. The conventionally sintered sample showed significantly larger crystallite size $d = (406 \pm 4)$ nm as compared to the FAST sintered sample which was the result of longer sintering time. The chemical composition determined by XPS and EDX spectroscopy stipulated that in calcinated powder, only calcium, titanium and oxygen with small amount of carbon was detected. Whereas, after FAST sintering, the additional peak of nitrogen was also observed by XPS. This showed that some of the oxygen vacancies were probably immediately replaced by nitrogen during FAST sintering. Moreover, atomic percent of elements in calcinated powder, conventionally and FAST sintered $CaTiO_3$ determined by EDX spectroscopy revealed that the oxygen contents slightly decreased after FAST sintering and slightly increased after conventional sintering as compared to calcinated powder. This indicates that even if oxygen vacancies (defects) were present in calcinated powder, they healed during conventional sintering in air causing relative increase in oxygen atomic percent. In contrast, FAST sintering in vacuum increased the amount of oxygen vacancies or defects causing relative decrease in the amount of oxygen atomic percent. XPS data also confirmed that lattice defects like oxygen vacancies, i.e. lattice distortions, were present in FAST sintered $CaTiO_3$ which were not observed in calcinated powder. These defects were mainly produced during the FAST sintering in vacuum. Additionally, Joule heating might also lead to the lattice distortions and

their distorted states (defects) were frozen due to the rapid heating and cooling rates in FAST sintering.

Additionally, the average grain sizes of conventionally (7.2 ± 0.3) μm and FAST sintered $CaTiO_3$ (2.5 ± 0.1) μm were estimated assuming a log normal distribution. This reveals that FAST sintered $CaTiO_3$ had smaller grain sizes as compared to conventionally sintered sample causing a larger amount of grain boundary areas due to fast heating and cooling rates. These grain boundary areas acted as pinning points as well as blocking positions for migrations and diffusion of defects.

The observation of oxygen vacancies, freezing of defects as well as relatively larger grain boundary areas in FAST sintered $CaTiO_3$ reveal that defects were highly localized and could be responsible for off-centering titanium leading to permanent electric dipoles. Hence, a piezoelectric response was generated which could only be observed in FAST sintered sample unlike conventionally sintered one. This effect was referred to as pseudo piezoelectricity, since its origin was a defective structure. The effect was measured by both direct and inverse piezoelectric methods. The charge produced and the average piezoelectric constant values were $Q = (2.7 \pm 0.5)$ pC and $d_{33} \sim 0.595$ pm/V , respectively. The obtained value of average piezoelectric constant of FAST sintered $CaTiO_3$ was very close to the ones of natural bone. These findings are promising for $CaTiO_3$ to be used as a bone implant material to improve osseointegration. However, if EEF is applied repeatedly or for a long period of time at elevated temperature, then defects can overcome the enthalpy of motion for charge carriers, thus leading to their diffusion and disappearance of piezoelectric behaviour.

Since, the observed pseudo piezoelectric behaviour was generated by structural changes (oxygen vacancies and defects). Therefore, the detailed analysis of structural changes under EEF as well as without EEF was also presented. It was shown that the lattice parameters a and c were significantly larger than the literature value but b was significantly smaller. Although, the lattice parameters of conventionally sintered $CaTiO_3$ were comparable to literature values. This showed that the defects in conventionally sintered sample were not present in significant amounts or they cured themselves during densification in air. However, significant difference of lattice parameters in FAST sintered sample from literature values indicated that oxygen vacancies and lattice distortions were present.

2D multiplots of HEXRD confirmed lattice distortions by producing zigzag pattern of diffraction peaks of FAST sintered $CaTiO_3$. This showed the shift of corresponding peak as a function of azimuthal sectors. It was found that maximum lattice strain was produced in lattice parameter c and lattice strain in a and b was influenced by c. Additionally, lattice strain in lattice parameters a and c was always produced in the same direction as a function of azimuthal sectors. However, lattice strain in lattice parameter b was always generated in opposite direction. It was also observed that the Debye-Scherrer rings were not circular but elliptical in shape and hence generated electric dipoles leading to the pseudo piezoelectric response of FAST sintered sample.

In-situ HEXRD also showed lattice distortions under EEF. The lattice parameter c under EEF compressed in parallel EEF (0° or 180° azimuthal sectors) direction and elongated in perpendicular EEF (90° or 270° azimuthal sectors) direction with respect to lattice parameter values without EEF. This suggests that if electric dipoles were slightly aligned during FAST sintering, then they would have aligned further due to high EEF which was applied in the SF direction. This led to more distortions in lattice

parameter c . Additionally, changes in lattice parameters a and b were instructed by c . It is worth mentioning that the expansion and compression of all lattice parameters were reversible. This response could only be observed in piezoelectric materials.

The change in diffraction intensities under EEF was also presented in FAST sintered $CaTiO_3$. Whereas, no change was observed in α - TiO_2 phase. This confirmed the existence of lattice distortions as well as non- 180° domains reorientation, which happened only in $CaTiO_3$ but not in α - TiO_2 phase.

It was shown by the visualization of 3D crystal structure that oxygen vacancies; top-to-top (O1) and in-plane (O2) sites, caused the increase in Ti-Ti atom distances located at lattice parameter c of FAST sintered sample. This led to the elongation of lattice parameter c due to slight straightening of bond angles as a result of repulsion of like charges which caused electric dipoles (without EEF). In addition, further elongation in lattice parameter c was caused under perpendicular EEF direction due to the alignment of electric dipoles. Whereas, further compression in lattice parameter c in parallel EEF direction was caused by the trapping of electrons at oxygen vacancies leading to the attraction of Ti atoms which slightly bent the bond. Another interesting finding was unequal bond lengths of O2-O2 atoms leading to the displacement of O1, O2 or Ti atoms. Apart from that, it was also shown that the planes with axis along lattice parameter c direction shifted in FAST sintered $CaTiO_3$ which could have also contributed to its pseudo piezoelectric behaviour.

It is worth mentioning that all the findings related to structural changes indicate that lattice parameter c is a primary agent for generating the pseudo piezoelectric effect in FAST sintered sample.

The texture evolution at 90° azimuthal sector suggested that preferred orientation occurred in perpendicular SF direction. It also revealed that the sample was moderately poled during FAST sintering. As a result, pseudo piezoelectric effect was observed without poling treatment.

Moreover, the investigated hardness and Young's modulus of FAST sintered $CaTiO_3$ were comparable with $CaTiO_3$ coated titanium implant. This opened the possibility of implanting pure $CaTiO_3$ without surface coating of titanium or its alloys.

Chapter 8

Outlook

It is suggested that pseudo piezoelectric behaviour of $CaTiO_3$ can trigger the remodelling and growth of bone. To verify this, further studies on in vitro and in vivo experiments are necessary. Since, these methods can be helpful to find proper treatments for bone osseointegration.

The optimization of piezoelectric constant in terms of better osseointegration is also a necessary step. However, poling treatment which is the simplest method of optimization is a challenging task in defective $CaTiO_3$ due to diffusion of lattice defects under strong EEF for a long period of time. Therefore, as an alternative, the piezoelectric constants can be tuned through cation substitution by doping with elements which exist in human body such as iron, magnesium and copper. Additionally, a single element, e.g. iron, can be used for doping with different amounts of concentration (1%...10%). These synthesis methods can be then compared with each other which will help to find out the most suitable piezoelectric constant that can trigger bone cells.

For the ongoing research in the direction of magnetic materials, Mößbauer spectroscopy measurements can play an important role to understand the environment of examined atom, i.e. iron, and also hyperfine interactions.

To further study the doped $CaTiO_3$ and its pseudo piezoelectric behaviour, in-situ HEXRD experiments as well as piezoelectric measurements can be performed. Moreover, its defective structure should also be studied and compared with pure $CaTiO_3$. Additionally, electron paramagnetic resonance spectroscopy can be used to determine the nature of the lattice defects of bulk samples, which will help to understand the lattice defects more deeply caused by unpaired electrons. However, the possibility of attaining permanent electric dipoles even after applying strong EEF repeatedly or for long period of time at elevated temperature by freezing the lattice defects (highly localized defects) is still open for research.

Stress shielding is a major problem resulting in the reduction of bone density that can lead to the fracture of bone even in minor stresses. It causes osteopenia which can be overcome by increasing the porosity of $CaTiO_3$ by optimizing the sintering conditions. Another possibility to overcome this problem can be FAST sintering of bulk layered porous material in which biocompatible pure titanium or its alloys can be sandwiched between bioactive $CaTiO_3$. As a result, porous titanium or its alloy's mechanical properties can be compared to natural bone which will overcome the problem of stress shielding as well as increase the osseointegration due to the pseudo piezoelectric behaviour of $CaTiO_3$.

Appendices

Appendix A

Azimuthal sector integration from 2D images and lattice parameters

2D image with azimuthal sectors and 1D diffraction pattern

An illustration of azimuthal sector integration as 2D image is presented in Figure A.1. All shown azimuthal sectors were integrated with five slices of 1° step. The same procedure was repeated for every measurement before applying EEF as well as after the application of EEF in both positive and negative directions.

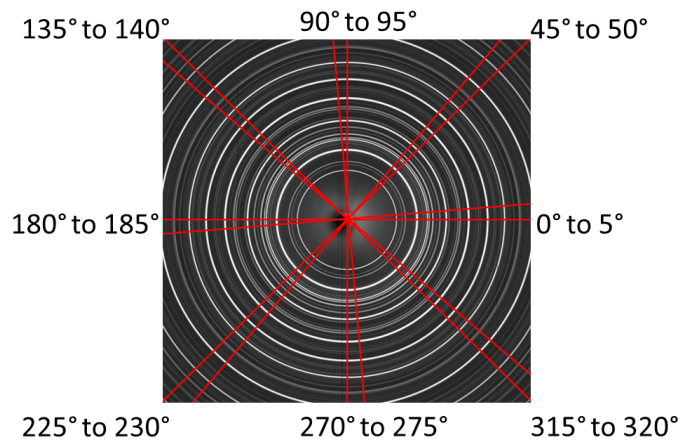


Figure A.1: Azimuthal integration of various sectors (red color) in 2D image for further data analysis.

Figure A.2 presents the exemplary 1D pattern versus 2θ with all integrated azimuthal sectors of FAST sintered sample deduced from 2D images. Figure A.2a shows diffraction patterns of virgin sample when incident X-ray beam was perpendicular to SF direction and Figure A.2b corresponds when parallel to SF direction (without any mechanical loading or EEF). Similar patterns are also plotted and analyzed which were measured with in-situ HEXRD, i.e. under EEF (applied in positive and negative directions).

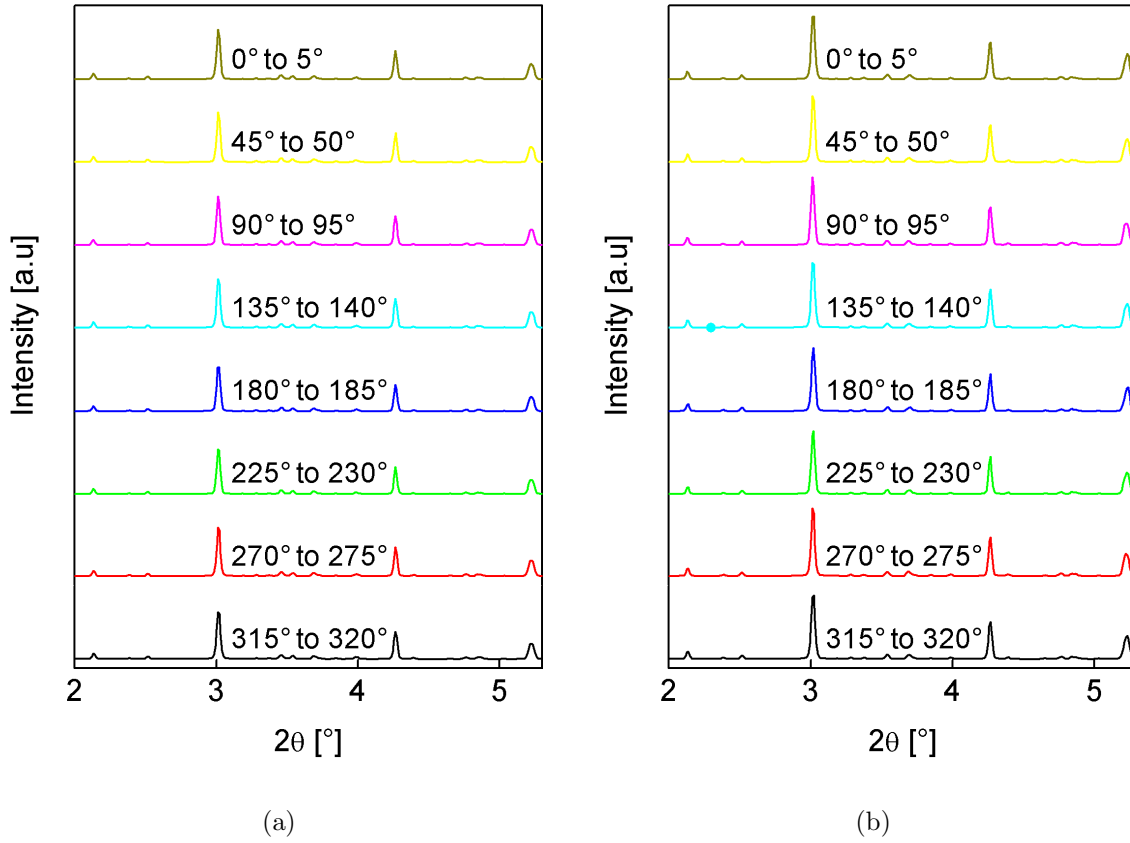


Figure A.2: Reduction of 2D images into 1D patterns of intensity versus 2θ of azimuthal sectors. Diffraction patterns are presented when SF direction were (a) parallel and (b) perpendicular to incident X-ray beam (without EEF).

Lattice parameters of samples, R_{wp} and R_{exp} values

Table A.1 presents the lattice parameters of calcinated powder, conventionally and FAST sintered $CaTiO_3$ as well as their R_{wp} and R_{exp} values from Rietveld refinement of single shot HEXRD experiment.

$CaTiO_3$	Lattice parameters [\AA]			R_{wp} [%]	R_{exp} [%]
	a	b	c		
Calcinated powder	5.3915 ± 0.0009	5.4384 ± 0.0008	7.6587 ± 0.0009	7.85	1.00
Conventionally sintered	5.3832 ± 0.0004	5.4396 ± 0.0007	7.6454 ± 0.0004	6.90	0.65
FAST sintered	5.3898 ± 0.0004	5.4338 ± 0.0004	7.6508 ± 0.0007	5.05	0.50

Table A.1: Lattice parameters of calcinated powder, conventionally and FAST sintered $CaTiO_3$ as well as R_{wp} and R_{exp} values from Rietveld refinement of single shot HEXRD experiment.

Appendix B

SEM, XPS and EDX spectroscopy

SEM images of samples

Figure B.1 shows exemplary SEM images of polished surfaces of conventionally and FAST sintered $CaTiO_3$. The grains in FAST sintered sample are spherical but in conventionally sintered sample have ambiguous shapes probably due to abnormal Ostwald ripening which also causes irregular elongation of grains. The average grain sizes of both samples were estimated assuming a log normal distribution. Additionally, the diameter of each grain of FAST sintered sample was calculated and for conventionally sintered sample, the lengths of irregular elongated grains were used to calculate the grain sizes.

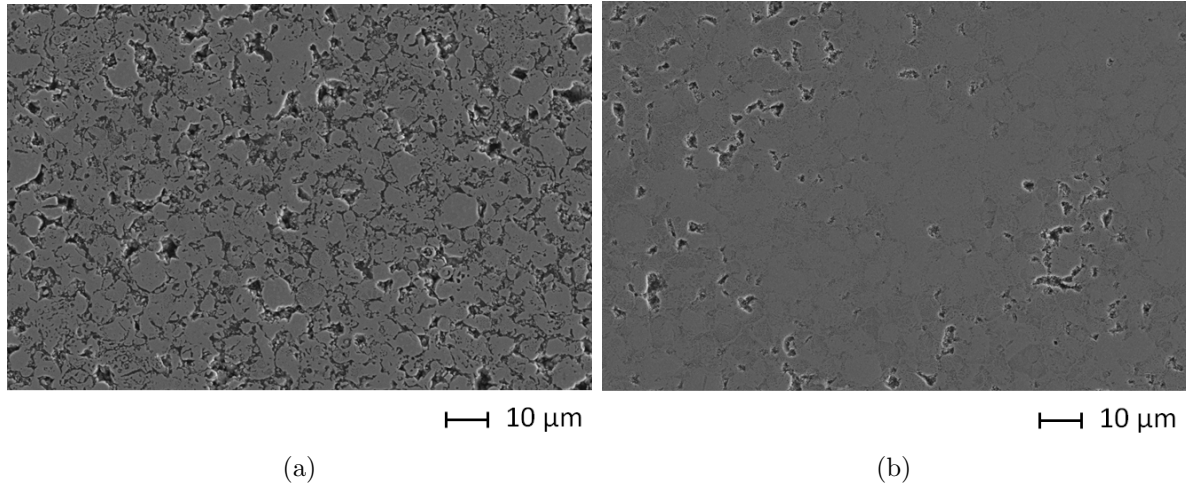


Figure B.1: Exemplary SEM images of (a) conventionally and (b) FAST sintered $CaTiO_3$.

EDX spectra of samples

Figure B.2 presents the EDX spectra of calcinated powder after cold pressed, conventionally and FAST sintered $CaTiO_3$ samples along with their SEM images and corresponding scanning areas. The spectra of all samples confirms the presence of calcium, titanium, oxygen and carbon. Whereas, no other impurity element is detectable.

It is important to mention that the measurement time for all samples was same, so the results can be compared. The oxygen peak of calcinated powder (Figure B.2a) is approximately 6.8 cps/eV which increases to 8.1 cps/eV (Figure B.2c) after the conventional sintering. However, the oxygen peak decreases to 5.8 cps/eV after FAST sintering (Figure B.2e). This can be interpreted that amount of oxygen increased in the sample after conventional sintering and decreased after FAST sintering. In other words, oxygen vacancies present in the calcinated powder cured themselves after conventional sintering in air. However, in FAST sintering oxygen vacancies increased due to vacuum environment.

Depth profile of elements

Figure B.3 presents the depth profiles of each element detected by XPS. First red areas (right side of the images) in Figures B.3a and B.3b are $Ti - 2p_{3/2}$ and $Ca - 2p_{3/2}$ peaks, respectively. Second red area (left side of the same images) are $Ti - 2p_{1/2}$ and $Ca - 2p_{1/2}$ peaks. Figure B.3c is the O-1s peak of oxygen element and the broadening of red area is due to the overlapping of two peaks with different binding energies. Figure B.3d is the depth profile of carbon contained in $CaTiO_3$ sample after FAST sintering. It can be seen that titanium, calcium and oxygen are detected till the maximum observed depth. However, carbon is present on the surface with the depth of approximately 14 nm only. This provides the proof that carbon was not completely diffused from the protective graphite foil which was used to prevent the powder reaction with graphite die during FAST sintering.

Normalized XPS peaks of elements

Figure B.4 shows the normalized XPS spectra of titanium ($Ti - 2p_{3/2}$ and $Ti - 2p_{1/2}$) and calcium ($Ca - 2p_{3/2}$ and $Ca - 2p_{1/2}$) of calcinated powder as well as FAST sintered $CaTiO_3$. All spectra were normalized before background subtraction. The peaks of FAST sintered samples of titanium and calcium show uneven broadening as compared to calcinated powder. The difference in energies of doublet separation of Ti-2p of calcinated powder and FAST sintered is also presented with the increased difference of approximately 0.11 eV in FAST sintered sample. Whereas, no measurable difference in energies of doublet separation of calcium is detected.

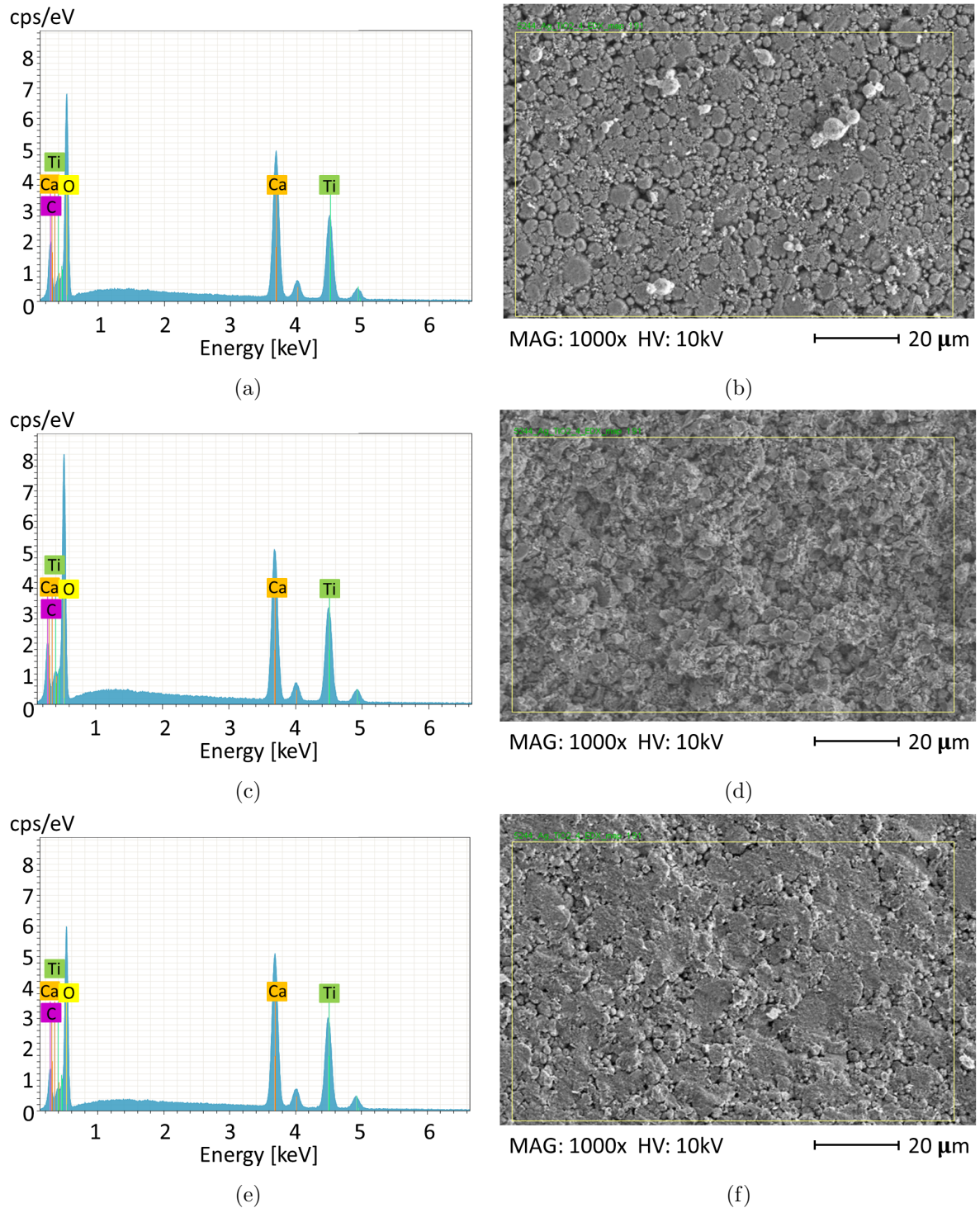
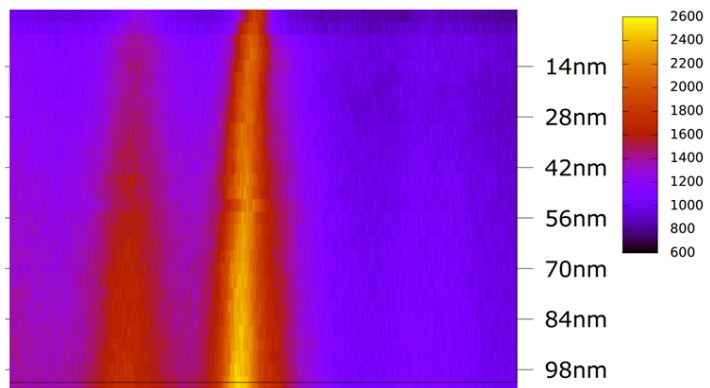
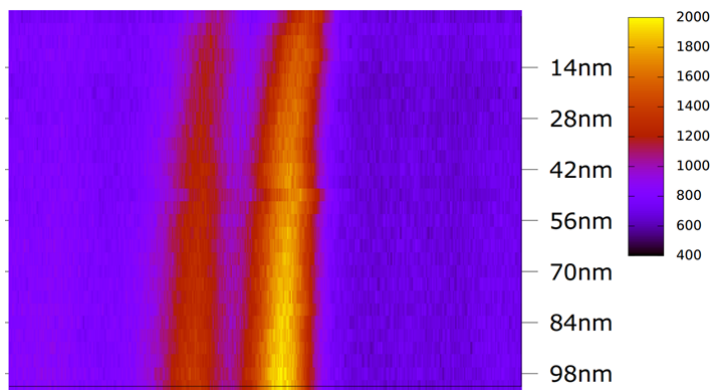


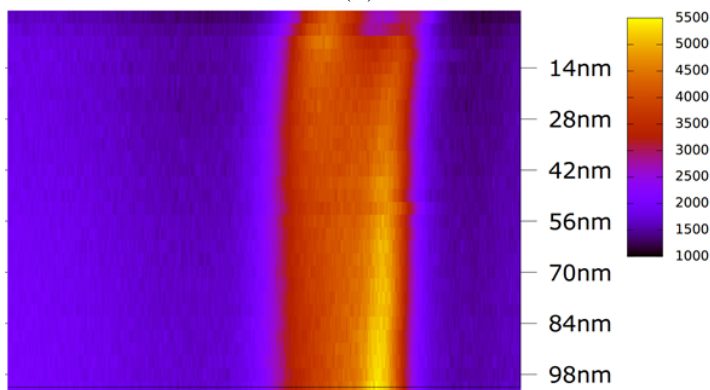
Figure B.2: EDX spectra of (a) calcinated powder, (c) conventionally and (e) FAST sintered as well as SEM images of the analyzed areas of (b) calcinated powder, (d) conventionally and (f) FAST sintered $CaTiO_3$ (without polishing of samples).



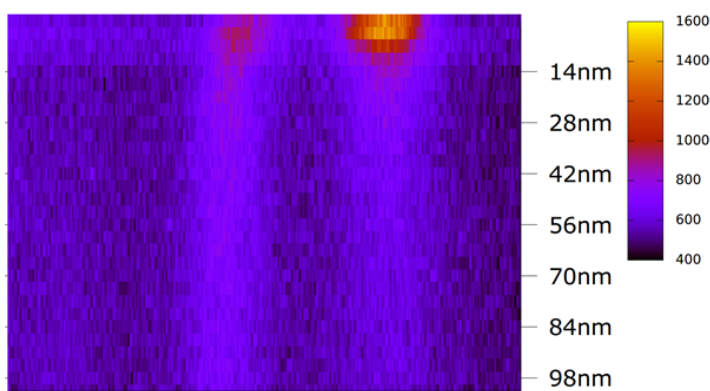
(a)



(b)



(c)



(d)

Figure B.3: Depth profiles of (a) titanium, (b) calcium, (c) oxygen and (d) carbon determined by XPS experiment.

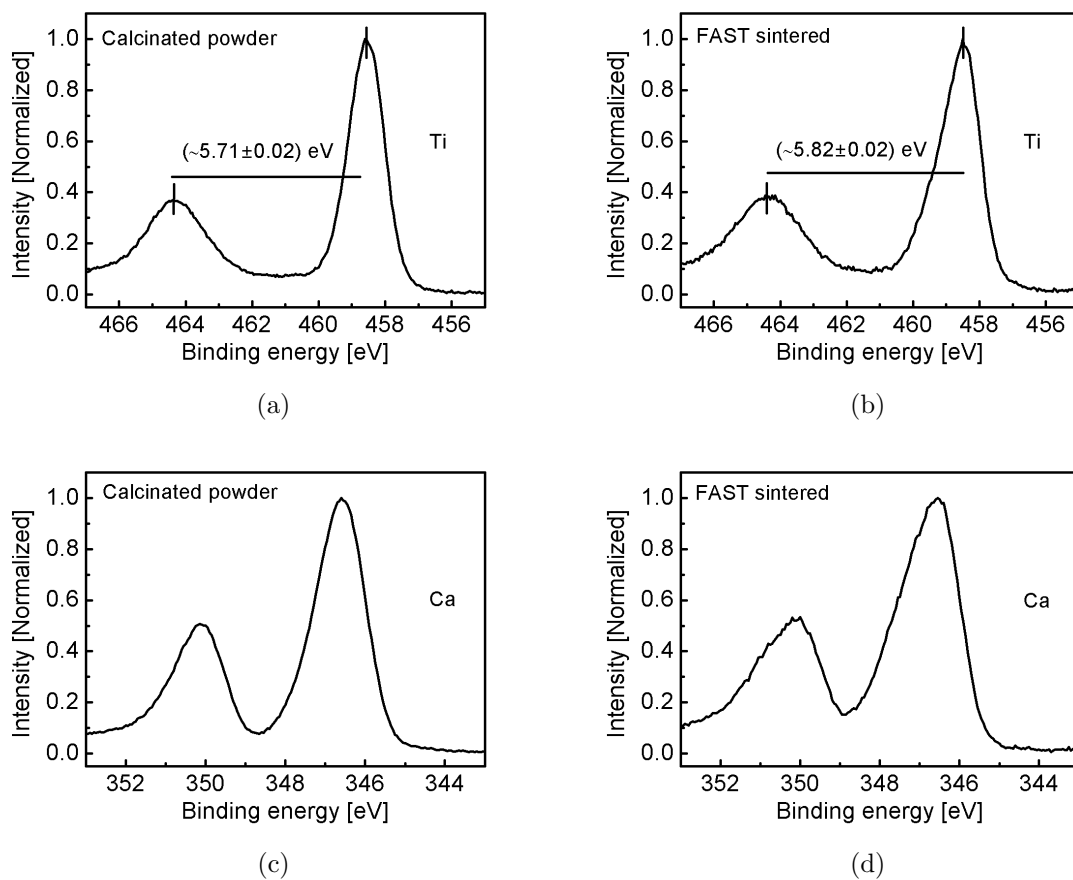


Figure B.4: Normalized XPS spectra of (a) Ti-2p, (c) Ca-2p peaks of calcinated powder and (b) Ti-2p, (d) Ca-2p peaks of FAST sintered $CaTiO_3$.

Appendix C

In-situ HEXRD

Diffraction patterns

Exemplary diffraction patterns of FAST sintered $CaTiO_3$ at 0° azimuthal sector and under EEF of +13 kV/cm are presented in Figure C.1. Dots represent the experimental data, red line represents the fitted data and blue line shows the difference between fitted and experimental data. Moreover, the corresponding Bragg positions of all contributed phases are shown. No additional peaks are observed as compared to virgin samples except silver phase in parallel direction (Figure C.1b). Silver phase was identified due to the silver electrodes applied on the sample. All other diffraction patterns, e.g. EEF of -13 kV/cm or all other integrated azimuthal sectors, shows similar diffraction patterns and the only change in lattice parameters is observed.

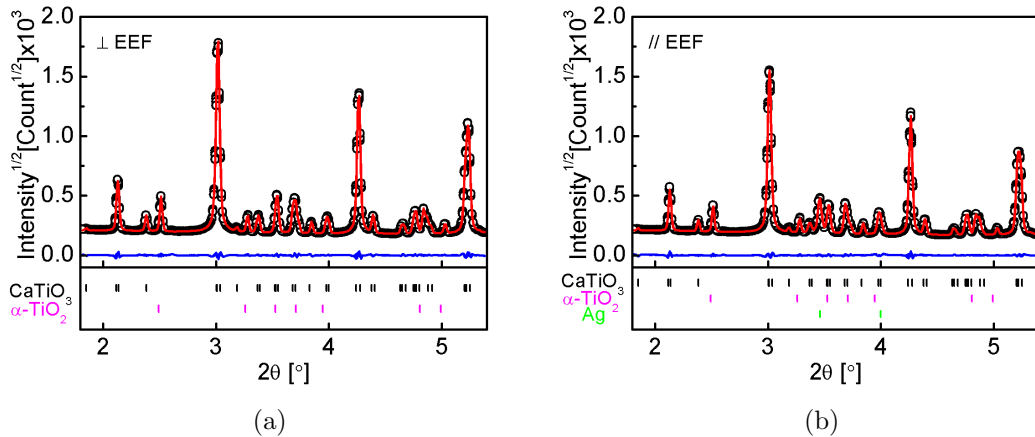


Figure C.1: Exemplary diffraction patterns of FAST sintered $CaTiO_3$ at 0° azimuthal sectors when incident X-ray beam was (a) perpendicular and (b) parallel to EEF direction. The experimental pattern (black dots) and fitted patterns (red solid line) are presented. Below each diffractogram the differential patterns (blue line) are presented. Furthermore, corresponding Bragg positions of all contributed phases are shown.

Distortions in lattice parameter

Figures C.2, C.3 and C.4 show the distortions in lattice parameters a , b and c of FAST sintered $CaTiO_3$ under EEF as a function of azimuthal sectors. The measurement procedure as well as all points shown in all the figures are explained in Chapter 4.

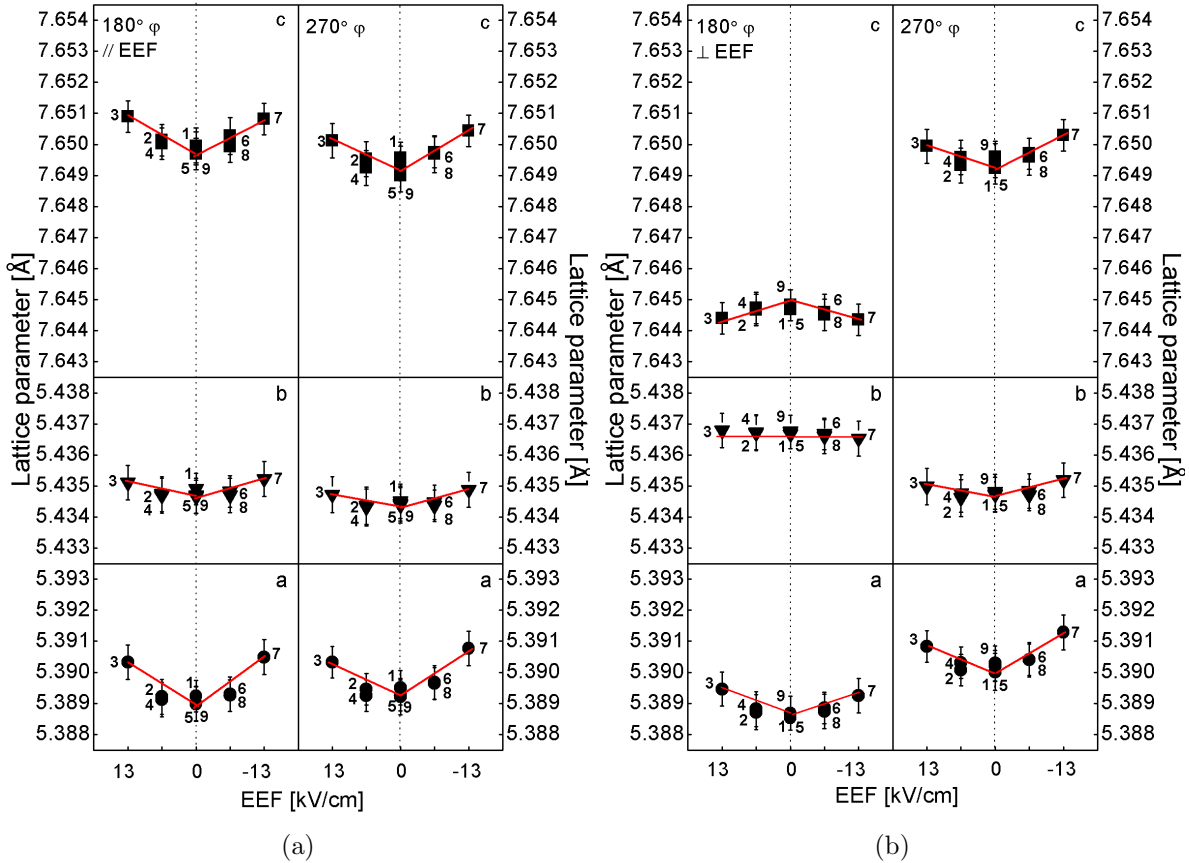


Figure C.2: Evolution of lattice parameters of FAST sintered $CaTiO_3$ at 180° and 270° azimuthal sectors under EEF. Presented data points are measured when incident X-ray beam was in (a) parallel and (b) perpendicular direction to EEF.

Figures C.2a and C.2b present the distortions in lattice parameters a , b and c at 180° and 270° azimuthal sectors, when incident X-ray beam was parallel and perpendicular to EEF direction, respectively. It can be seen in Figure C.2a that the lattice parameters do not shift from 180° to 270° azimuthal sector (without EEF). They only expand linearly under EEF. In Figure C.2b, there is a significant shift of lattice parameter c (point 1) from 180° to 270° azimuthal sector (without EEF). Additionally, lattice parameter c compresses linearly and a expands linearly under EEF. No change in lattice parameter b is observed under EEF, at 180° azimuthal sector. Whereas, all lattice parameters expand linearly under EEF at 270° azimuthal sector.

Figures C.3a and C.3b present the distortions in lattice parameters a , b and c at 45° and 135° azimuthal sectors, when incident X-ray beam was parallel and perpendicular to EEF direction, respectively. In Figure C.3a, the behaviour of all lattice parameters under EEF as well as initial positions (point 1) is similar to other azimuthal sectors. However, in Figure C.3b, it can be seen that the initial position (point 1) of lattice parameter c shifts due to lattice strain (without EEF) and is in-between the points 1 of

lattice parameter c in 180° and 270° or 0° and 90° azimuthal sectors. Whereas, minor differences in lattice parameters a and b at points 1 are most probably due to the lattice redistribution in crystal structure which is influenced by the strain in lattice parameter c . Additionally, lattice parameters a and c significantly as well as lattice parameter b slightly (in the range of errors) expand under EEF.

Figures C.4a and C.4b present the distortions in lattice parameters a , b and c at 225° and 315° azimuthal sectors, when incident X-ray beam was parallel and perpendicular to EEF direction, respectively. Lattice parameters in these figures show similar behaviour as noticed in Figures C.3a and C.3b.

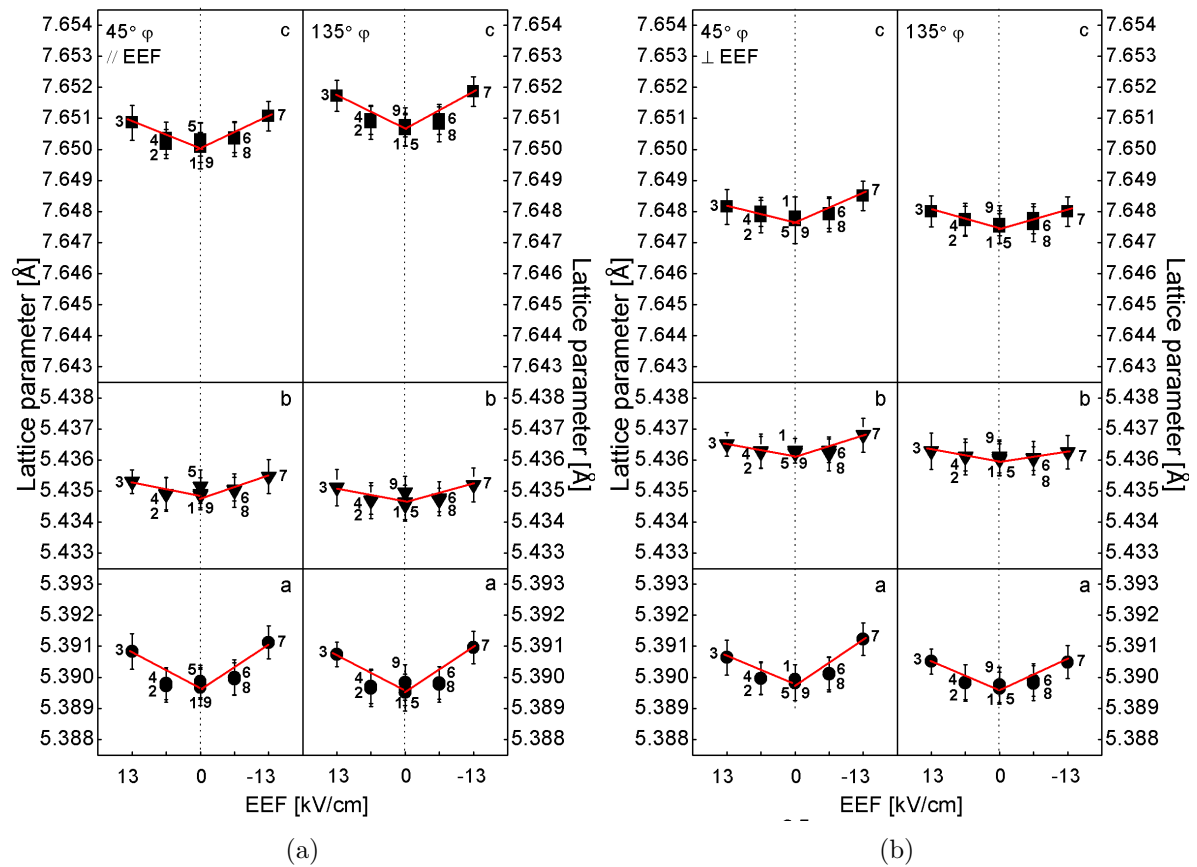


Figure C.3: Evolution of lattice parameters of FAST sintered $CaTiO_3$ at 45° and 135° azimuthal sectors under EEF. Presented data points are measured when incident X-ray beam was in (a) parallel and (b) perpendicular direction to EEF.

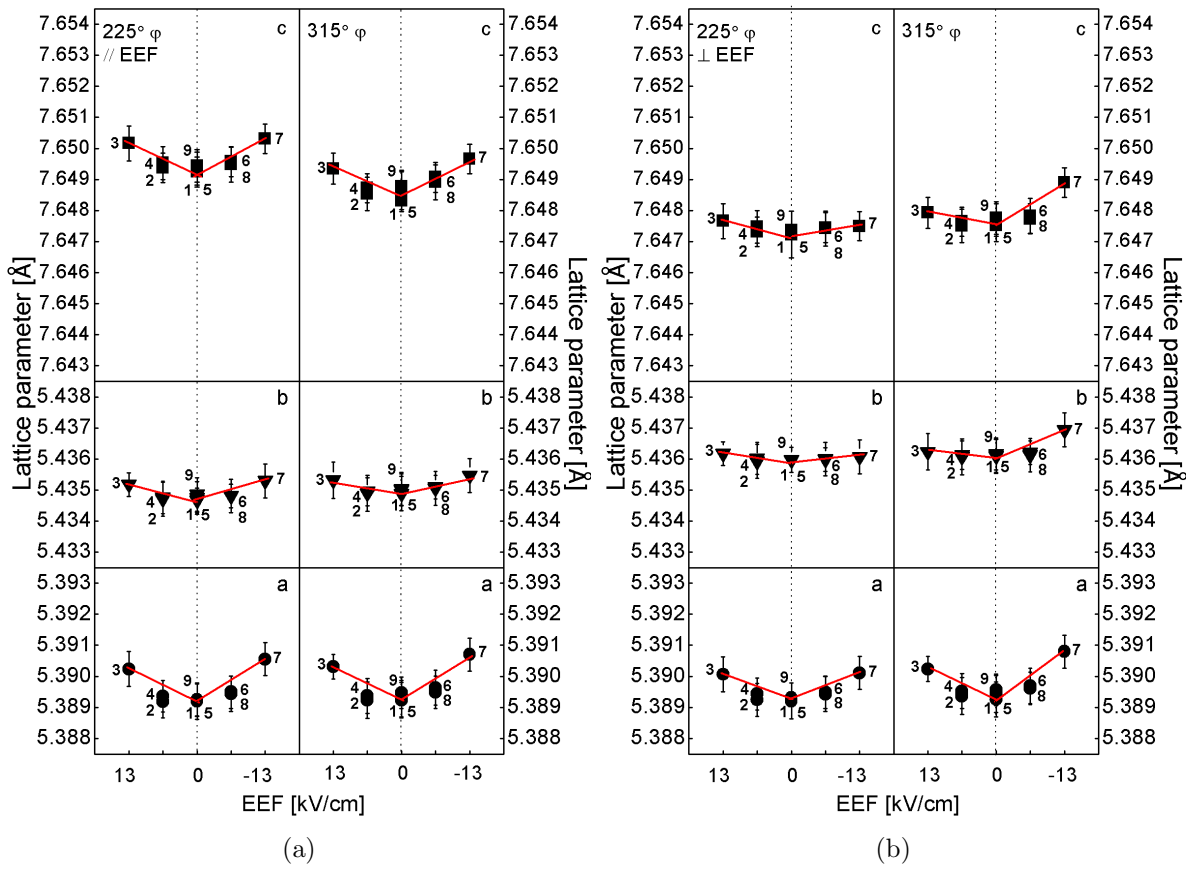


Figure C.4: Evolution of lattice parameters of FAST sintered $CaTiO_3$ at 225° and 315° azimuthal sectors under EEF. Presented data points are measured when incident X-ray beam was in (a) parallel and (b) perpendicular direction to EEF.

Non-180° domain wall motion

Figure C.5 shows the main peaks of FAST sintered $CaTiO_3$ at 0° azimuthal sector under EEF of ± 13 kV/cm as well as without EEF (a virgin sample). The increase in intensity of main peak compared to virgin sample is observed in both parallel and perpendicular direction of incident X-ray beam to EEF. This indicates the motion of non-180° domain walls with respect to both azimuthal sectors (mentioned in Chapter 6) as well as under EEF.

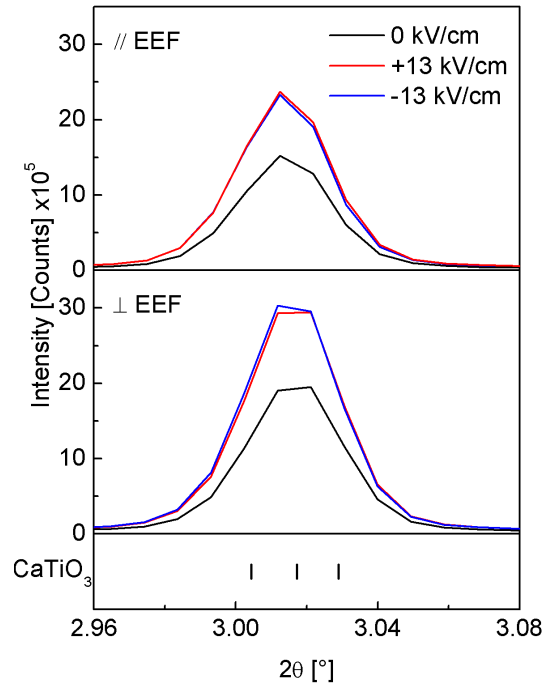


Figure C.5: Diffraction patterns of main peak of FAST sintered $CaTiO_3$ at 0° azimuthal sector, without EEF as well as under EEF applied in parallel and perpendicular direction to incident X-ray beam. Corresponding Bragg positions of $CaTiO_3$ are also presented.

Evolution of lattice strain

Figures C.6, C.7, C.8 and C.9 present the evolution of lattice strain in FAST sintered $CaTiO_3$ under EEF at different azimuthal sectors. It is assumed that red dotted line is the reference lattice parameter, without strain or zero lattice strain when no EEF was applied.

The lattice strain was calculated with the help of Equation 5.2, assuming that d is strain free lattice parameter and d_o is lattice parameter with strain. It can be seen that when EEF of ± 13 kV/cm is applied in parallel direction to incident X-ray beam, lattice strain is always produced in positive direction at each observed azimuthal sector. Furthermore, almost same magnitudes of lattice strain are generated in both negative and positive directions of EEF. This indicates that only expansion in crystal unit cell is observed. Contrary to the results of lattice strains produced when EEF was parallel

to incident X-ray beam, negative lattice strain in lattice parameter c is observed at 0° and 180° azimuthal sectors (Figures C.6b and C.8b). Additionally, no lattice strain is produced in lattice parameter b when lattice strain in c has negative value under EEF in perpendicular direction to incident X-ray beam. Whereas, lattice strain in a always remains positive. This suggests that when c compresses, a expands and b remains unchanged.

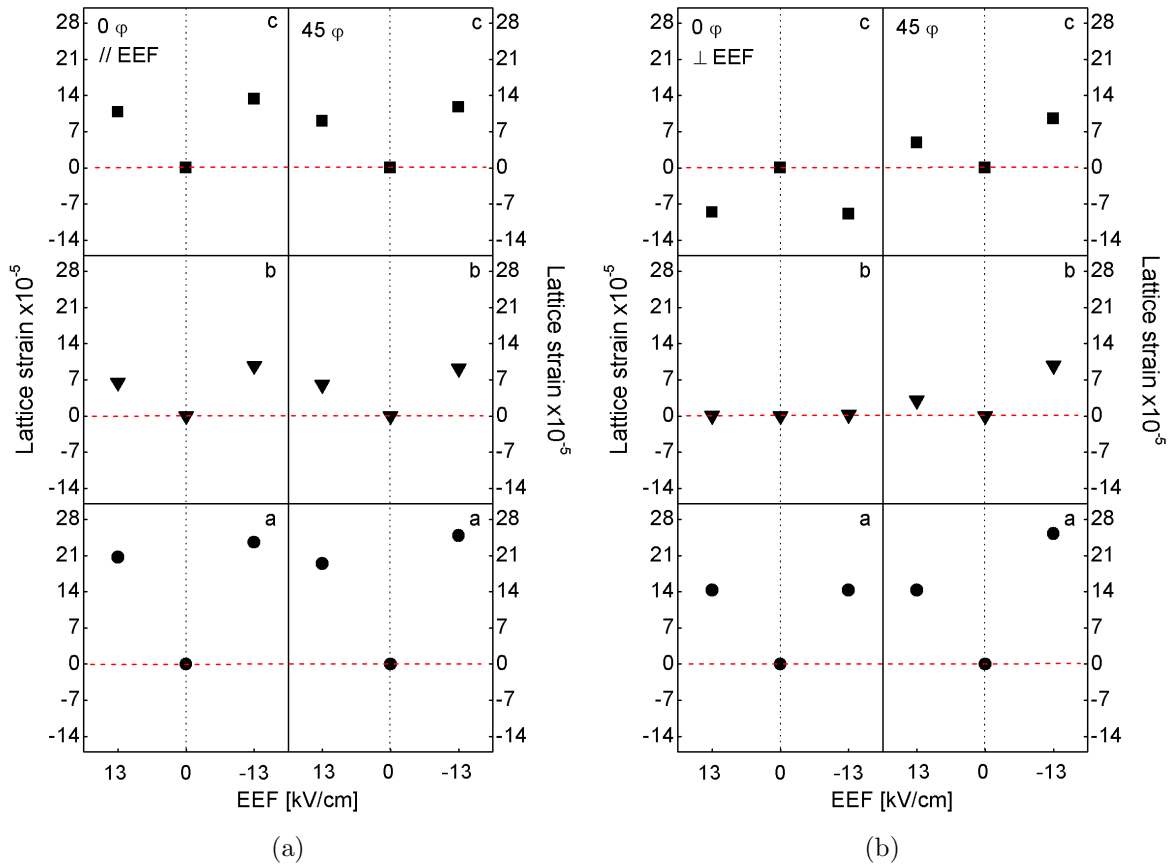


Figure C.6: Lattice strain at 0° and 45° azimuthal sectors vs EEF (incident X-ray beam in (a) parallel and (b) perpendicular direction to EEF).

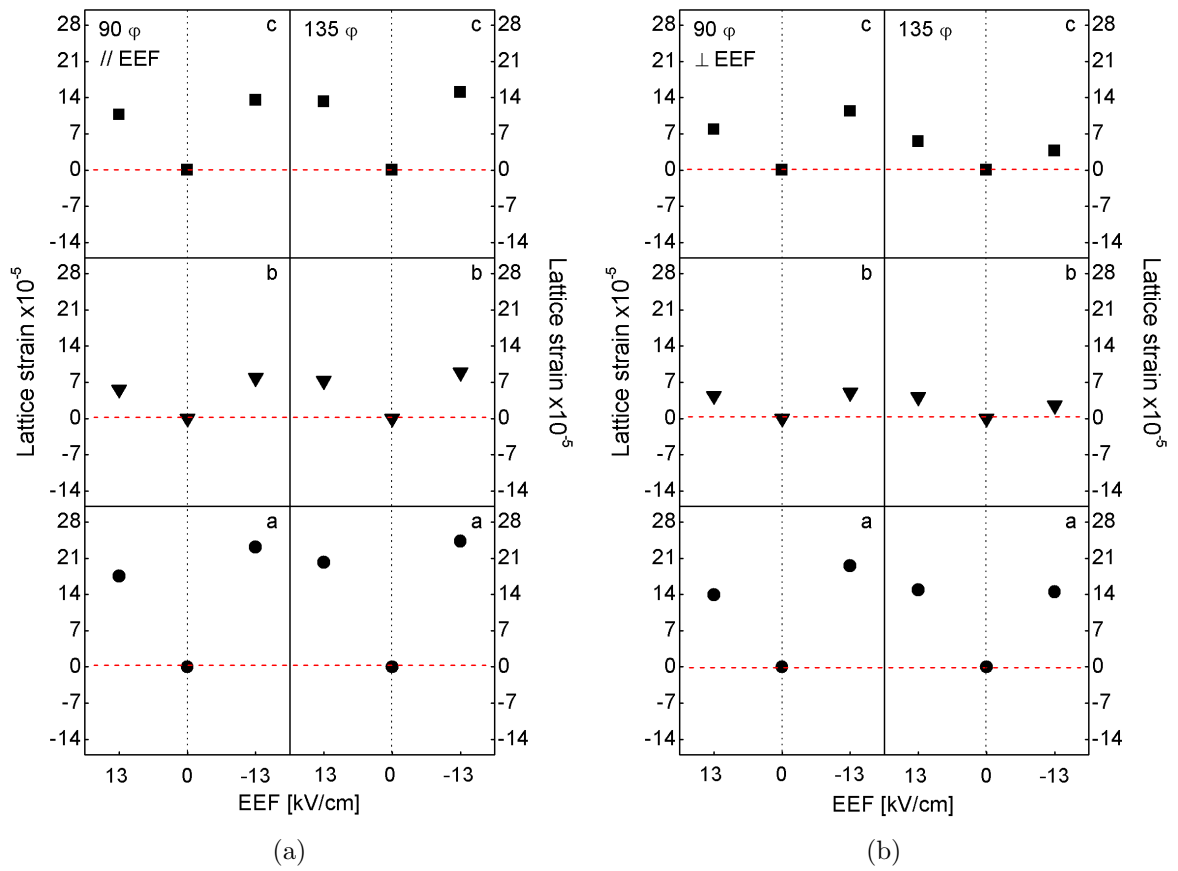


Figure C.7: Lattice strain at 90° and 135° azimuthal sectors vs EEF (incident X-ray beam in (a) parallel and (b) perpendicular direction to EEF).

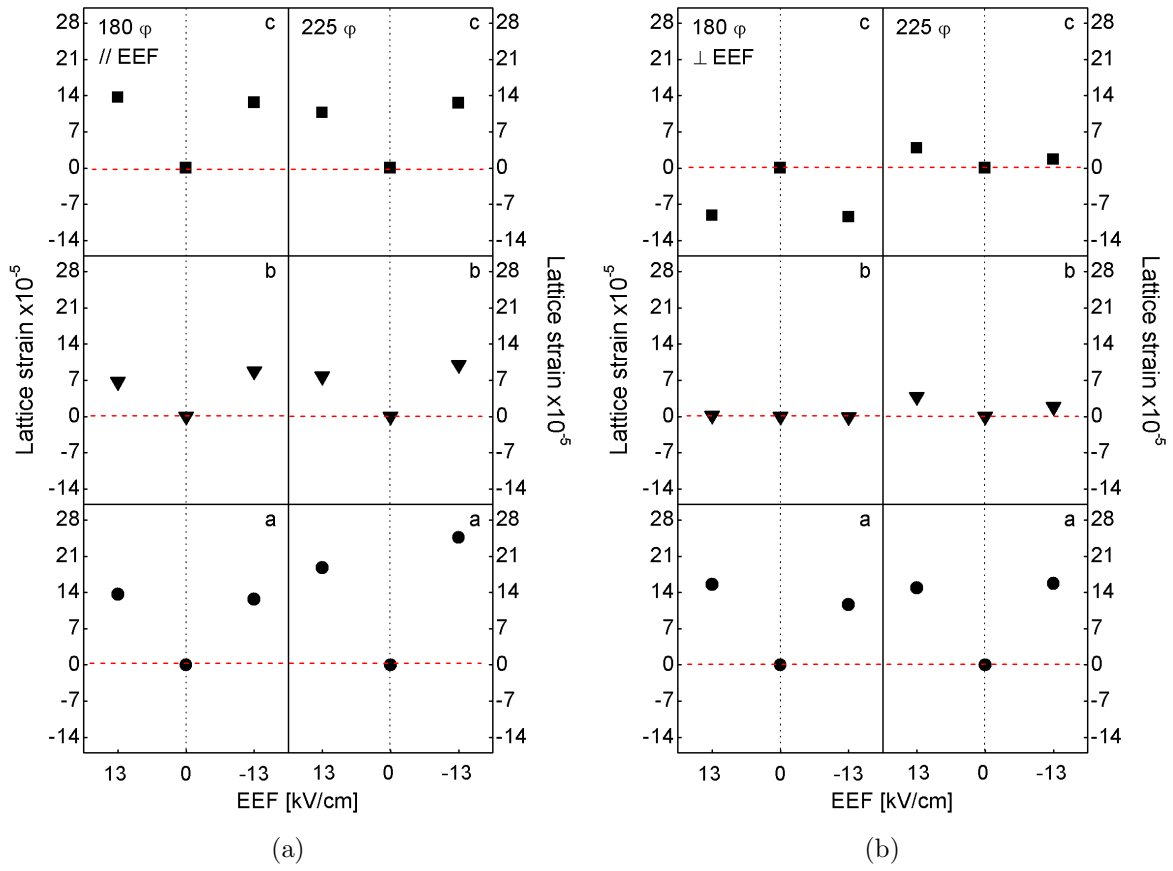


Figure C.8: Lattice strain at 180° and 225° azimuthal sectors vs EEF (incident X-ray beam in (a) parallel and (b) perpendicular direction to EEF).

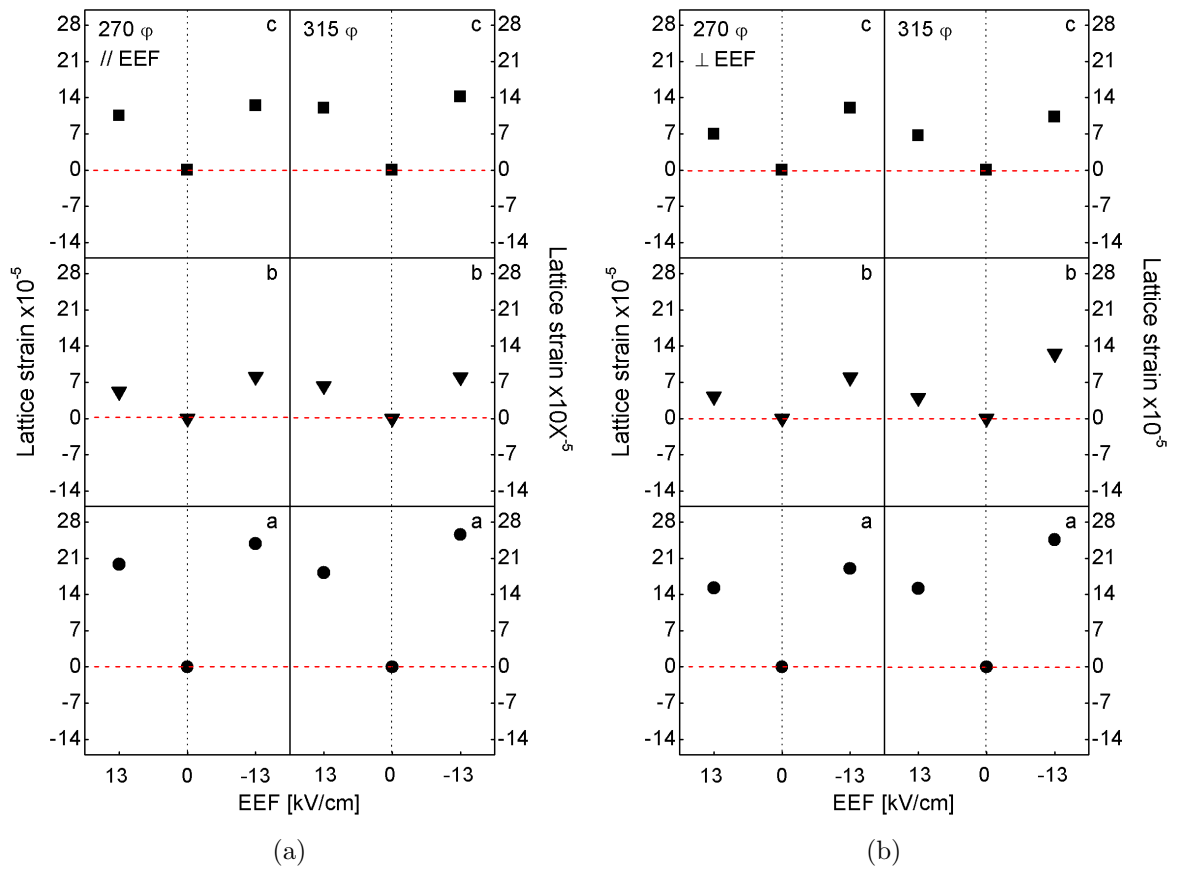


Figure C.9: Lattice strain at 270° and 315° azimuthal sectors vs EEF (incident X-ray beam in (a) parallel and (b) perpendicular direction to EEF).

Appendix D

Nanoindentation

Figure D.1 presents the nanoindentation depth versus loading and unloading curves of FAST sintered $CaTiO_3$ with applied loads of 10, 20 and 30 mN.

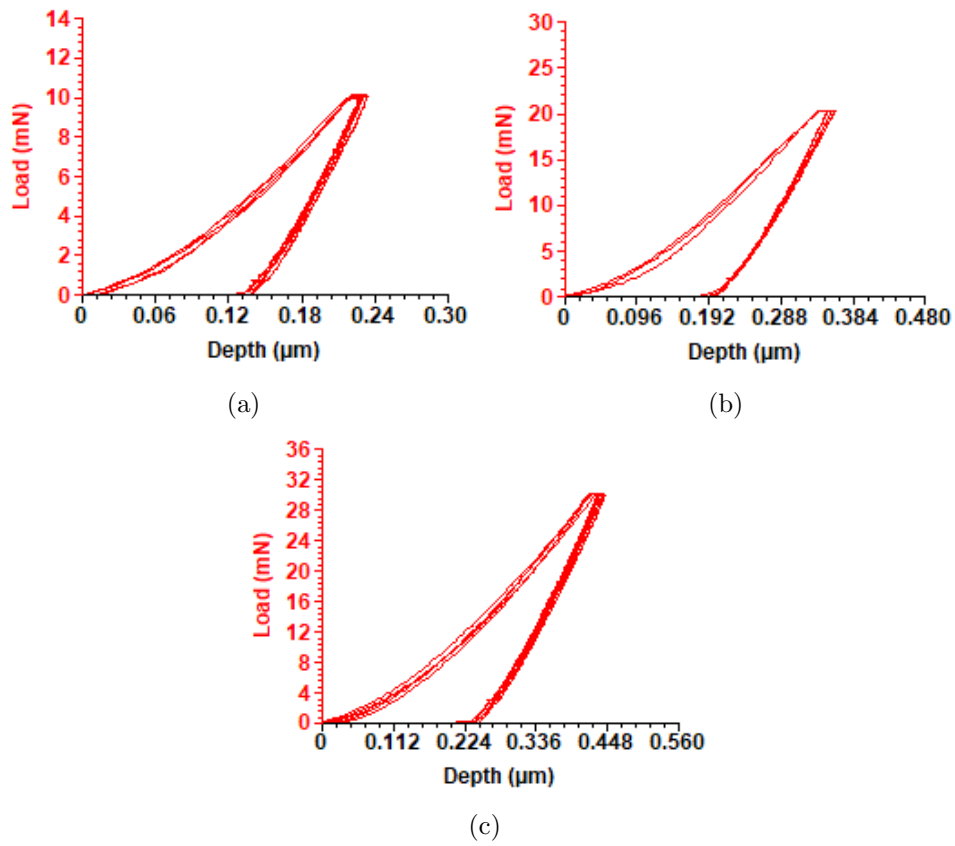


Figure D.1: Depth vs load curves of FAST sintered $CaTiO_3$ with load of (a) 10 mN, (b) 20 mN and (c) 30 mN.

Bibliography

- [1] F. Zhang and E. Burkel, “Novel titanium manganese alloys and their macroporous foams for biomedical applications prepared by field assisted sintering,” in *Biomedical Engineering, Trends in Materials Science*, InTech, 2011.
- [2] F. Zhang, Y. Quan, M. Reich, O. Kessler, and E. Burkel, “Sintering and heat treatment of titanium alloys by pulsed electric current sintering,” in *Sintering Applications*, InTech, 2013.
- [3] A.-M. Yousefi, H. Oudadesse, R. Akbarzadeh, E. Wers, and A. Lucas-Girot, “Physical and biological characteristics of nanohydroxyapatite and bioactive glasses used for bone tissue engineering,” *Nanotechnology Reviews*, vol. 3, no. 6, pp. 527–552, 2014.
- [4] F. R. Baxter, C. R. Bowen, I. G. Turner, and A. C. Dent, “Electrically active bioceramics: A review of interfacial responses,” *Annals of biomedical engineering*, vol. 38, no. 6, pp. 2079–2092, 2010.
- [5] E. Fukada and I. Yasuda, “On the piezoelectric effect of bone,” *Journal of the physical society of Japan*, vol. 12, no. 10, pp. 1158–1162, 1957.
- [6] E. Fukada and I. Yasuda, “Piezoelectric effects in collagen,” *Japanese Journal of Applied Physics*, vol. 3, no. 2, p. 117, 1964.
- [7] D. Pienkowski and S. Pollack, “The origin of stress-generated potentials in fluid-saturated bone,” *Journal of Orthopaedic Research*, vol. 1, no. 1, pp. 30–41, 1983.
- [8] J. Ferrier, S. M. Ross, J. Kanehisa, and J. E. Aubin, “Osteoclasts and osteoblasts migrate in opposite directions in response to a constant electrical field,” *Journal of cellular physiology*, vol. 129, no. 3, pp. 283–288, 1986.
- [9] S. Singh and S. Saha, “Electrical properties of bone. a review.,” *Clinical orthopaedics and related research*, no. 186, pp. 249–271, 1984.
- [10] D. Wieland, C. Krywka, E. Mick, R. Willumeit-Römer, R. Bader, and D. Klues, “Investigation of the inverse piezoelectric effect of trabecular bone on a micrometer length scale using synchrotron radiation,” *Acta biomaterialia*, vol. 25, pp. 339–346, 2015.
- [11] S. Spriano, S. Ferraris, C. Bianchi, C. Cassinelli, P. Torricelli, M. Fini, L. Rimondini, R. Giardino, *et al.*, “Bioactive titanium surfaces,” 2010.
- [12] M. PLUS, “Is pzt an environment friendly piezoelectric material?,”
- [13] H. Choudhury, R. Cary, W. H. Organization, *et al.*, “Barium and barium compounds,” 2001.

- [14] R. Tazaki, D. Fu, M. Itoh, M. Daimon, and S.-y. Koshihara, "Lattice distortion under an electric field in batio3 piezoelectric single crystal," *Journal of Physics: Condensed Matter*, vol. 21, no. 21, p. 215 903, 2009.
- [15] N. Ohtsu, K. Sato, K. Saito, K. Asami, and T. Hanawa, "Calcium phosphates formation on catio 3 coated titanium," *Journal of Materials Science: Materials in Medicine*, vol. 18, no. 6, pp. 1009–1016, 2007.
- [16] K. Hamada, M. Kon, T. Hanawa, K. Yokoyama, Y. Miyamoto, and K. Asaoka, "Hydrothermal modification of titanium surface in calcium solutions," *Biomaterials*, vol. 23, no. 10, pp. 2265–2272, 2002.
- [17] T. J. Webster, C. Ergun, R. H. Doremus, and W. A. Lanford, "Increased osteoblast adhesion on titanium-coated hydroxylapatite that forms catio3," *Journal of Biomedical Materials Research Part A: An Official Journal of The Society for Biomaterials, The Japanese Society for Biomaterials, and The Australian Society for Biomaterials and the Korean Society for Biomaterials*, vol. 67, no. 3, pp. 975–980, 2003.
- [18] A. K. Dubey, G. Tripathi, and B. Basu, "Characterization of hydroxyapatite-perovskite (catio3) composites: Phase evaluation and cellular response," *Journal of Biomedical Materials Research Part B: Applied Biomaterials*, vol. 95, no. 2, pp. 320–329, 2010.
- [19] A. Kholkin, N. Pertsev, and A. Goltsev, "Piezoelectricity and crystal symmetry," in *Piezoelectric and Acoustic Materials for Transducer Applications*, Springer, 2008, pp. 17–38.
- [20] J. W. Anthony, *Handbook of mineralogy: Arsenates, phosphates, vanadates. arsenates, phosphates, vanadates*. Mineral Data Pub., 2000, vol. 4.
- [21] A. Erba, K. E. El-Kelany, M. Ferrero, I. Baraille, and M. Rérat, "Piezoelectricity of srtio3: An ab initio description," *Physical Review B*, vol. 88, no. 3, p. 035 102, 2013.
- [22] T. Nishigaki and S. Hontsu, "Effect of poling treatment on piezoelectric constant of pulsed laser deposited hydroxyapatite thin films.," *Key Engineering Materials*, vol. 631, 2014.
- [23] S. Van Aert, S. Turner, R. Delville, D. Schryvers, G. Van Tendeloo, and E. K. Salje, "Direct observation of ferrielectricity at ferroelastic domain boundaries in catio3 by electron microscopy," *Advanced Materials*, vol. 24, no. 4, pp. 523–527, 2012.
- [24] M. Hantusch, V. Bessergenev, M. Mateus, M. Knupfer, and E. Burkel, "Electronic properties of photocatalytic improved degussa p25 titanium dioxide powder," *Catalysis Today*, vol. 307, pp. 111–118, 2018.
- [25] T. Rojac, M. Kosec, B. Budic, N. Setter, and D. Damjanovic, "Strong ferroelectric domain-wall pinning in bifeo 3 ceramics," *Journal of Applied Physics*, vol. 108, no. 7, p. 074 107, 2010.
- [26] O. Guillon, J. Gonzalez-Julian, B. Dargatz, T. Kessel, G. Schierning, J. Räthel, and M. Herrmann, "Field-assisted sintering technology/spark plasma sintering: Mechanisms, materials, and technology developments," *Advanced Engineering Materials*, vol. 16, no. 7, pp. 830–849, 2014.

- [27] J. Garay, "Current-activated, pressure-assisted densification of materials," *Annual review of materials research*, vol. 40, pp. 445–468, 2010.
- [28] R. Orru, R. Licheri, A. M. Locci, A. Cincotti, and G. Cao, "Consolidation/synthesis of materials by electric current activated/assisted sintering," *Materials Science and Engineering: R: Reports*, vol. 63, no. 4-6, pp. 127–287, 2009.
- [29] Z. A. Munir, D. V. Quach, and M. Ohyanagi, "Electric current activation of sintering: A review of the pulsed electric current sintering process," *Journal of the American Ceramic Society*, vol. 94, no. 1, pp. 1–19, 2011.
- [30] S. Jauregi, F. Fernández, R. Palma, V. Martínez, and J. Urcola, "Influence of atmosphere on sintering of t15 and m2 steel powders," *Metallurgical Transactions A*, vol. 23, no. 2, pp. 389–400, 1992.
- [31] A. Rečnik, J. Bruley, W. Mader, D. Kolar, and M. Rühle, "Structural and spectroscopic investigation of (111) twins in barium titanate," *Philosophical Magazine B*, vol. 70, no. 5, pp. 1021–1034, 1994.
- [32] V. Kodash, J. Groza, K. Cho, B. Klotz, and R. Dowding, "Field-assisted sintering of ni nanopowders," *Materials Science and Engineering: A*, vol. 385, no. 1-2, pp. 367–371, 2004.
- [33] E. Burkel and R. Schnierer, "Molding comprising piezoactive calcium titanium, a process for their preparation and excitation and use piezoactive calciumtitanoxids as a piezoelectric body or form part of piezoelectric moldings."
- [34] N. Ohtsu, K. Sato, A. Yanagawa, K. Saito, Y. Imai, T. Kohgo, A. Yokoyama, K. Asami, and T. Hanawa, "Catio3 coating on titanium for biomaterial application—optimum thickness and tissue response," *Journal of Biomedical Materials Research Part A: An Official Journal of The Society for Biomaterials, The Japanese Society for Biomaterials, and The Australian Society for Biomaterials and the Korean Society for Biomaterials*, vol. 82, no. 2, pp. 304–315, 2007.
- [35] T. Ikeda, *Fundamentals of piezoelectricity*. Oxford university press, 1996.
- [36] L. test project, *Common structure of binary compounds*. [Online]. Available: <https://chem.libretexts.org/>.
- [37] M. Hantusch, "Temperature anomalies in transition-metal-oxides and their correlations with photocatalytic activity," PhD thesis, University if Rostock, 2017.
- [38] R. Ali and M. Yashima, "Space group and crystal structure of the perovskite catio3 from 296 to 1720 k," *Journal of Solid State Chemistry*, vol. 178, no. 9, pp. 2867–2872, 2005.
- [39] F. Kröger and H. Vink, "Relations between the concentrations of imperfections in crystalline solids," in *Solid state physics*, vol. 3, Elsevier, 1956, pp. 307–435.
- [40] A. Beran, E. Libowitzky, and T. Armbruster, "A single-crystal infrared spectroscopic and x-ray-diffraction study of untwinned san benito perovskite containing oh groups," *The Canadian Mineralogist*, vol. 34, no. 4, pp. 803–809, 1996.
- [41] K. Momma and F. Izumi, "Vesta 3 for three-dimensional visualization of crystal, volumetric and morphology data," *Journal of applied crystallography*, vol. 44, no. 6, pp. 1272–1276, 2011.

- [42] M. Zhou, T. Bak, J. Nowotny, M. Rekas, C. Sorrell, and E. Vance, "Defect chemistry and semiconducting properties of calcium titanate," *Journal of Materials Science: Materials in Electronics*, vol. 13, no. 12, pp. 697–704, 2002.
- [43] P. Kofstad, "Nonstoichiometry, diffusion, and electrical conductivity in binary metal oxides," 1972.
- [44] J. E. Daniels, W. Jo, J. Rödel, V. Honkimäki, and J. L. Jones, "Electric-field-induced phase-change behavior in (bi_{0.5}na_{0.5})tio₃-batio₃-(k_{0.5}na_{0.5})nbo₃: A combinatorial investigation," *Acta Materialia*, vol. 58, no. 6, pp. 2103–2111, 2010.
- [45] W. George and R. Grace, "Formation of point defects in calcium titanate," *Journal of Physics and Chemistry of Solids*, vol. 30, no. 4, pp. 881–887, 1969.
- [46] K. Udayakumar and A. N. Cormack, "Structural aspects of phase equilibria in the strontium-titanium-oxygen system," *Journal of the American Ceramic Society*, vol. 71, no. 11, pp. C469–C471, 1988.
- [47] U. Balachandran and N. G. Eror, "Electrical conductivity in calcium titanate with excess cao," *Materials Science and Engineering*, vol. 54, no. 2, pp. 221–228, 1982.
- [48] K. Udayakumar and A. Cormack, "Non-stoichiometry in alkaline earth excess alkaline earth titanates," *Journal of Physics and Chemistry of Solids*, vol. 50, no. 1, pp. 55–60, 1989.
- [49] N. Eror and U. Balachandran, "On the defect structure of calcium titanate with nonideal cationic ratio," *Journal of Solid State Chemistry*, vol. 43, no. 2, pp. 196–203, 1982.
- [50] U. Balachandran, B. Odekirk, and N. Eror, "Electrical conductivity in calcium titanate," *Journal of Solid State Chemistry*, vol. 41, no. 2, pp. 185–194, 1982.
- [51] X. Pan, M.-Q. Yang, X. Fu, N. Zhang, and Y.-J. Xu, "Defective tio₂ with oxygen vacancies: Synthesis, properties and photocatalytic applications," *Nanoscale*, vol. 5, no. 9, pp. 3601–3614, 2013.
- [52] M. Calleja, M. T. Dove, and E. K. Salje, "Trapping of oxygen vacancies on twin walls of catio₃: A computer simulation study," *Journal of Physics: Condensed Matter*, vol. 15, no. 14, p. 2301, 2003.
- [53] H. Cheng and A. Selloni, "Surface and subsurface oxygen vacancies in anatase tio₂ and differences with rutile," *Physical Review B*, vol. 79, no. 9, p. 092 101, 2009.
- [54] D. Damjanovic, "Hysteresis in piezoelectric and ferroelectric materials," *The science of hysteresis*, vol. 3, pp. 337–465, 2006.
- [55] B. Jaffe, *Piezoelectric ceramics*. Elsevier, 2012, vol. 3.
- [56] O. Ando Junior, M. Coelho, C. Malfatti, and V. Brusamarello, "Proposal of a micro generator piezoelectric for portable devices from the energy harvesting," in *International Conference on Renewable Energies and Power Quality*, 2014, pp. 08–10.

- [57] M. C. Ehmke, N. H. Khansur, J. E. Daniels, J. E. Blendell, and K. J. Bowman, "Resolving structural contributions to the electric-field-induced strain in lead-free $(1-x)\text{Ba}(\text{Zr}_{0.2}\text{Ti}_{0.8})\text{O}_3-x(\text{Ba}_{0.7}\text{Ca}_{0.3})\text{TiO}_3$ piezoceramics," *Acta Materialia*, vol. 66, pp. 340–348, 2014.
- [58] J. L. Jones, M. Hoffman, J. E. Daniels, and A. J. Studer, "Direct measurement of the domain switching contribution to the dynamic piezoelectric response in ferroelectric ceramics," *Applied physics letters*, vol. 89, no. 9, p. 092901, 2006.
- [59] T. Sluka, A. K. Tagantsev, P. Bednyakov, and N. Setter, "Free-electron gas at charged domain walls in insulating batio₃," *Nature communications*, vol. 4, p. 1808, 2013.
- [60] B. Sturman, E. Podivilov, M. Stepanov, A. Tagantsev, and N. Setter, "Quantum properties of charged ferroelectric domain walls," *Physical Review B*, vol. 92, no. 21, p. 214112, 2015.
- [61] N. Bassiri-Gharb, I. Fujii, E. Hong, S. Trolier-McKinstry, D. V. Taylor, and D. Damjanovic, "Domain wall contributions to the properties of piezoelectric thin films," *Journal of Electroceramics*, vol. 19, no. 1, pp. 49–67, 2007.
- [62] Y.-H. Seo, D. J. Franzbach, J. Koruza, A. Benčan, B. Malič, M. Kosec, J. L. Jones, and K. G. Webber, "Nonlinear stress-strain behavior and stress-induced phase transitions in soft $\text{Pb}(\text{Zr}_{1-x}\text{Ti}_x)\text{O}_3$ at the morphotropic phase boundary," *Physical Review B*, vol. 87, no. 9, p. 094116, 2013.
- [63] A. Achuthan and C. Sun, "Domain switching in ferroelectric ceramic materials under combined loads," *Journal of applied physics*, vol. 97, no. 11, p. 114103, 2005.
- [64] K. Aizu, "Possible species of "ferroelastic" crystals and of simultaneously ferroelectric and ferroelastic crystals," *Journal of the Physical society of Japan*, vol. 27, no. 2, pp. 387–396, 1969.
- [65] G. Arlt and N. Pertsev, "Force constant and effective mass of 90 domain walls in ferroelectric ceramics," *Journal of Applied Physics*, vol. 70, no. 4, pp. 2283–2289, 1991.
- [66] N. Pertsev and A. Y. Emelyanov, "Domain-wall contribution to the piezoelectric response of epitaxial ferroelectric thin films," *Applied physics letters*, vol. 71, no. 25, pp. 3646–3648, 1997.
- [67] V. Koukhar, N. Pertsev, and R. Waser, "Thermodynamic theory of epitaxial ferroelectric thin films with dense domain structures," *Physical Review B*, vol. 64, no. 21, p. 214103, 2001.
- [68] A. V. Vinogradov and V. V. Vinogradov, "Low-temperature sol-gel synthesis of crystalline materials," *RSC Advances*, vol. 4, no. 86, pp. 45903–45919, 2014.
- [69] P. Mallik, G. Biswal, S. Patnaik, and S. Senapati, "Characterisation of sol-gel synthesis of phase pure CaTiO_3 nano powders after drying," in *IOP Conference Series: Materials Science and Engineering*, IOP Publishing, vol. 75, 2015, p. 012005.
- [70] C. J. Brinker and G. W. Scherer, *Sol-gel science: The physics and chemistry of sol-gel processing*. Academic press, 2013.

- [71] Y. Lu, R. Ganguli, C. A. Drewien, M. T. Anderson, C. J. Brinker, W. Gong, Y. Guo, H. Soyeze, B. Dunn, M. H. Huang, *et al.*, “Continuous formation of supported cubic and hexagonal mesoporous films by sol–gel dip-coating,” *Nature*, vol. 389, no. 6649, p. 364, 1997.
- [72] Z. Wang, L. Shi, F. Wu, S. Yuan, Y. Zhao, and M. Zhang, “The sol–gel template synthesis of porous tio₂ for a high performance humidity sensor,” *Nanotechnology*, vol. 22, no. 27, p. 275 502, 2011.
- [73] M. Hantusch, “Temperature anomalies in transition-metal-oxides and their correlations with photocatalytic activity,” *Doctoral dissertation*, 2017.
- [74] R. Patel, M. Patel, and A. Suthar, “Spray drying technology: An overview,” *Indian Journal of Science and Technology*, vol. 2, no. 10, pp. 44–47, 2009.
- [75] Z. Munir, U. Anselmi-Tamburini, and M. Ohyanagi, “The effect of electric field and pressure on the synthesis and consolidation of materials: A review of the spark plasma sintering method,” *Journal of Materials Science*, vol. 41, no. 3, pp. 763–777, 2006.
- [76] D. M. Hulbert, A. Anders, D. V. Dudina, J. Andersson, D. Jiang, C. Unuvar, U. Anselmi-Tamburini, E. J. Lavernia, and A. K. Mukherjee, “The absence of plasma in “spark plasma sintering”,” *Journal of Applied Physics*, vol. 104, no. 3, p. 033 305, 2008.
- [77] R. H. Castro, “Overview of conventional sintering,” in *Sintering*, Springer, 2012, pp. 1–16.
- [78] A. S. Mujumdar, *Handbook of industrial drying*. CRC press, 2014.
- [79] K. Witte, W. Bodnar, N. Schell, H. Lang, and E. Burkel, “High energy x-ray diffraction study of a dental ceramics–titanium functional gradient material prepared by field assisted sintering technique,” *Materials Characterization*, vol. 95, pp. 266–271, 2014.
- [80] Q. Hu, P. Luo, and Y. Yan, “Influence of spark plasma sintering temperature on sintering behavior and microstructures of dense bulk mosi₂,” *Journal of Alloys and Compounds*, vol. 459, no. 1-2, pp. 163–168, 2008.
- [81] C. Schick, “Differential scanning calorimetry (dsc) of semicrystalline polymers,” *Analytical and bioanalytical chemistry*, vol. 395, no. 6, p. 1589, 2009.
- [82] I. NPTEL, *Differential scanning calorimetry*. [Online]. Available: <http://nptel.ac.in/courses/115103030/module4/lec22/2.html>.
- [83] H. K. D. H. Bhadeshia, *Thermal analysis techniques, Differential Scanning Calorimetry*. 2002.
- [84] K. Kodre, S. Attarde, P. Yendhe, R. Patil, and V. Barge, “Differential scanning calorimetry: A review,” *Research and Reviews: Journal of Pharmaceutical Analysis*, vol. 3, no. 3, pp. 11–22, 2014.
- [85] T. L. C. Ltd, *High-resolution scanning electron microscopy*. [Online]. Available: <http://www.technoorg.hu/news-and-events/articles/high-resolution-scanning-electron-microscopy-1/>.
- [86] S. Amelinckx, D. Van Dyck, J. Van Landuyt, and G. Van Tendeloo, *Electron microscopy: Principles and fundamentals*. John Wiley & Sons, 2008.

- [87] D. Shindo and T. Oikawa, “Energy dispersive x-ray spectroscopy,” in *Analytical Electron Microscopy for Materials Science*, Springer, 2002, pp. 81–102.
- [88] J. F. Moulder, W. F. Stickle, P. E. Sobol, and K. D. Bomben, “Handbook of x-ray photoelectron spectroscopy: A reference book of standard spectra for identification and interpretation of xps data; physical electronics: Eden prairie, mn, 1995,” *Google Scholar*, p. 261, 2000.
- [89] J. Fialka and P. Beneš, “Comparison of methods of piezoelectric coefficient measurement,” in *Instrumentation and Measurement Technology Conference (I2MTC), 2012 IEEE International*, IEEE, 2012, pp. 37–42.
- [90] E. Burkel, “Introduction to x-ray scattering,” *Journal of Physics: Condensed Matter*, vol. 13, no. 34, p. 7477, 2001.
- [91] Edited by: R E Dinnebier and S J L Billinge, *Powder Diffraction : Theory and Practice*. 2008, pp. 1–582.
- [92] H. Rietveld, “A profile refinement method for nuclear and magnetic structures,” *Journal of applied Crystallography*, vol. 2, no. 2, pp. 65–71, 1969.
- [93] H. Rietveld, “Line profiles of neutron powder-diffraction peaks for structure refinement,” *Acta Crystallographica*, vol. 22, no. 1, pp. 151–152, 1967.
- [94] G. Caglioti, A. t. Paoletti, and F. Ricci, “Choice of collimators for a crystal spectrometer for neutron diffraction,” *Nuclear Instruments*, vol. 3, no. 4, pp. 223–228, 1958.
- [95] L. Lutterotti and P. Scardi, “Simultaneous structure and size–strain refinement by the rietveld method,” *Journal of applied Crystallography*, vol. 23, no. 4, pp. 246–252, 1990.
- [96] L. Lutterotti, “Introduction to diffraction and the rietveld method,” *Laboratorio Scienza e Tecnologia dei Materiali*, pp. 6–20, 2012.
- [97] W. C. Oliver and G. M. Pharr, “Measurement of hardness and elastic modulus by instrumented indentation: Advances in understanding and refinements to methodology,” *Journal of materials research*, vol. 19, no. 1, pp. 3–20, 2004.
- [98] W. C. Oliver and G. M. Pharr, “An improved technique for determining hardness and elastic modulus using load and displacement sensing indentation experiments,” *Journal of materials research*, vol. 7, no. 6, pp. 1564–1583, 1992.
- [99] M. Doerner, D. Gardner, and W. Nix, “Plastic properties of thin films on substrates as measured by submicron indentation hardness and substrate curvature techniques,” *Journal of Materials Research*, vol. 1, no. 6, pp. 845–851, 1986.
- [100] C. A. Schneider, W. S. Rasband, and K. W. Eliceiri, “Nih image to imagej: 25 years of image analysis,” *Nature methods*, vol. 9, no. 7, p. 671, 2012.
- [101] M. Hantusch, V. Bessergenev, M. Mateus, M. Knupfer, and E. Burkel, “Electronic properties of photocatalytic improved degussa p25 titanium dioxide powder,” *Catalysis Today*, 2017.
- [102] K. Prume, S. Tiedke, and T. Schmitz-Kempen, “Double-beam and four-point,” *Mikroniek nr*, vol. 4, pp. 31–35, 2010.

- [103] N. Schell, A. King, F. Beckmann, T. Fischer, M. Müller, and A. Schreyer, “The high energy materials science beamline (hems) at petra iii,” in *Materials Science Forum*, Trans Tech Publ, vol. 772, 2014, pp. 57–61.
- [104] N. Schell, A. King, F. Beckmann, H.-U. Ruhnau, R. Kirchhof, R. Kiehn, M. Müller, and A. Schreyer, “The high energy materials science beamline (hems) at petra iii,” in *AIP Conference Proceedings*, AIP, vol. 1234, 2010, pp. 391–394.
- [105] L. Lutterotti, M. Bortolotti, G. Ischia, I. Lonardelli, and H. Wenk, “Rietveld texture analysis from diffraction images,” *Z. Kristallogr. Suppl*, vol. 26, pp. 125–130, 2007.
- [106] L. Lutterotti, S. Matthies, H.-R. Wenk, A. Schultz, and J. Richardson Jr, “Combined texture and structure analysis of deformed limestone from time-of-flight neutron diffraction spectra,” *Journal of Applied Physics*, vol. 81, no. 2, pp. 594–600, 1997.
- [107] J. Yu, C. Y. Jimmy, W. Ho, M. K.-P. Leung, B. Cheng, G. Zhang, and X. Zhao, “Effects of alcohol content and calcination temperature on the textural properties of bimodally mesoporous titania,” *Applied Catalysis A: General*, vol. 255, no. 2, pp. 309–320, 2003.
- [108] S. Manik, S. Pradhan, and M. Pal, “Nanocrystalline TiO_3 prepared by soft-chemical route,” *Physica E: Low-dimensional Systems and Nanostructures*, vol. 25, no. 4, pp. 421–424, 2005.
- [109] A. Di Paola, M. Bellardita, and L. Palmisano, “Brookite, the least known TiO_2 photocatalyst,” *Catalysts*, vol. 3, no. 1, pp. 36–73, 2013.
- [110] M. D. Abràmoff, P. J. Magalhães, and S. J. Ram, “Image processing with imagej,” *Biophotonics international*, vol. 11, no. 7, pp. 36–42, 2004.
- [111] D. Marshall, A. G. Evans, B. Khuri Yakub, J. Tien, and G. Kino, “The nature of machining damage in brittle materials,” *Proceedings of the Royal Society of London. A. Mathematical and Physical Sciences*, vol. 385, no. 1789, pp. 461–475, 1983.
- [112] Z. Z. Fang, H. Wang, and V. Kumar, “Coarsening, densification, and grain growth during sintering of nano-sized powders—a perspective,” *International Journal of Refractory Metals and Hard Materials*, vol. 62, pp. 110–117, 2017.
- [113] X. Casa, “Version 2.3. 16,” *Casa Software Ltd.: Teignmouth, UK*, 2010.
- [114] M. Wojdyr, “Fityk: A general-purpose peak fitting program,” *Journal of Applied Crystallography*, vol. 43, no. 5-1, pp. 1126–1128, 2010.
- [115] T. Williams and C. Kelley, *Many others, gnuplot 4.4: An interactive plotting program*, 2010.
- [116] R. Asahi, T. Morikawa, T. Ohwaki, K. Aoki, and Y. Taga, “Visible-light photocatalysis in nitrogen-doped titanium oxides,” *Science*, vol. 293, no. 5528, pp. 269–271, 2001.
- [117] M. Ishfaq, M. Rizwan Khan, M. Bhopal, F. Nasim, A. Ali, A. Bhatti, I. Ahmed, S. Bhardwaj, and C. Cepek, “1.5 mev proton irradiation effects on electrical and structural properties of $\text{TiO}_2/\text{n-si}$ interface,” *Journal of Applied Physics*, vol. 115, no. 17, p. 174506, 2014.

- [118] S.-W. Lee, L. Lozano-Sánchez, and V. Rodríguez-González, “Green tide deactivation with layered-structure cuboids of Ag/CaTiO_3 under uv light,” *Journal of hazardous materials*, vol. 263, pp. 20–27, 2013.
- [119] L. Lutterotti, R. Ceccato, R. Dal Maschio, and E. Pagani, “Quantitative analysis of silicate glass in ceramic materials by the rietveld method,” in *Materials Science Forum*, Aedermannsdorf, Switzerland: Trans Tech Publications, 1984-, vol. 278, 1998, pp. 87–92.
- [120] B. Ullah, W. Lei, Q.-S. Cao, Z.-Y. Zou, X.-K. Lan, X.-H. Wang, and W.-Z. Lu, “Structure and microwave dielectric behavior of a-site-doped $\text{Sr}(1-x)\text{Ca}x\text{TiO}_3$ ceramics system,” *Journal of the American Ceramic Society*, vol. 99, no. 10, pp. 3286–3292, 2016.
- [121] T. Phongamwong, M. Chareonpanich, and J. Limtrakul, “Role of chlorophyll in spirulina on photocatalytic activity of CO_2 reduction under visible light over modified n-doped TiO_2 photocatalysts,” *Applied Catalysis B: Environmental*, vol. 168, pp. 114–124, 2015.
- [122] M. Nasir, S. Bagwasi, Y. Jiao, F. Chen, B. Tian, and J. Zhang, “Characterization and activity of the ce and n co-doped TiO_2 prepared through hydrothermal method,” *Chemical Engineering Journal*, vol. 236, pp. 388–397, 2014.
- [123] S. Hu, F. Li, Z. Fan, and J. Gui, “Improved photocatalytic hydrogen production property over Ni/NiO/n-TiO_2-x heterojunction nanocomposite prepared by NH_3 plasma treatment,” *Journal of Power Sources*, vol. 250, pp. 30–39, 2014.
- [124] J. Liu, R. Han, Y. Zhao, H. Wang, W. Lu, T. Yu, and Y. Zhang, “Enhanced photoactivity of v- n codoped TiO_2 derived from a two-step hydrothermal procedure for the degradation of pcp- na under visible light irradiation,” *The Journal of Physical Chemistry C*, vol. 115, no. 11, pp. 4507–4515, 2011.
- [125] B. Richter, H. Kuhlenbeck, H.-J. Freund, and P. S. Bagus, “Cluster core-level binding-energy shifts: The role of lattice strain,” *Physical review letters*, vol. 93, no. 2, p. 026 805, 2004.
- [126] X. Chen and C. Burda, “Photoelectron spectroscopic investigation of nitrogen-doped titania nanoparticles,” *The Journal of Physical Chemistry B*, vol. 108, no. 40, pp. 15 446–15 449, 2004.
- [127] A. Kushima and B. Yildiz, “Role of lattice strain and defect chemistry on the oxygen vacancy migration at the $(8.3\% \text{Y}_2\text{O}_3\text{-ZrO}_2)/\text{SrTiO}_3$ hetero-interface: A first principles study,” *ECS Transactions*, vol. 25, no. 2, pp. 1599–1609, 2009.
- [128] G. Esteves, C. M. Fancher, S. Röhrig, G. A. Maier, J. L. Jones, and M. Deluca, “Electric-field-induced structural changes in multilayer piezoelectric actuators during electrical and mechanical loading,” *Acta Materialia*, vol. 132, pp. 96–105, 2017.
- [129] V. Hauk, *Structural and residual stress analysis by nondestructive methods: Evaluation-Application-Assessment*. Elsevier, 1997.
- [130] C. Heitsch, C. Nordman, and R. Parry, “The crystal structure and dipole moment in solution of the compound $\text{AlH}_3 \cdot 2\text{n}(\text{CH}_3)_3$,” *Inorganic Chemistry*, vol. 2, no. 3, pp. 508–512, 1963.

- [131] A. V. Stanishevsky and S. Holliday, "Mechanical properties of sol-gel calcium titanate bioceramic coatings on titanium," *Surface and Coatings Technology*, vol. 202, no. 4-7, pp. 1236-1241, 2007.
- [132] J. Zhang, G. L. Niebur, and T. C. Ovaert, "Mechanical property determination of bone through nano-and micro-indentation testing and finite element simulation," *Journal of biomechanics*, vol. 41, no. 2, pp. 267-275, 2008.
- [133] M. Ridzwan, S. Shuib, A. Hassan, A. Shokri, and M. M. Ibrahim, "Problem of stress shielding and improvement to the hip implant designs: A review," *J. Med. Sci*, vol. 7, no. 3, pp. 460-467, 2007.
- [134] L. Goncalves-Ferreira, S. A. Redfern, E. Artacho, and E. K. Salje, "Ferroelectric twin walls in CaTiO_3 ," *Physical review letters*, vol. 101, no. 9, p. 097602, 2008.
- [135] F. J. Humphreys and M. Hatherly, *Recrystallization and related annealing phenomena*. Elsevier, 2012.
- [136] F. Maglia, I. G. Tredici, and U. Anselmi-Tamburini, "Densification and properties of bulk nanocrystalline functional ceramics with grain size below 50 nm," *Journal of the European Ceramic Society*, vol. 33, no. 6, pp. 1045-1066, 2013.
- [137] K. Huang and R. Logé, "A review of dynamic recrystallization phenomena in metallic materials," *Materials & Design*, vol. 111, pp. 548-574, 2016.
- [138] Y. Zhou, K. Hirao, Y. Yamauchi, and S. Kanzaki, "Densification and grain growth in pulse electric current sintering of alumina," *Journal of the European Ceramic Society*, vol. 24, no. 12, pp. 3465-3470, 2004.
- [139] S.-Y. Choi, S.-D. Kim, M. Choi, H.-S. Lee, J. Ryu, N. Shibata, T. Mizoguchi, E. Tochigi, T. Yamamoto, S.-J. L. Kang, *et al.*, "Assessment of strain-generated oxygen vacancies using SrTiO_3 bicrystals," *Nano letters*, vol. 15, no. 6, pp. 4129-4134, 2015.
- [140] P. A. Cox, *Transition metal oxides: An introduction to their electronic structure and properties*. Oxford university press, 2010, vol. 27.
- [141] S. R. Moheimani and A. J. Fleming, "Fundamentals of piezoelectricity," *Piezoelectric transducers for vibration control and damping*, pp. 9-35, 2006.
- [142] H. S. Nalwa, *Ferroelectric polymers: Chemistry: Physics, and applications*. CRC Press, 1995.
- [143] M. Minary-Jolandan and M.-F. Yu, "Shear piezoelectricity in bone at the nanoscale," *Applied Physics Letters*, vol. 97, no. 15, p. 153127, 2010.
- [144] J. Anderson and C. Eriksson, "Piezoelectric properties of dry and wet bone," *Nature*, vol. 227, no. 5257, p. 491, 1970.
- [145] C. Fancher, S. Brewer, C. Chung, S. Röhrig, T. Rojac, G. Esteves, M. Deluca, N. Bassiri-Gharb, and J. Jones, "The contribution of 180 domain wall motion to dielectric properties quantified from in situ x-ray diffraction," *Acta Materialia*, vol. 126, pp. 36-43, 2017.
- [146] A. Pramanick, D. Damjanovic, J. E. Daniels, J. C. Nino, and J. L. Jones, "Origins of electro-mechanical coupling in polycrystalline ferroelectrics during subcoercive electrical loading," *Journal of the American Ceramic Society*, vol. 94, no. 2, pp. 293-309, 2011.

- [147] L. Fan, J. Chen, Y. Ren, Z. Pan, L. Zhang, and X. Xing, "Unique piezoelectric properties of the monoclinic phase in pb (zr, ti) o₃ ceramics: Large lattice strain and negligible domain switching," *Physical review letters*, vol. 116, no. 2, p. 027601, 2016.
- [148] S. Saha, T. Sinha, and A. Mookerjee, "Structural and optical properties of paraelectric srtio₃," *Journal of Physics: Condensed Matter*, vol. 12, no. 14, p. 3325, 2000.
- [149] N. W. Ashcroft and N. D. Mermin, "Solid state physics (holt, rinehart and winston, new york, 1976)," *Google Scholar*, vol. 403, 2005.
- [150] A. Yoshiasa, T. Nakatani, A. Nakatsuka, M. Okube, K. Sugiyama, and T. Mashimo, "High-temperature single-crystal x-ray diffraction study of tetragonal and cubic perovskite-type pbtio₃ phases," *Acta Crystallographica Section B: Structural Science, Crystal Engineering and Materials*, vol. 72, no. 3, pp. 381–388, 2016.
- [151] C. M. Fancher, J. E. Blendell, and K. J. Bowman, "Decoupling of superposed textures in an electrically biased piezoceramic with a 100 preferred orientation," *Applied Physics Letters*, vol. 110, no. 6, p. 062901, 2017.
- [152] M. Deluca, "Microscopic texture characterisation in piezoceramics," *Advances in Applied Ceramics*, vol. 115, no. 2, pp. 112–122, 2016.
- [153] G. Tutuncu, M. Motahari, J. Bernier, M. Varlioglu, J. L. Jones, and E. Ustundag, "Strain evolution of highly asymmetric polycrystalline ferroelectric ceramics via a self-consistent model and in situ x-ray diffraction," *Journal of the American Ceramic Society*, vol. 95, no. 12, pp. 3947–3954, 2012.
- [154] X. Duan, D. Jia, Z. Wu, Z. Tian, Z. Yang, S. Wang, and Y. Zhou, "Effect of sintering pressure on the texture of hot-press sintered hexagonal boron nitride composite ceramics," *Scripta Materialia*, vol. 68, no. 2, pp. 104–107, 2013.
- [155] J. Ricote, L. Pardo, A. Moure, A. Castro, P. Millán, and D. Chateigner, "Microcharacterisation of grain-oriented ceramics based on bi₃tinbo₉ obtained from mechanochemically activated precursors," *Journal of the European Ceramic Society*, vol. 21, no. 10-11, pp. 1403–1407, 2001.
- [156] A. Kumar, V. B. Prasad, K. J. Raju, and A. James, "Optimization of poling parameters of mechanically processed plzt 8/60/40 ceramics based on dielectric and piezoelectric studies," *The European Physical Journal B*, vol. 88, no. 11, p. 287, 2015.

Acknowledgement

First of all I would like to thank Prof. Dr. Eberhard Burkel for giving me the opportunity to work in the group of Physics of New Materials under his supervision. His support during the whole time led to the successful completion of this work. Furthermore, I am grateful to Bärbel Przybill and Ulrike Schröder for the friendly environment. I deeply appreciate Dr. Wiktor Bodnar and Dr. Kerstin Witte. Their support in X-ray diffraction experiments as well as discussions significantly influenced this work.

I also acknowledge M.Sc. Marcel Benjamin Wetegrove and M.Sc. Rico Schnierer, especially Dr. Martin Hantusch for useful discussions. Also, Dr. Martin Hantusch is appreciated to perform X-ray photoelectron spectroscopy on $CaTiO_3$.

Moreover, I would like to appreciate the support of Dr. Norbert Schell from Helmholtz-Center Geesthacht at the beamline in Hamburg and of Dr. Armin Springer from the EMZ University of Rostock for the help at the scanning electron microscope. Furthermore, I want to thank Carola Ladewig for the polishing of samples and Dr. Richard Dietrich for his assistance in sputter coating.

Finally, I am thankful to my friends M.Sc. Haider Ali and M.Sc. Waleed Arshad for their support. There was also a significant support from my parents and wife, especially from my father.

Declaration

I hereby declare that I have prepared the present work on my own and wrote it without help from others, that I have not used anything other than the tools and sources I have indicated.

Abdullah Riaz
08.04.2019, Rostock